U.S. Department of Transportation

Federal Transit Administration

Final Report

Fuel Cells for Transportation Applications

Report Number FTA-IL-26-7006-2009.1

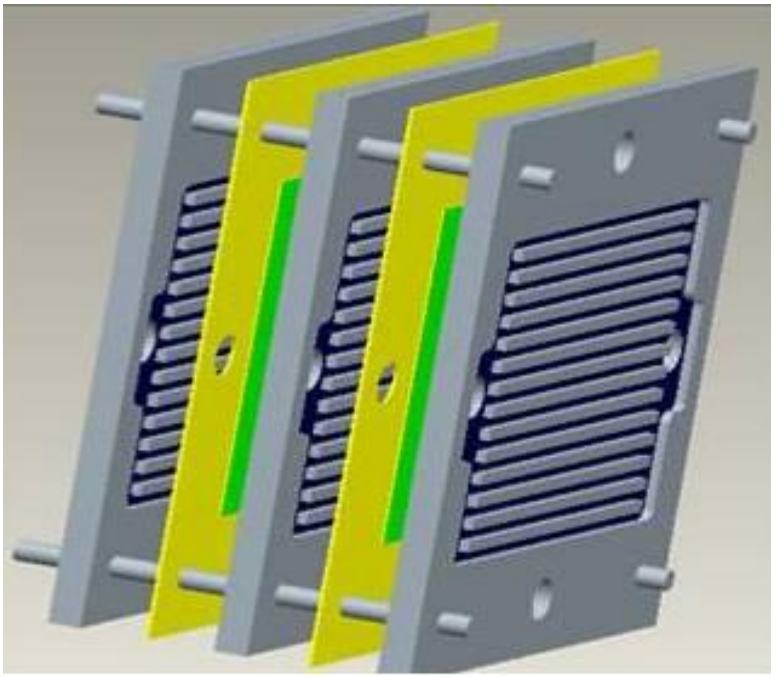

February 2009

http://www.fta.dot.gov/research

NOTICE

REPORT DOCUMENTATION PAGE

Form Approved
OMB No. 0704-0188

1. AGENCY USE ONLY (Leave blank)	2. REPORT DATE February 2009	3. REPORT TYPE AND DATES COVERED Final Report from October 1, 2004 to September 15, 2008

4. TITLE AND SUBTITLE
Fuel Cells for Transportation Applications

5. FUNDING/GRANT NUMBER
IL-26-7006

6. AUTHOR(S)
Principal Investigator: Promod Vhora
Prepared by: Anima Bose, Ph.D.; Lead Scientist

7. PERFORMING ORGANIZATION NAME(S) AND ADDRESS(ES)
College of Engineering and Engineering Technology
Northern Illinois University
DeKalb, Illinois 60115

Transportation Technology R&D Center
Argonne National Laboratory
Argonne, IL 60439

8. PERFORMING ORGANIZATION REPORT NUMBER
N/A

9. SPONSORING/MONITORING AGENCY NAME(S) AND ADDRESS(ES)
Federal Transit Administration
U.S. Department of Transportation
1200 New Jersey Avenue, SE
Washington, DC 20590

Website [http://www.fta.dot.gov/research]

10. SPONSORING-MONITORING AGENCY REPORT NUMBER
FTA-IL-26-7006-2009.1

11. SUPPLEMNTARY NOTES

12a. DISTRIBUTION/AVAILABILITY STATEMENT
Available From: National Technical Information Service (NTIS), Springfield, VA 22161.
Phone 703.605.6000, Fax 703.605.6900, Email [orders@ntis.gov]

12b. DISTRIBUTION CODE
TRI-12

13. ABSTRACT (Maximum 200 words)
Research team at Northern Illinois University in collaboration with the Argonne National laboratory, has made significant achievements in six areas. First, researchers have shown that platinum loading can be reduced at least by factor of five-fold to below 0.1 mg/cm^2 compared to currently commercially available electro-catalyst without sacrificing oxygen reduction ability. Second, loss of catalytic activities due to surface oxidation can be prevented by the newly designed polymeric metal phosphate catalysts. Third, corrosion of catalyst support surface can be minimized by boron-doped carbon materials. Fourth, performance of Nafion® based MEA can be enhanced by carefully controlling the dynamics of curing process and by adding specific reinforcing materials. Fifth, bipolar plate performance can significantly improve cell performance even at high current densities through the reduction of mass transfer losses. Sixth, new perovskites materials [$La_{1-x}Sr_xMnO_3$ ($x > 0.5$)] with increased oxygen vacancy states were synthesized and characterized. These materials are stable in the temperature range $200 < T < 700$ºC and exhibited long-term stability below 800ºC. In addition, the NIU-ANL team developed an alternate protocol for accelerated durability tests.

14. SUBJECT TERMS
Fuel Cells, Electrocatalyst, BiPolar Plates, Solid Oxide Fuel Cell (SOFC), Membrane Electrode Assembly (MEA), Platinum Catalysis, Cathode Materials, Multi-Cell Analysis, Multi-Cell Testing

15. NUMBER OF PAGES
125

16. PRICE CODE

17. SECURITY CLASSIFICATION OF REPORT	18. SECURITY CLASSIFICATION OF THIS PAGE	19. SECURITY CLASSIFICATION OF ABSTRACT	20. LIMITATION OF ABSTRACT
Unclassified	Unclassified	Unclassified	

U.S. Department
of Transportation
**Federal Transit
Administration**

FUEL CELLS FOR TRANSPORTATION APPLICATIONS

February 2009

Prepared by
Principal Investigator: Promod Vhora
Prepared by: Anima Bose, Ph.D.; Lead Scientist
College of Engineering and Engineering Technology
Northern Illinois University
DeKalb, Illinois 60115
[http://www.niu.edu/CEET/]

Report No. **FTA-TRI-IL-26-7006-2009.1**

Sponsored by
Federal Transit Administration
Office of Research, Demonstration and Innovation
U.S. Department of Transportation
1200 New Jersey Avenue, SE
Washington, D.C. 20590

Available Online
[http://www.fta.dot.gov/research]

Forward

This report summarizes a four-year effort to address the high costs, durability and reliability of materials components and systems for widespread application of transportation fuel cells. This effort included an explicit effort to develop the education and training of scientists, engineers, and technicians critical for the development, deployment and maintenance of fuel cell technology in stationary and portable power generation used for distributed residential and office power as well as public and private transportation systems.

Six technical challenges are addressed in this Department of Transportation (DOT) program to make cost effective fuel cells. First, develop effective ultra-low platinum loading catalysts for Proton Exchange Membrane Fuel Cell (PEMFC) and Direct Methanol Fuel Cells (DMFC). Second, synthesize and characterize low-temperature cathodic materials for Solid Oxide Fuel Cells (SOFC). Third, develop new catalyst support for durable catalytic activities. Fourth, explore advanced, more efficient, bipolar fuel cell plates design using computational tools .Fifth, improve performance of fuel cell membrane electrode assembly (MEA). Finally, explorer utilization of hybrid technology by combining fuel cell, battery, and ultra-capacitors.

This Department of Transportation (DOT) program has generated five patent applications (Appendix A), 13 publications in national and international journals (Appendix B), 13 presentations in national and international meetings (Appendix C), and supported either partially and fully 17 graduate students (Appendix D) in alternative energy technology to help the nation educate a workforce required for energy independence.

Table of Contents

CHAPTER 1 - Background and Challenges 1
Background 1
Educational Objectives: 2
New Catalysts 3
Catalyst Support 3
Bipolar Plates 4
Membrane Electrode Assembly (MEA) 6
Fuel Cell Material Durability 7
Hybrid Technology 8
Challenges 11
Chapter 2 – Methodology and Research Approach 12
Preparation and Characterization of New Catalysts for PEMFC 13
Chemical Electropolymerization Using Platinum Phosphate Blue 13
Preparation of Mixed-Valence Platinum-Phosphate Matrix Catalyst 17
Preparation of Mixed Metal Composite Catalyst 18
New Catalyst Support: Nano-Porous Boron Carbon Microsphere 18
Bipolar Plate 18
Computational Fluid Dynamics (CFD) Modeling of Bipolar Plate Flow Channel Design and Analysis 19
Fabrication, Testing and Performance Evaluation of Bipolar Plates 20
Data Acquisition Methodology: 22
Data Acquisition Software Implementation 22
Single Cell Performance 23
Preparation of Membrane Electrode Assembly 23
Performance Enhancement within Existing Technology 25
MEA Preparation with Nanocomposite Nafion® Membrane 26
Multi-Cell Performance 27
Durability Test Protocol 28
In-Situ Diagnostics 29
Post-Mortem Diagnostics 29
Power Conditioning 29
Acceleration Study 30
Driving cycle study 31
Power Flow Determination 33
Fuel Cell and Other ESU Optimization 33
Battery and Capacitor Optimization 37
Control Law Rules 39
Motor Control Method 39
Solid Oxide Fuel Cell Cathode 41
Synthesis of Samples for Special Experiments 43
Synthesis and Measurement of Mixed Conducting Cathodes 44
Chapter 3 Results and Discussion 45
Thin-Film of Ultralow Platinum Electrocatalyst by Chemical Electropolymerization 46
Tunable Platinum Phosphate Composite Thin-Film Electrocatalysts 48
Oxygen Reduction Ability by the Platinum Phosphate Matrix Catalyst 48

Catalyst at Potential Higher Than 1.0 V 51
Oxygen Reduction Efficiency 53
Minimization of Hydrogen Adsorption Property 54
Oxygen Reduction Efficiency of Mixed Metal Phosphate Composite Catalyst 55
Methanol Oxidation 56
Novel Catalyst Support 57
Bipolar Plates 59
Testing and Performance Evaluation of Bipolar Plates 61
PEM Fuel Cell Simulation Results 62
Hydrogen Concentration Distribution in Tri-Layer PEMFC 63
Oxygen Concentration Distribution in Tri-layer PEMFC 64
Temperature Distribution in Tri-Layer PEMFC 66
Water Distribution in Tri-Layer PEMFC 67
Cell Performance 68
Effect of Bi-Polar Plate Design on Polarization Curve 69
Thermo-Mechanical Analysis of Fuel Cell with Bi-Polar Plate 71
Single Cell Performance Evaluation 72
Platinum Phosphate Blue Cathode Catalyst 72
Nafion® and Commercially Available Catalyst 73
Multi- Cell Durability and Degradation Mechanisms 79
Initial Performance 79
Post-mortem diagnostic results 91
Fuel Cell Vehicle Transient Power 95
Energy Storage Requirements 95
Driving cycle study 97
Power Flow Determination: 99
Motor Control Method 99
Cathode Catalyst Development for Solid Oxide Fuel Cell 100
Thermodynamic and Kinetic Stability of La1-xSrxMnO3-d Perovskites 100
Determination of LSM Chemical Compatibility with the Y-ZrO2 Electrolyte 102
Determination of LSM Mechanical Compatibility with the Y-ZrO2 Electrolyte 103
Measurements of Conductivity and Area Specific Resistance 104
Chapter 4 – Summary and Recommendations 110
Ultralow Platinum Catalysis 110
Membrane Electrode Assembly (MEA) Performance 110
Multi-Cell Analysis and Validation 111
Bipolar Plates 111
Hybrid Power 111
New Cathode Materials 112
References 112
Appendix A - List of Intellectual Property Developed from the Grant 121
Appendix B - List of Articles Published 122
Appendix C - List of Papers Presented in Meetings/Conferences 123
Appendix D - List of Thesis/Dissertations 125

List of Figures

1. Schematic diagram of a fuel cell

2. Tri-layer Fuel cell with the series of bipolar plates

3. Example of power system structure for the fuel cell vehicle

4. Electrochemically active reaction regions for current LSM and advanced MIEC cathodes.

5. Structural formula of the mixed-valence platinum-phosphate blue (PPB).

6. Extended X-ray structure of a polymeric pyrophophato platinum complex. The amine ligand is trans-1,2 diamine-cyclohexane. Two strands of polymeric chains are connected by hydrogen bonds

7. Cyclic Voltammograms of platinum phosphate blue (2.0 mM) at pH 6.0 in 0.50 M $NaClO_4$. The voltammograms were recorded at a sweep rate of 100 mV/s with a carbon rod as the working and Ag/AgCl as the reference electrodes. The first cycle shows negligible electroactivity while the subsequent cycles clearly exhibit reduction and oxidation waves with increasing current densities.

8. Cyclic Voltammograms(a, left) of platinum phosphate blue (2.0 mM) at pH 6.0 in 0.50 M $NaClO_4$ solution with a platinum wire working electrode at 100 mV/s sweep rate. Reduction and oxidation waves were clearly observed from the very first cycle with no significant changes in the current densities in subsequent cycles; Cyclic voltammogram (b, right) of phosphate blue (2.0 mM) at pH 6.0 in 0.50 M $NaClO_4$ by using a platinum-coated carbon electrode.

9. Comparison cyclic voltammograms of $Fe(CN)_6^{2-/3-}$ redox couple using a platinum wire (a, left) and a platinum-coated carbon electrode (b, right) in 0.50 M $NaClO_4$ at pH 2.0.

10. SEM image of a platinum-coated carbon surface (0.05 mg_{pt}/cm^2 on carbon rod) using platinum phosphate blue.

11. Gambit modeling for the bipolar plate designs.

12. Computational mesh for different channel designs.

13. Straight-channel plate – cathode side (blue) and anode headers (red).

14. Typical transient finite element results for temperature and stress distributions in the bipolar plate test section.

15. Test facility for evaluating bi-polar plates.

16. LabView data Acquisition display window.

17. Schematic diagram for preparing membrane electrode assembly by using PPB thin-film as cathode and commercial catalyst (40 wt% Pt/C) as the anode.

18. Schematic of the polymer electrolyte fuel cell stack.

19. Load profile for the stack dynamic stress test.

20. Comparison of power requirements based on constant power and constant force acceleration.

21. Torque Control System.

22. Oxygen contents of $La_{1-x}Sr_xMnO_{3-d}$ perovskites produced in Ar.

23. First step of the synthesis of kinetically stable perovskites.

24. Low-temperature oxygenation of $La_{1-x}Sr_xMnO_{3-d}$ in oxygen.

25. Low-temperature reduction of $La_{1-x}Sr_xMnO_3$ in hydrogen.

26. Schematic design of "in situ" neutron diffraction structural experiments performed on dense tubes using improved Miller furnace as a function of composition, temperature, and oxygen pressure.

27. A graph of current potential curves generated from the thin-film platinum phosphate catalyst on carbon paper (0.08 mg/cm^2) utilizing a three-electrode cell by using a voltage scanning rate 25 mV/s. The total geometric surface area exposed was 1.12 cm^2.

28. graph of net current (oxygen saturated minus argon saturated cells)-potential curve demonstrating the oxygen reduction and presence of additional current after the reduction peak presumably due to water oxidation properties of the thin-film catalyst as in Figure 27.

29. A cyclic voltammogram of oxygen reduction by a platinum phosphate composite catalyst on carbon cloth: the blue curve was recorded in argon while the red curve in the presence of oxygen. The voltage scan rate was 25 mV/s.

30. A cyclic voltammogram of oxygen reduction by a platinum phosphate composite catalyst on carbon rod: the black curve was recorded in argon while the red curve in the presence of oxygen. The voltage scan rate was 5 mV/s and geometric area was 0.713 cm^2. Similar features were observed for all scan rates from 10-100 mV/s expect that currents were higher for higher scan rates.

31. Cyclic voltammograms of an oxygen reduction reaction on commercial Pt- catalysts with comparable loadings as in Figure 27: the black curve was recorded in argon while the red curve in the presence of oxygen.

32. A graph of a rotating disk electrode voltammetry (900 rpm) of oxygen reduction by platinum phosphate composite catalyst (0.09 mg/cm^2; geometric surface area 0.196 cm2):

the blue curves are recorded in argon, red curves in oxygen, and the yellow curves are the net current due to oxygen reduction, and note that red and yellow curves overlapped due to the absence of platinum oxide layer.

33. A graph of rotating disk voltammetry of oxygen reduction by a commercial catalyst (0.25 mg Pt/cm^2; geometric surface area 0.196 cm2) (Alfa Aesar, 40 wt% Pt/C) at 1600 rpm: the blue curves are recorded in argon, red curves in oxygen, and the yellow curves are the net current due to oxygen reduction.

34. A graph of hydrogen adsorption/desorption behavior (blue curve) for a platinum phosphate composite with predominant mixed valence platinum (II,III) species. The voltage scan rate was 10 mV/s.

35. A graph of hydrogen adsorption behavior (black curve) for a platinum phosphate composite catalyst that contains 2/3 platinum metal and 1/3 mixed valence platinum (II,III) species. The voltage scan rate was 25 mV/s.

36. A graph of rotating disk voltammetry (1600 rpm) of oxygen reduction by platinum phosphate composite catalyst composed of predominantly mixed-valence species (0.05 mg/cm^2) and augmented by ruthenium (<0.02 mg/cm^2).

37. A graph of rotating disk voltammetry (1600 rpm) of oxygen reduction by platinum phosphate composite catalyst composed of predominantly mixed-valence species (0.05 mg/cm2; geometric area 0.196 cm2) and augmented by iron (<0.02 mg/cm2).

38. A current-voltage diagram for methanol oxidation by a platinum phosphate composite catalyst (pink) (0.08 mg/cm2) on carbon rod and by bare platinum metal (blue) of platinum oxide for the conventional platinum metal.

39. X-ray photoelectron spectroscopy (XPS) of nano-porous Boron carbide micro-spheres (BCMS).

40. SEM micrograph of novel nanoporous Boron Carbide Micro-Sphere (BCMS).

41. The thermal oxidation comparison of Boron-Carbide micro-sphere (BCMS) and carbon nano-tubes (CNT) through Thermo Gravimetric Analysis (TGA) measurement.

42. Four channel bipolar plate design with pressure contours.

43. Comparison of pressure drops for different bipolar plate design.

44. Comparison of simulated results with experimental data.

45. Variation of Nusselt number pressure drop with Reynolds number.

46. Bipolar plate cool down and thermal power of gas flow.

47. Different meshes for PEM fuel cell simulation.

48. Contour plots for hydrogen concentration distribution across the anode channel and anode diffusion layer.

49. Contour plots of oxygen concentration across the cell.

50. Contour plots of temperature across the cell for different current densities.

51. Contour plots of water across the cell at different current densities.

52. PEM fuel cell performance with varying level of Stoichiometric ratios.

53. Polarization curve for different bi-polar plate designs for stoichiometric ratio.

54. Temperature distribution across the bipolar plate.

55. Contour thermal stress plot in a bipolar plate with $1 \times 1 \times 50$mm channel size with current density of 1.4Amp/cm^2

56. A graph of non-Resistance (IR) free and IR free performance curves of membrane electrode assembly (MEA) at 80 degrees C operated on H_2/O_2 at 80/80/80 degrees C of $T_{cell}/T_{cathode\ humidity}/T_{anode\ humidity}$ operated at 100% relative humidity (RH).

57. Non-IR free performance curves of MEA-1, MEA-2, and MEA-3 at 60°C & 80°C operated on H_2/O_2 at 60/60/60°C and 80/80/80°C of $T_{cell}/T_{cathode\ humidity}/T_{anode\ humidity}$. ●-MEA-1 at 80°C ; ■-MEA-2 at 80°C; ▲-MEA-3 at 80°C (hollow symbols represent 60°C performances).

58. Polarization (IR free & non- IR free) curves of MEA-1, MEA-2 & MEA-3 operated on H_2/O_2 at 80/80/80°C of $T_{cell}/T_{cat\ humidity}/T_{anode\ humidity}$. ●-MEA-1 at 80°C; ■-MEA-2 at 80°C; ▲-MEA-3 at 80°C (hollow symbols represent non-IR free performances at 80°C).

59. Performance and power density curves of MEA-1, MEA-2, and MEA-3 operated on H_2/O_2 at 80/80/80°C of $T_{cell}/T_{cat\ humidity}/T_{anode\ at\ 100\%\ RH.}$ ●-power of MEA-1 at 80°C; ■-power of MEA-2 at 80°C; ▲-power of MEA-3 at 80°C (hollow symbols represent the corresponding potentials).

60. SEM image of MEA-2 cross-section showing large variations in the thickness of the cathode.

61. (a) SEM image of MEA-2 cathode cross-section; b) EDX platinum map of MEA-2 cathode for a selected area of Figure 61a; c) EDX fluorine map of MEA-2 for a selected area of Figure 61a.

62. SEM image of MEA-1 cathode cross-section. A few small Pt agglomerates can be seen.

63. SEM image of MEA-3 cross-section.

64. Initial polarization curve of the 10-cell stack. Conditions: Hydrogen/Oxygen, 0.75 bar/0.9 bar, T_{cell}=65°C, T_{H2hum} = 50°C T_{O2hum}= 55°C. Flow rates = 1-1.24 slpm H_2 and 1-1.18 slpm O_2.

65. Initial polarization curve of the 10-cell stack under constant stoichiometric hydrogen and oxygen flows. Conditions: Hydrogen/Oxygen, 0.75 bar/0.9 bar, T_{cell}=65°C, T_{H2hum} = 50°C T_{O2hum}= 55°C. Constant stoichiometric ratio flow rates of 1.05 hydrogen and 2.0 oxygen.

66. Initial individual cell voltages (top) and IR-corrected individual cell voltages as a function of stack current density. Conditions are the same as those for Figure65.

67. IR-corrected individual cell voltages as a function of the logarithm of stack current density. The black line shows the theoretical slope expected for a purely kinetically-controlled reaction. Conditions are the same as those for Fig. 65.

68. (A) Voltage response of the stack to five dynamic stress test cycles. (B) Magnification of the intermediate current steps in the dynamic stress test cycles illustrating performance increase with cycling. (C) Voltage response of stack to 70,000 seconds of dynamic stress testing. (D) Magnification of the high current region of the testing showing voltage degradation at >8,000 seconds.

69. Response of the stack and individual cells and stack to the first 4,000 seconds of dynamic stress test cycling shown in Figure 19.

70. Polarization curves for the stack: Initial performance and performance after 240 hours of dynamic stress testing.

71. Individual cell voltages (top) and iR-corrected individual cell voltages as a function of stack current density after 240 hours of dynamic stress testing. Conditions are the same as those for Figure 65.

72. IR-corrected individual cell voltages as a function of the logarithm of stack current density after 240 hours of dynamic stress testing. The black line shows the theoretical slope expected for a purely kinetically-controlled reaction. Conditions are the same as those for Figure 65.

73. Polarization curves for the stack: Performance after 240 and 480 hours of dynamic stress testing.

74. Individual cell voltages (top) and iR-corrected individual cell voltages as a function of stack current density after 480 hours of dynamic stress testing. Conditions are the same as those for Figure 65.

75. IR-corrected individual cell voltages as a function of the logarithm of stack current density after 480 hours of dynamic stress testing. The black line shows the theoretical slope expected for a purely kinetically-controlled reaction. Conditions are the same as those for Figure 65.

76. Post-mortem photographs of MEA 4 (left) and MEA 5 (middle and right) showing seal degradation.

77. MEA #1: (A) SEM image of a cross-section, (B) SEM image of a section of the cathode layer (a small swath of the GDL is at the bottom of the image), (C) EDX map of F in the cathode layer of the SEM image in (B) showing where the Nafion® is located. (D) EDS map of Pt in the cathode layer in (B).

78. (A) SEM image of a cross-section of MEA #5 and (B) SEM image of the cathode of MEA #7 with an EDX line scan superimposed. The line scan was made by scanning the electron beam from the top of the straight yellow line to the bottom of it. (Red line = carbon, green line = fluorine, pink line = platinum).

79. Battery performance during US06 highway driving cycle.

80. Experimental waveforms from slip control test. Top trace represents speed. Bottom trace represents slip command.

81. Thermogravimetric study of $La_{1-x}Sr_xMnO_3$ stability in air.

82. An example of the "in situ" NPD diffraction patterns.

83. Stability of oxygen ordered phases as a function of oxygen content and temperature for $SrMnO_{3-y}$.

84. Stability of oxygen ordered phases as a function of oxygen content and temperature for $La_{1-x}Sr_xMnO_{3.}$

85. Stability ranges of various oxygen ordered phases as a function of chemical composition and oxygen content for $La_{1-x}Sr_xMnO_{3-d.}$

86. Study of chemical stability of $La_{1-x}Sr_xMnO_3$ and YSZ (3% Y) up to 1000^oC.

87. Thermal end chemical expansion for $SrMnO_{2.6.}$

88. Comparison of thermal expansion coefficients (TEC) of $La_{1-x}Sr_xMnO_3$, $(La,Sr)(Fe,Co)O_{3-d}$ and $La(Ni,Fe)O_3$ with currently used electrolytes.

89. Resistivity and area specific resistance of selected $La_{1-x}Sr_xMnO_3$ cathodes.

90. Low-temperature oxygenation of $Sr(Fe,Mn,Co)O_{3-d.}$

91. Oxygenation temperatures for $Sr(Fe,Mn,Co)O_{3-d}$ system.

92. Low-temperature oxygenation of $La_{1-x}Sr_xFe_{1-y}Co_yO_{3-d.}$

93. Resistivity of TM substituted $SrMnO_{3-d}$ cathode materials.

94. Study of chemical stability of $SrMn_{0.3}Fe_{0.7}O_3$ and YSZ (8% Y).

95. Conductivity and thermal expansion of $LaFe_{0.5}Ni_{0.5}O_{3-d}$.

96. Impedance spectroscopy measurements for $SrMn_{0.3}Fe_{0.7}O_{3-d}$ half-cells at 700^{o}C.

List of Tables

1. Specifications for the H_2 ECOnomy polymer electrolyte fuel cell stack.
2. Current density vs. time for the cycle profile shown in Figure 19.
3. Comparison of MEA-1, MEA-2 and MEA-3 at 60ºC & 80ºC
4. High frequency resistance (mΩ-cm²)
5. High frequency resistance (mΩ-cm²)
6. Hydrogen crossover (mA/cm^2)
7. Pt concentration in the cathode effluent as a function of dynamic stress testing cycling
8. Cell losses and contribution to overall stack loss of 2.039 V at 100 mA/cm² (%)
9. Cell losses at 100 mA/cm² (V) and contribution to overall stack loss of 1.655 V at 100 mA/cm² (%) after 240 hours of dynamic stress testing
10. Cell losses at 100 mA/cm² (V) and contribution to overall stack loss of 1.291 V at 100 mA/cm² (%) after 480 hours of dynamic stress testing
11. Mid-Size SUV Characteristics
12. Battery vs. Ultracapacitor Performance
13. Trends of Battery and Capacitor Masses for Constant Force Case
14. Trends of Battery and Capacitor Masses for Constant Power Case
15. Example design results using Method 1
16. Example design results using Method 2

Abstract

Research team at Northern Illinois University in collaboration with the Argonne National laboratory, has made significant achievements in six areas. First, researchers have shown that platinum loading can be reduced at least by factor of five-fold to below 0.1 mg/cm^2 compared to currently commercially available electro-catalyst without sacrificing oxygen reduction ability. Second, loss of catalytic activities due to surface oxidation can be prevented by the newly designed polymeric metal phosphate catalysts. Third, corrosion of catalyst support surface can be minimized by boron-doped carbon materials. Fourth, performance of Nafion® based MEA can be enhanced by carefully controlling the dynamics of curing process and by adding specific reinforcing materials. Fifth, bipolar plate performance can significantly improve cell performance even at high current densities through the reduction of mass transfer losses. Sixth, new perovskites materials [$La_{1-x}Sr_xMnO_3$ ($x > 0.5$)] with increased oxygen vacancy states were synthesized and characterized. These materials are stable in the temperature range $200 < T < 700^oC$ and exhibited long-term stability below 800^oC. In addition, the NIU-ANL team developed an alternate protocol for accelerated durability tests has been designed.

Acknowledgements

The principal investigator wishes to recognize the lead scientists and coordinators for Northern Illinois University and Argonne National Laboratory, Drs. Anima Bose and Romesh Kumar, respectively, for their technical management of this comprehensive fundamental study. Prof. Petr Vanýsek, NIU Department of Chemistry and Biochemistry, supported Drs. Bose and Kumar with the development and testing of new nano-catalytic electrodes for PEM Cells. Prof. Bogdan Dabrowski, NIU Department of Physics and Director of the NIU Laboratory for Materials Design, explored with ANL the development of cathode materials for fuel cells based on yttrium stabilized ZrO_2 electrolyte. Prof. Pradip Majumdar, NIU Mechanical Engineering, used computational fluid dynamics and heat transfer with ANL to design bi-polar plates through simulation.

The sustained engagement by the FTA technical representative, Sean Ricketson, Transportation Specialist in U.S. Department of Transportation provided the technical team relevant insight from other complimentary FTA efforts. The final report was edited by Dr. Joseph S. Santner to include links to facilitate the location and extraction of specific information among many diverse topics.

Summary

Projected costs of the present fuel cell designs are uneconomical for widespread use. It is critical to develop improved, less expensive electrolytes, fuel and air electrocatalysts and electrodes, and interconnect/bipolar plates. While it is useful to obtain real-world data with state of the art fuel cells, a systems approach to components for fuel, air, heat, and water management is needed to help implement automotive, heavy and light rail mass transit, over the road and other applications.

Key results include:

- Platinum loading can be reduced at least by factor of five-fold to below 0.1 mg/cm^2 compared to currently commercially available electro-catalyst without sacrificing oxygen reduction ability
- Catalytic activities are maintained by the newly designed polymeric metal phosphate catalysts
- Corrosion of catalyst support surface can be minimized by boron-doped carbon materials
- Nafion® based membrane electrode assembly can be enhanced by carefully controlling the dynamics of curing process and by adding specific reinforcing materials
- Bipolar plate performance can significantly improve cell performance even at high current densities through the reduction of mass transfer losses
- New perovskites materials with long-term stability and increased oxygen vacancy states below 800^{o}C were synthesized and characterized [$La_{1-x}Sr_xMnO_3$ ($x > 0.5$)]
- An alternate protocol was designed for accelerated fuel cell durability testing

Recommendations include:

- Polymer electrolyte membrane electrode assembly work should focus on enforcing reagents so they can operate at higher temperatures
- Search for multi-cell gaskets and electrocatalysts needed to meet the demanding durability requirements of the automotive fuel cell must continue
- Improved stack designs need to facilitate reactant transport to the end cells since end cells account for a major portion of the initial performance losses
- Bipolar plate work should concentrate on selection of material of construction relative to cost and manufacturability with prototype design based on simulation.
- validate the utility of new compounds show outstanding thermoelectric characteristics with corroborating measurement of conductivity and thermoelectric power Q

The intellectual property includes five patent applications (Appendix A), 13 publications in national and international journals (Appendix B), 13 presentations in national and international meetings (Appendix C). The explicit effort to nurture the education and training of alternative energy technology workforce critical for the implementation of fuel cell technology partially or fully supported 17 graduate students (Appendix D).

This page is intentionally blank.

Chapter 2 – Methodology and Research Approach

Chapter 2 – Methodology and Research Approach 12
Preparation and Characterization of New Catalysts for PEMFC 13
Chemical Electropolymerization Using Platinum Phosphate Blue 13
Preparation of Mixed-Valence Platinum-Phosphate Matrix Catalyst 17
Preparation of Mixed Metal Composite Catalyst 18
New Catalyst Support: Nano-Porous Boron Carbon Microsphere 18
Bipolar Plate 18
Computational Fluid Dynamics (CFD) Modeling of Bipolar Plate Flow Channel Design and Analysis 19
Fabrication, Testing and Performance Evaluation of Bipolar Plates 20
Data Acquisition Methodology: 22
Data Acquisition Software Implementation 22
Single Cell Performance 23
Preparation of Membrane Electrode Assembly 23
Performance Enhancement within Existing Technology 25
MEA Preparation with Nanocomposite Nafion Membrane 26
Multi-Cell Performance 27
Durability Test Protocol 28
In-Situ Diagnostics 29
Post-Mortem Diagnostics 29
Power Conditioning 29
Acceleration Study 30
Driving cycle study 31
Power Flow Determination 33
Fuel Cell and Other ESU Optimization 33
Battery and Capacitor Optimization 37
Control Law Rules 39
Motor Control Method 39
Solid Oxide Fuel Cell Cathode 41
Synthesis of Samples for Special Experiments 43
Synthesis and Measurement of Mixed Conducting Cathodes 44

Experimental approaches and methodology are described for preparation and characterization of new catalysts for PEMFC, new catalyst support: nano-porous boron carbon microsphere, bipolar plate, single cell performance, multi-cell performance, power conditioning, solid oxide fuel cell cathode, and finally, the synthesis and measurement of mixed conducting cathodes.

Preparation and Characterization of New Catalysts for PEMFC

To reduce the cost of PEMFC it is necessary to reduce the platinum group metals (PGM) especially platinum (Pt) as catalyst. We have developed new method, chemical electropolymerization which allows us to reduce the amount of pt loading in the catalyst from 0.5 mg_{pt}/cm^2 to below 0.1 mg_{pt}/cm^2.

Chemical Electropolymerization Using Platinum Phosphate Blue

To create a thin-film platinum surfaces with nano-layer thickness on carbon substrates rather than using a bulk catalyst, we have exploited the redox chemistry of mixed-valence platinum phosphate blue, a mixed-valence Pt(II)-Pt(III) tetramer with an average oxidation state of +2.25 (Figure 5) [86,87], and incorporated it on a variety of carbon surfaces.

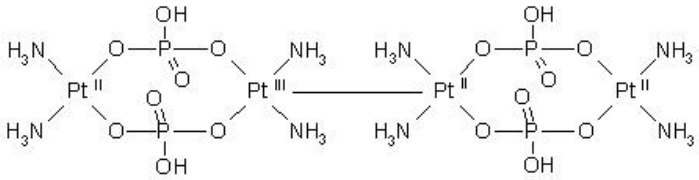

Figure 5: Structural formula of the mixed-valence platinum-phosphate blue (PPB).

The phosphate blue is a tetrameric species that remains in solution at lower pH but becomes a robust insoluble material in its polymerized form. A recent X-ray crystal structure of a dinuclear platinum(II,II)pyrophosphate-bridged complex, similar to the building block of the phosphate-bridged complex PPB, indicates the extensive polymeric network held by hydrogen bonding (Figure 6) [88]. This tetramer was polymerized on carbon substrates by extending platinum-platinum bond formation through the bridging phosphate network and applying a small positive voltage.

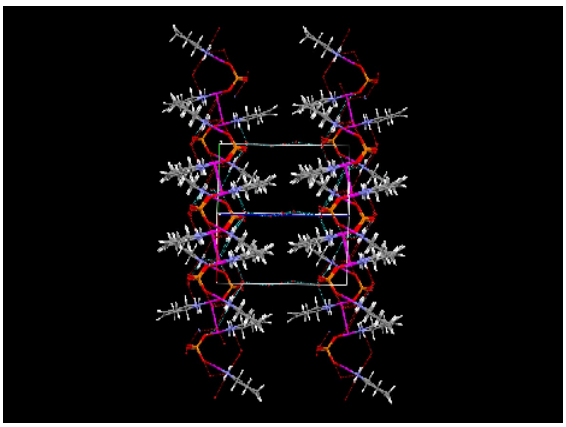

Figure 6: Extended X-ray structure of a polymeric pyrophophato platinum complex. The amine ligand is trans-1,2 diamine-cyclohexane. Two strands of polymeric chains are connected by hydrogen bonds.

Figure 7 shows the cyclic voltammograms recorded by scanning potentials from 0.2 to -1.0 V vs. saturated calomel electrode. As can be seen from the Figure 7, the voltammogram recorded from the first cycle appeared to be almost featureless, displaying only a shoulder at about -0.95 V. This first voltammogram indicates that the phosphate blue is very weakly electroactive at the carbon surface. The next sets of voltammograms clearly exhibited two distinct reduction waves. The potential for the first reduction wave at -0.53 V remained constant while the second wave moved from initial -0.94 V to- 0.72 V. Also distinct is the magnitude of the current for both waves. Magnitudes of current for the redox waves initially increase and finally level off.

These voltammograms were then compared with those obtained with a platinum metal working electrode. Figure 8 shows a typical cyclic voltammogram of the phosphate blue with a platinum metal working electrode. In this voltammogram, two reduction waves and two oxidation waves in the region -0.42 to -0.73 V were observed. Separations between the reduction and oxidation waves indicate quasi reversible redox processes.

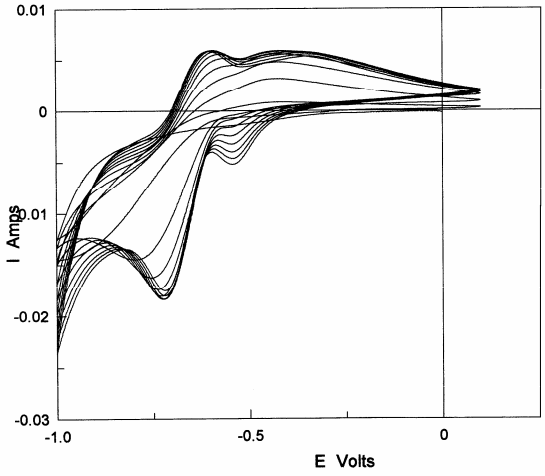

Figure 7: Cyclic Voltammograms of platinum phosphate blue (2.0 mM) at pH 6.0 in 0.50 M $NaClO_4$. The voltammograms were recorded at a sweep rate of 100 mV/s with a carbon rod as the working and Ag/AgCl as the reference electrodes. The first cycle shows negligible electroactivity while the subsequent cycles clearly exhibit reduction and oxidation waves with increasing current densities.

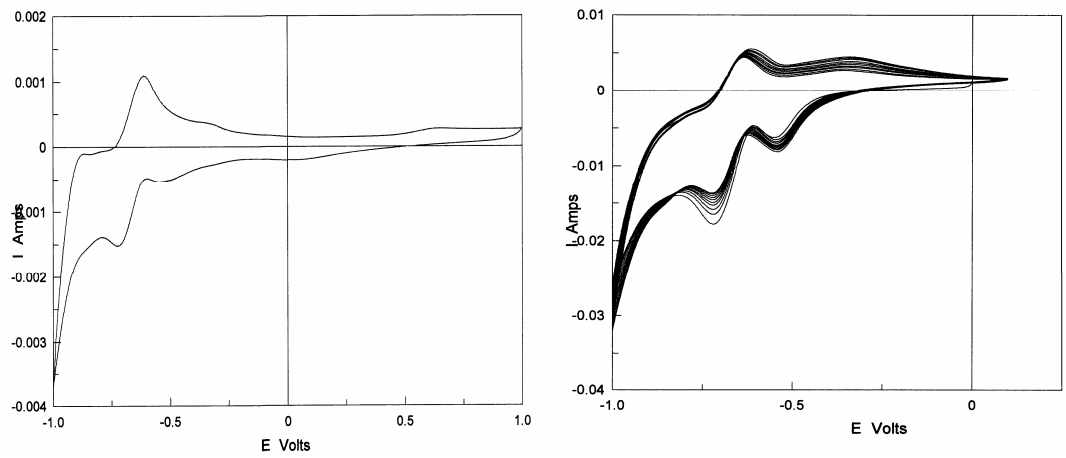

Figure 8: (a, left) Cyclic Voltammograms of platinum phosphate blue (2.0 mM) at pH 6.0 in 0.50 M $NaClO_4$ solution with a platinum wire working electrode at 100 mV/s sweep rate. Reduction and oxidation waves were clearly observed from the very first cycle with no significant changes in the current densities in subsequent cycles; (b, right) Cyclic voltammogram of phosphate blue (2.0 mM) at pH 6.0 in 0.50 M $NaClO_4$ by using a platinum-coated carbon electrode.

Next, platinum coated carbon electrodes were cleaned in 2.0 M perchloric acidic solution and then reused to record volttammograms of the blue. These voltammograms recorded with platinum coated carbon electrodes as the working electrode exhibited identical features to those obtained with platinum metal working electrodes. Furthermore, repetitive scans using the platinum coated carbon electrodes exhibited conventional voltammetry (Figure 8b) in that a small decrease in current was observed over repetitive scans due to the depletion of the electroactive species at the electrode surface. These data clearly indicate that platinum coated carbon electrodes function like a pure platinum metal electrode. To further demonstrate the utility of the coated electrode as the pure platinum electrode, cyclic voltammograms of $Fe(CN)_6^{3-/2-}$ redox couple were recorded. The voltammogram of the $Fe^{3+/2+}$ couple III/II was identical to that obtained with a platinum metal electrode both in peak positions and peak currents when identical surface areas were used (Figure 9). The equal surface area of the platinum coated carbon electrode was adjusted in the following way. First, the voltammogram of the blue was recorded using a platinum metal working electrode. Then, platinum-coated carbon electrode was dipped in the same solution and the depth of the electrode insertion was adjusted until it reached to the same current level as measured at a potential away from the oxidation and reduction waves.

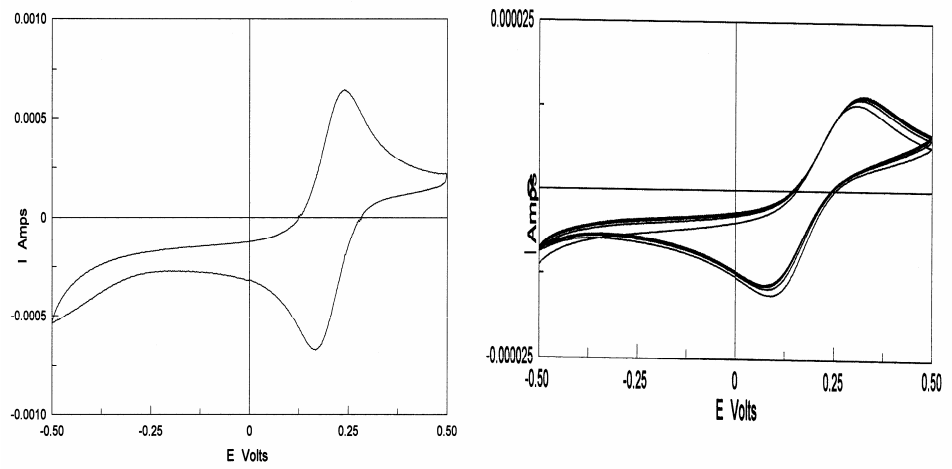

Figure 9: Comparison cyclic voltammograms of $Fe(CN)_6^{2-/3-}$ redox couple using a platinum wire (a, left) and a platinum-coated carbon electrode (b, right) in 0.50 M $NaClO_4$ at pH 2.0.

To demonstrate the ability to irreversibly coat platinum on other carbon surfaces, carbon papers were used as working electrodes. Here again, the first cycle was distinctly different from the subsequent cycles as observed for the graphite surface. However, these voltammograms show a greater degree of irreversibility in that the cathodic to anodic current ratios were larger for the carbon paper, indicating even more efficient electrodepositions on the carbon paper.

The degree of coating was measured by quantitative analysis of platinum content as a function of the number of cycles. As expected, platinum loading depended on the concentration of the blue solutions and the number of cycles employed in recording voltammograms. These determinations reveal that when 2.0 mM solution was used, the loading varies between 0.03 mg_{pt}/cm^2 to 0.22 mg_{pt}/cm^2 with five and twenty cycles. Furthermore, the highest loading represents the saturation point as no further increase in loading was observed. The electron microscopy of the 0.05 mg/cm^2 loaded sample reveal formation of platinum monolayer (Figure 10).

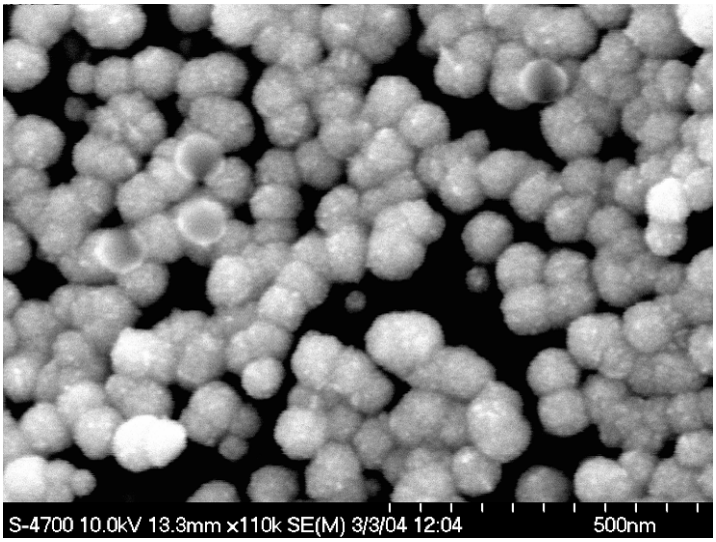

Figure 10: SEM image of a platinum-coated carbon surface (0.05 mg/cm2 on carbon rod) using platinum phosphate blue.

Preparation of Mixed-Valence Platinum-Phosphate Matrix Catalyst

Platinum phosphate composite thin-films surfaces on carbon support are prepared from electropolymerization and reductive electropolymerization of platinum phosphate blue by cycling voltages between two predetermined values as described below. Typically, a three-electrode cell with a variety carbon surfaces as a working electrode, saturated calomel or Ag/AgCl as a reference electrode, and a platinum wire as an auxiliary electrode was used to prepare thin-film surfaces. The carbon surfaces include graphite carbon, carbon papers, carbon powder (Vulcan XC72R) on carbon cloth, and carbon cloths (E-TeK). To prepare the catalyst on carbon surfaces, three-electrode cells contained 1.0 to 5.0 mM platinum phosphate blue solution in 0.5 M NaClO4 at pH 4 to 5. Thin-films of different platinum loadings (0.03 to 0.22 mg_{pt}/cm^2) were prepared by cycling voltage from 1.0 to -1.0 V vs. Ag/AgCl with different scan rates, 5 mV/s to 50 mV/s. Other potential ranges between 0.8 to -0.8 V, 0.5 to -0.5 V, vs. Ag/AgCl were also used in conjunction with scan rates 5 to 50 mV/s to deposit the thin-film. An ink was prepared by emulsifying the carbon powder in 30 wt% Nafion (from 5 wt% Nafion solution purchased from Dupont, (DE 521 an ionomer) in isopropyl alcohol for 5-7 days. The resulting ink was then coated on a tip of rotating disk electrode and dried under an IR lamp. The mixed-valence platinum phosphate thin-film was then deposited on to the dried carbon-Nafion matrix substrate by cycling the voltage stated above. The selection of number of cycles, scan rates, and starting concentrations of the precursor complex controlled the desired platinum loading of the thin-film surfaces.

This unique method of thin-film formation is described in an earlier patent application [89] and published in the Journal of the Power Sources [90]. However, the previous patent application and subsequent publication dealt with making thin-film of metal surfaces by completely reducing metal ions. The current application entails making composite surfaces with a variety of oxidation states and demonstrating the applications of these composite thin-films in fuel cell systems. In making these composite surfaces, the adsorption properties and complex electrochemistry of the phosphate blue precursor complex have been exploited. For example, the mixed valence Pt_2(II,III) species is easily polymerized on carbon surface by applying voltage <-0.4 V, reduced

to Pt(II,II) at -0.72 V, and completely reduced to platinum metal at potential below -0.97 V vs. Ag/AgCl . The same mixed valence species can be oxidized to Pt_2(III,III) at voltage >0.5 V. Therefore, by selecting specific range of potentials, composite surfaces of desired oxidation states can be prepared. Moreover, the cycling technique allows to discard any loosely bound platinum species by oxidizing the surface at positive potentials.

The platinum content was quantitatively estimated by atomic absorption spectroscopy and the amount of phosphate was determined as phosphomolybdate. These estimations revealed that depending on the range of voltage selected, the platinum/phosphate ratio varies. For example, the composite catalyst shows 1:1 platinum:phosphate ratio for the catalyst generated by scanning potential between 0.5 to -0.5 V. vs. Ag/AgCl while those prepared from 1.0 to -1.0 V vs. Ag/AgCl yielded phosphate/Pt ration as low as 0.3 on carbon road. The composite catalysts prepared by scanning 0.5 to -0.5 V predominantly yielded mixed-valence Pt_2(II,III) species. On the other hand, potential range 0.8 to -0.8 V afforded a combination of Pt_2(II,III) and Pt_2(III,III) along with small fraction of platinum metal. Finally, the scanning of wider potential range such as 1.0 to -1.0 or higher (both positive and negative) yielded significant amount of platinum metal along with Pt_2(II,III) and Pt_2(III,III).

Preparation of Mixed Metal Composite Catalyst

Once the platinum-phosphate is anchored, the surfaces were further coated with other metals in the following manner. In this process, a platinum coated electrode was used as a working electrode and desired metals were deposited from dilute solutions (2-5 mM) from their respective metal salts via scanning potential from -1 to 1 V vs. Ag/AgCl. For example, Fe(III) acetate, Co(III) acetate/phosphate, Pd(II) chloride, Ru(III) chloride were used to coat respective metals. The extent of coating can be manipulated by the choice of concentration of the metallic salts and the number of cycles for coating them.

New Catalyst Support: Nano-Porous Boron Carbon Microsphere

*C*arbon support corrosion in the fuel cell operation results the effective surface area loss that has been clearly noticed even in early 90's. In order to prevent the sintering of Pt nanoparticles, the nanoparticles have to be stabilized on the support materials; development of advanced supporting materials that are more stable and with enhanced interaction with Pt particles is highly desirable.

Boron doping into carbon materials has been known to change the physical and chemical properties of carbon [91-95]. Studies have found that boron is a unique and effective dopant for improving the oxidation resistance of graphite, carbon fibers, carbon/carbon composites, carbon nanotubes and various other carbon materials [96, 97].

A new class of new material, Nanoporous Boron Carbon microspheres (BCMS) were prepared by a chemical vapor deposition process in a temperature gradient environment from boron salt with specific in hydrocarbon solvents. The details of synthesis are not presented here since a patent application is in process. These novel BCMS material were characterized through high resolution scanning electron microscopy (SEM), X-ray photoelectron spectroscopy (XPS), Nitrogen Adsorption measurement, and Thermo Gravimetric Analysis (TGA) measurement.

Bipolar Plate

As indicated in the Introductionsection about bipolar plate, one of the objectives was to design and develop bi-polar plates with enhanced heat and mass transport characteristics with limited

increase in pressure drop characteristics by using computer simulations and experiments. This part of the project is consisted of three parts. Part 1 discusses Computational Fluid Dynamics (CFD) modeling of bipolar plate flow channel design. Part 2 addresses fabrication and testing of bipolar plates to validate computation model as well as characterization of steady and transient heat dissipation capacity. Part 3 explores the development of PEM fuel cell. A simulation model hypothesizes the internal performance mechanisms of the PEM cell and evaluate the effect of bipolar plate designs on mass transfer losses on PEM fuel cell performance.

Computational Fluid Dynamics (CFD) Modeling of Bipolar Plate Flow Channel Design and Analysis

Different bipolar plate designs are considered and analyzed using computation fluid dynamics model. These designs include straight-parallel channels of different sizes, single serpentine channels with square and curvilinear bends, and multiple parallel serpentine channels. Computational fluid dynamics analysis is performed using Fluent Commercial code to evaluate velocity, pressure, heat and mass transfer effectiveness of these channels. A few of these designs created in Gambit are shown in Figure 11.

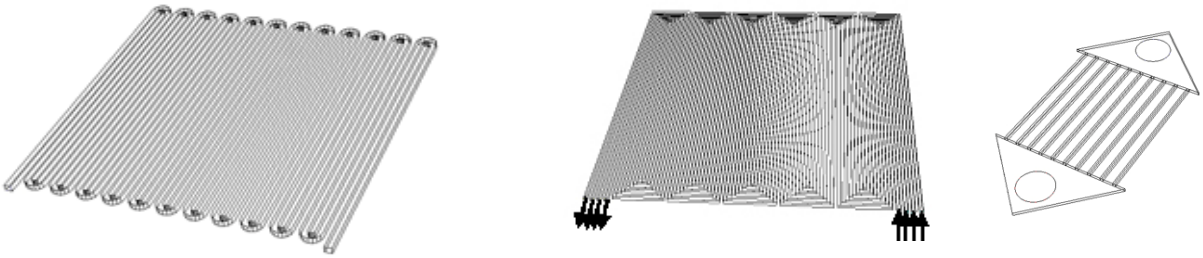

a) Serpentine channels with circular bends

b) multiple serpentine channels

c) Straight channels

Figure 11: Gambit modeling for the bipolar plate designs.

Meshing in gambit is generated using mapped meshing in order to achieve prescribed control volume shape and a regulated order of spacing in circular and corner edges according to the length of the edge and free meshing is used for the edges along the channel, and volume meshing. . The meshing is uniform throughout the model except it is more refined near the walls. Figure 12 shows typical meshes for the bend and straight sections of the channel.

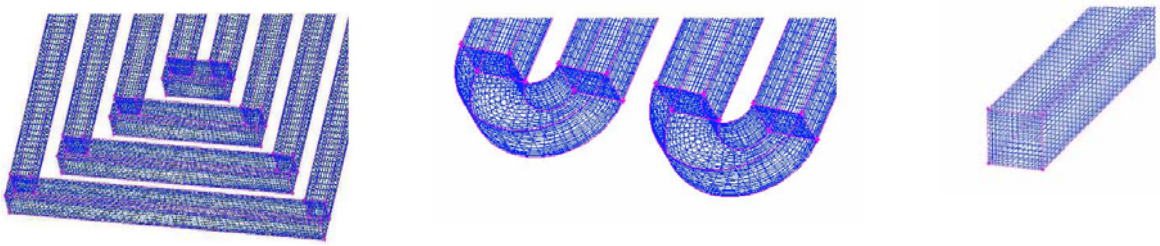

a) Multiple channel corners meshing

b) Serpentine circular corner meshing

c) Straight channel meshing

Figure 12: Computational mesh for different channel designs

Fabrication, Testing and Performance Evaluation of Bipolar Plates

This work builds upon the continuing simulation research at NIU for the development of bipolar plates through computer simulation modeling of high performance gas flow channel

designs. A number of potential bipolar plate designs are proposed and simulated computationally. The primary focus of this part of the study has consisted of experimental validation of these computer models, both in terms of convective and thermal performance. A test facility and test sections is designed and fabricated for experimentally evaluating bipolar plates. These test sections are heated electrically to impose simulated thermal conditions for fuel cell operation. Additionally, the heat dissipation characteristics of the bipolar plate material are evaluated under steady state and transient conditions. Figure 13 show one of the design being considered for fabrication and testing.

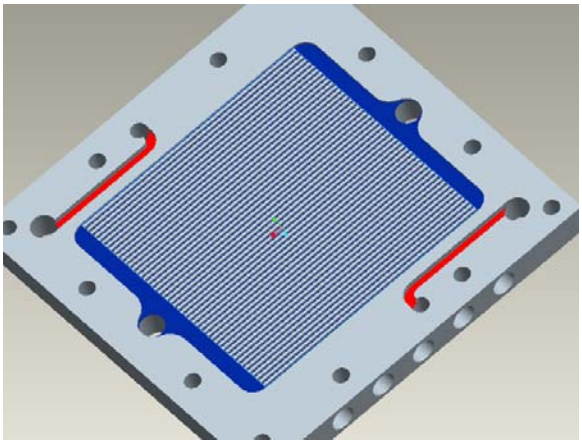

Figure 13: Straight-channel plate with cathode side (blue) and anode headers (red)

Finite element simulation of the model is carried out for this design in terms temperature distribution and thermal stress to achieve the desirable simulated heating conditions comparable to the operating current density range considered for PEM fuel cell design. For this model a transient thermal simulation was carried out and allowed to run until the surface temperature of the plate passed 100^{O}C. For the straight channel model this occurred after 480 seconds. Given the resulting temperature variation with time result the instantaneous temperature sets were selected at 60 second intervals and used as thermal conditions for static stress analysis. Figure 14 show typical transient temperature and stress distribution in the plate.

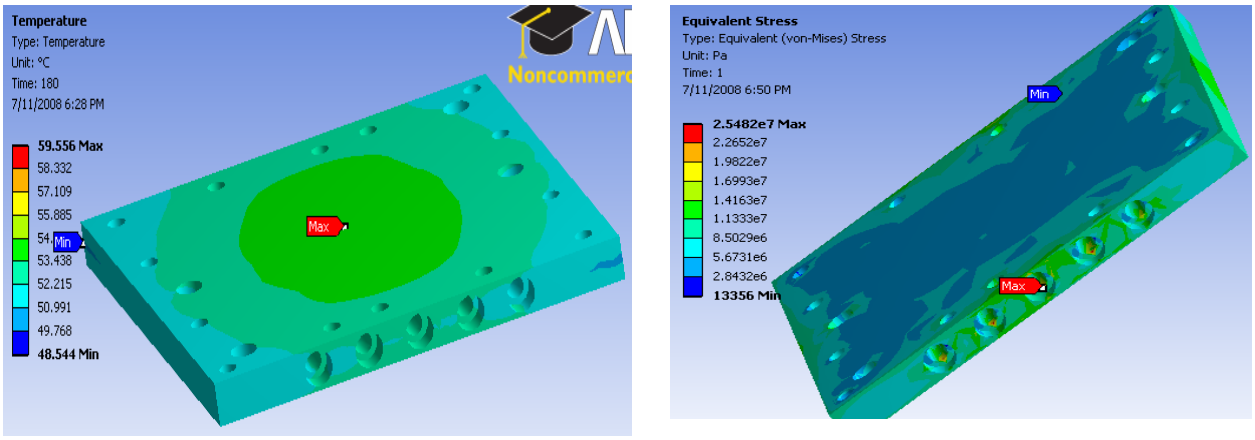

(a) Plate Temperature – 180s (b) Plate Stress – 180s

Figure 14: Typical transient finite element results for temperature and stress distributions in the bipolar plate test section

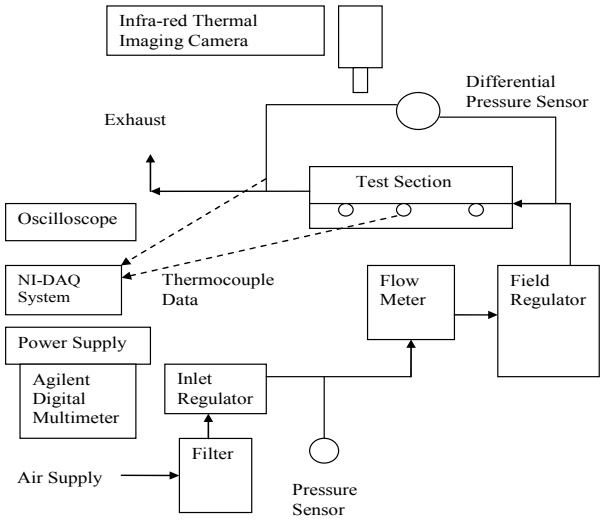

Schematic of test facility Photo of test facility

Figure 15: Test facility for evaluating bi-polar plates.

Given their importance it is valuable to develop flexible testing methodologies for examining in new plate designs operating under simulated stack conditions. A test facility equipped with temperature and pressure sensors, flow-meters/controllers, heaters, multimeter, oscilloscope and power supply has been designed and fabricated for experimentally evaluating bipolar plates at NIU. A schematic diagram and a photograph of the test facility are shown in Figure 15.

A computer data acquisition system with LabView graphical software is used to control the operation of the heater feed-back circuit, collection and sampling of the data, and monitoring the test operation. An infrared thermal imaging system is also used to measure surface temperature

of the test section to evaluate heat dissipation capacity of bipolar plate design and material construction. Test sections are made of stainless steel to conduct test under both isothermal and non-isothermal conditions. For non-isothermal tests, the test sections are mounted on a copper block heated with electric cartridge heaters to impose simulated heating conditions for bipolar plate under different operating current densities. The heater block was designed based on the design generated by the final set of simulations. It is fitted with embedded thermocouples to measure the field temperature. Pressure drop and heat transfer coefficient are computed for a wide range of Reynolds number, calculated based on a selected stiochiometric ratio and a range of current density applicable to automobile. Results are used to validate the computational model used for the design evaluation of bipolar plates.

Data Acquisition Methodology:

Thermocouple junction voltage and cold-junction thermistor resistance is collected using a multiplexed scan at 100Hz. Each of these channels is averaged over 100 samples to produce a one second average for transmission to the secondary DAQ system over a one-way RS232 serial link configured for 9800 baud transmission rate.

The receiving system waits until the full thermal data packet has arrived, and then proceeds to trigger acquisition of the flow and thermal data. Only after these values have been obtained does it decode the raw junction voltage data and confirm its checksum. This is done to minimize timing error relative to the two acquisitions. Once all data is collected it is run through its calibration routines for display. As the power and flow are under manual control the determination of when the system is operating under steady-state conditions has also been left to the operator's discretion. Moving averages of the rates of change of temperature readings are provided to assist in this, but the operator is required to flag periods of steady operation for averaging in the post processing stage. A timeout counter has been provided to guarantee constant sample windows for easier statistical analysis.

Time, temperature, pressure, flow, barometric, and steady flag are all recorded as printable text in an Excel-compatible Comma Separated Value (CSV) file. This can be used directly for Excel-based post-processing, however such formats are unwieldy from the standpoint of automated LabVIEW-based data reduction programs. As much of the data reduction is handled by such code the capture code additionally outputs a memory dump of its internal data structure. This binary data is encoded as printable text using the same MIME base64 encoding used by the serial link and encoded into the CSV file. This maintains the readability advantages of the CSV format, allows all data from a run to continue to be stored in a single file, and is easy and accurate for the post-processing routines to parse.

Data Acquisition Software Implementation

Both the primary and secondary DAQ routines were implemented in National Instruments LabVIEW. (Versions 4.1 and 8.0 respectively.) As no such routines exist in LabVIEW both systems had their base64 functionality implemented as LabVIEW wrappers around a compiled Windows DLL which contained the encoding and decoding routines necessary. These routines were written in ISO C89 and compiled using GCC 3.4 against the MinGW runtime libraries; targeting win32. Figure 16 shows the LabVIEW data acquisition display and monitoring window.

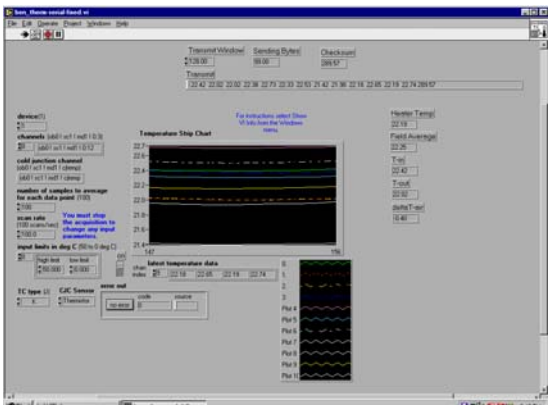

Primary data acquisition interface

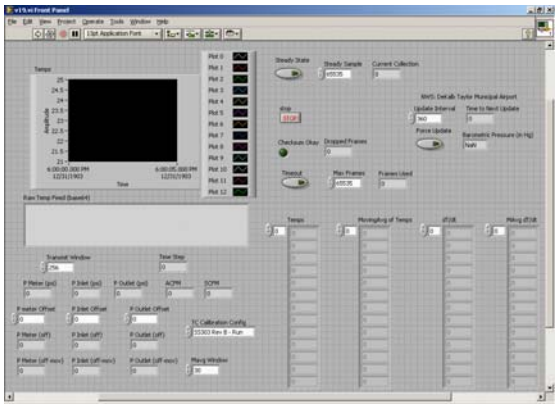

Secondary data acquisition interface

Figure 16: LabView data acquisition display window

Simulation of a PEM Fuel Cell with designed Bipolar Plates

In order to evaluate effect of the bipolar plate design on the PEM fuel cell performance in terms of mass transfer losses at higher current density, computational model for the simulation of Polymer Electrolyte Membrane (PEM) fuel cell is developed. The model includes combined heat and mass transfer processes due to convection and diffusion in the gas flow channels as well in the gas diffusion layers of the electrodes, and associated electrochemical reactions in a tri-layer PEM fuel cell design. For water transport, Electro-osmotic drag, convection and diffusion and temperature dependent membrane properties are considered. This simulation model is needed to evaluate and finalized with the proposed bipolar plate design, evaluate state-of-the-art materials for gas diffusion layers/electrodes, polymer electrolyte membrane, and catalyst loading. In order to demonstrate the overall balance and hence accuracy of the computational solution, fluxes of all reactant gases, water and heat are estimated at all faces of the computational domain and checked for overall balance. Results show good balance between the consumption rate of oxygen, hydrogen, heat and water. A mesh refinement study is conducted to ensure the effectiveness of the mesh and show the sensitivity, computational accuracy and convergence of the PEM fuel cell simulation model.

Single Cell Performance

Preparation of Membrane Electrode Assembly

Membrane electrode assemblies (MEAs) of 5 cm2 active area were prepared from Nafion-115, three different cathodes Gas Diffusion Electrodes (GDE), and a common anode electrode as described below. First GDE was prepared from the carbon-ionomer ink described above on wet-proof carbon cloth substrate. After spraying the ink on wet-proof carbon cloth, composite catalyst of desired loading was accomplished by electropolymerization on the ionomer-carbon surface as described above. Second, carbon cloth (E-Tek) with no wet proofing was wet-proofed by dipping in a solution of PVDF (polyvinylidene fluoride) and NMP (N-methypyrrolidine) and stirred for approximately 4 hours. Carbon cloth was then taken out of the dispersion and dried in

a conventional oven at temperatures of 150 ºC for about 2 hours to remove any solvent remaining on the surface of the cloth.

To localize the Pt particles on the electrode surface and to have a good three-phase interface, the following ink was prepared and sprayed: Vulcan carbon XC 72 R was treated in an oven at 280 ºC for 2 hours to remove any organic matter. The pretreated carbon was then mixed with 10 weight % PVDF, which was first dissolved in NMP solution to ensure that the PVDF is completely dissolved, and doesn't form any clusters with carbon ink. Three milliliters of isopropanol were mixed with the solution. 20 weight % of 5 weight % Nafion solution was also poured into the solution and was allowed to stir on the hot plate overnight. The resulting mixture was then applied on the dried wet-proofed carbon cloth; the weight of the mixture deposited was observed to be 15 mg.

The leftover mixture was then mixed with glycerol and applied on the surface of the cloth to make the surface of the cloth hydrophilic in nature. The weight of the mixture deposited was observed to be around 5 mg. Then the cloth was dried in the oven at 250 ºC for 2 hours. The un-catalyzed carbon electrode was then coated with platinum using the electro-polymerization technique with 5 mV/s scan rate and 10 cycles from 2.8 mM precursor complex solution. After the electro-polymerization the electrode was dried in the oven at 150 ºC for 2 hours. The electro-polymerized electrode was then impregnated with the Nafion dispersion by spraying. This was followed by drying at 80º C for 2 hours. Third, electrocatalyst was loaded directly on non-wet-proofed carbon cloth (E-Tek) using the electro-polymerization technique for the cathode catalyst preparation as illustrated in Figure 17.

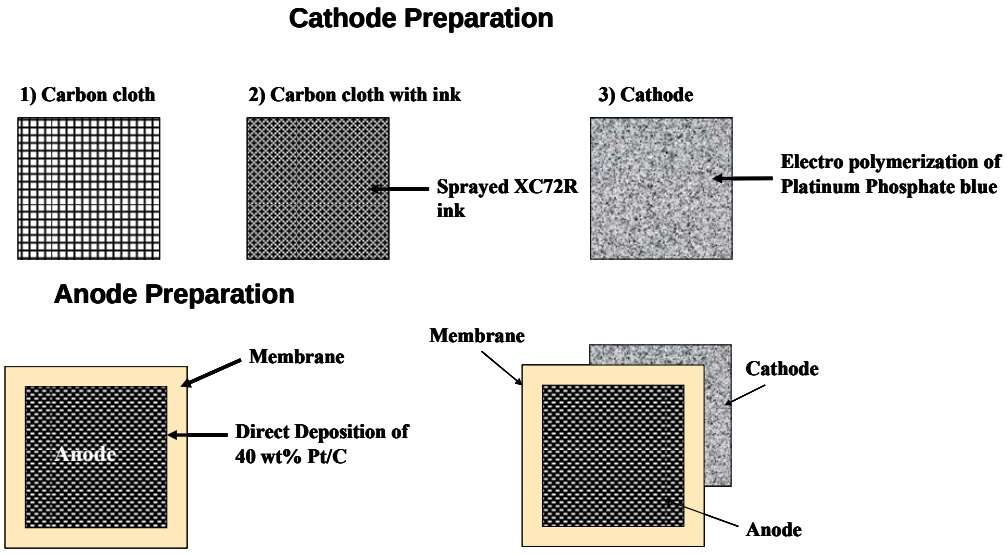

Figure 17: Schematic diagram for preparing membrane electrode assembly by using PPB thin-film as cathode and commercial catalyst (40 wt% Pt/C) as the anode.

For the anode, commercially available catalyst was used. The catalyst ink was directly sprayed on the as-purchased Nafion® 115 membrane, without any pre-treatment, using the spray gun under a high voltage infrared lamp. The catalyst ink was prepared by adding 3 mL of deionized water to 0.5 g of 40 weight % Pt/C (Alfa Asear) and stirred in an ultrasonicator for one minute. Five strokes of spray were made on the membrane, with a five-minute time interval between

each spray. The resulting weight of the deposited mixture was approximately 4-5 mg, which gave a Pt loading of 0.25mg/cm^2. The Nafion® membrane with the anode electrolyte sprayed was then taken to the hot press, along with the prepared GDE, which was kept on the other side of the membrane as cathode.

The whole assembly was pressed at 150 ºC for 5 minutes at 1000 pounds over a 36-square-inch plate.

Performance Enhancement within Existing Technology

We have also investigated the variation of cell performance within existing technology using commercially available catalyst and ionomer are: Pt/C catalyst, Nafion® ionomer, and Nafion® membrane electrolyte [55]. In particular, we have prepared several sets of MEAs and three such sets with almost identical compositions using different curing conditions, measured their performances, determined their structural features by SEM and EDX, and correlated that with the observed performance. In studying key factors that control the performance of MEAs, several MEAs with 5 cm^2 active area were prepared by depositing 40 wt% Pt/C (Alfa Aesar) catalyst mixed with Nafion® onto homemade Nafion® membranes that were prepared using 5 wt% Nafion® solution (DE 521, DuPont). Several sets of MEAs were prepared using the same batch of in-house prepared membrane, but results of two sets abbreviated as MEA-1 and MEA-2, are presented in the results section. The third set of MEAs (MEA-3) was fabricated from a separate batch of in-house prepared membrane. The in-house membranes were prepared using the following procedure. First, the membranes were cast using a 5% Nafion® solution, and then boiled in 3 M H_2O_2 for an hour, followed by a boiling in 5% H_2SO_4 for an hour. Finally, the membranes were boiled in de-ionized water for an hour to remove excess acid. The thicknesses of the membranes are 30 μm for MEA-1 and MEA-2, and 20 μm for MEA-3. The application of the electrode inks was identical within the experimental error; however, the curing conditions were different as described below.

The MEAs were prepared by direct deposition of the catalyst ink onto the membranes using a spray gun (Badger Airbrush: 155-1). The ink was deposited onto both sides of the membrane with anode and cathode catalyst loadings of 0.25 mg Pt/cm^2 and 0.50 mg Pt/cm^2, respectively. The catalyst loadings were maintained at the same level for all three MEAs and the same catalyst-ionomer ink batch was used for all three MEAs as well. The ratio of Pt/C catalyst to Nafion® solution used in the ink resulted in electrodes with 30 wt% ionomer content. The catalyst-ionomer ink was prepared by mixing 3 mL of deionized water with 0.5 g of 40 wt% Pt/C in an ultrasonic bath for one minute. Seven milliliters of isopropyl alcohol was then mixed with the solution, followed by mixing in the 5 wt% Nafion® solution at 30 wt% with respect to the Pt/C. Lastly, the solution was left to stir for 24 hours before use. After spraying the ink onto the membranes, the solvent was evaporated in a controlled manner under an IR-lamp. The curing conditions were varied by 1) changing the distance between the MEA and the IR lamp, resulting in different MEA temperatures and 2) changing the amount of time between two consecutive sprays. During the catalyst deposition for MEA-1 and MEA-3, the solvent evaporation time was 8 to 10 minutes between two consecutive sprays. After each spray, the catalyst layer was dried under the IR lamp at a temperature of ~50°C. The solvent evaporation time between the two consecutive sprays of catalyst ink onto MEA-2 was reduced to 5 minutes and the drying temperature was increased to ~60°C by reducing the distance between the IR lamp and the MEA. After spraying the ink on both sides of the membrane to deposit the designated amounts of Pt/C

for the anode and cathode, the MEAs were hot-pressed at 120 ºC for 10 minutes under 1000 pounds of pressure (Carver 3853-0 Model C).

The performance measurements of all above mentioned MEAs were conducted at 60°C and 80°C using a flow rate of 0.2 L/min for both H_2 and O_2 with an operating pressure of 30 psi, and with both gases humidified to 100% relative humidity using a Fuel Cell Test Station 890CL (Scribner Associates Inc.). For the cathode electrochemically-active surface area (ECSA) measurements, a typical half-cell configuration was used by passing nitrogen at the cathode and hydrogen at the anode. The ECSA measurements were made between 0 and 0.8 V using Corrware software (Scribner Associates Inc.) and an SI 1287 (Solatron Analytical) potentiostat at scan rate 30mV/s. The ECSAs were calculated using the charge generated from hydrogen adsorption/desorption and the well-known charge for hydrogen adsorption of 210 μC/cm²-Pt [98]. One common practice of preparing MEAs for SEM investigation is to cut the MEAs after freezing them in liquid nitrogen [99]. However, elemental mapping by energy dispersive x-ray spectroscopy (EDX) requires a surface that is polished flat in order to achieve results with the highest reliability. For our SEM investigation, a piece from each MEA was cast in a polyester resin (Castolite, LECO Corp.) and polished using standard polishing techniques for polymers and plastics [100]. The samples were oriented such that a cross-sectional view of the MEAs was revealed. The samples were then examined in an SEM (JEOL JSM-6400) using energy dispersive X-ray spectroscopy (EDX, Oxford) for elemental mapping.

MEA Preparation with Nanocomposite Nafion Membrane

We have also prepared composite Nafion membrane by adding reinforcing agents to increase the mechanical and thermal stability to operate at higher temperatures. Due to the propriety and preliminary nature of this work, details are not presented here. However, acknowledgements of DOT support will be made for future publications and disclosures on this composite Nafion membrane.

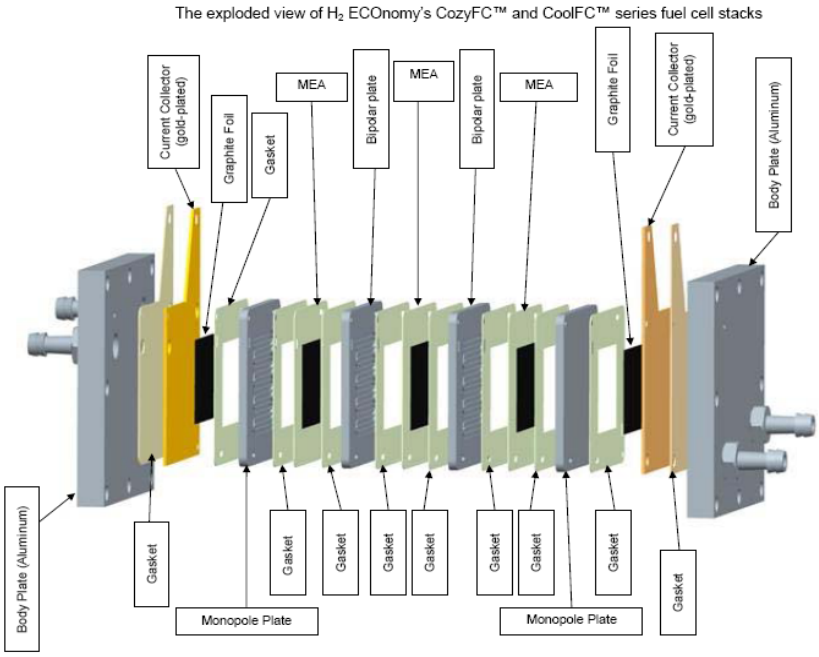

Figure 18: Schematic of the polymer electrolyte fuel cell stack.

Multi-Cell Performance

A 10-cell 48.5 cm^2 active area hydrogen-air polymer electrolyte fuel cell stack was purchased from H_2 ECOnomy (Yerevan, Armenia). A diagram of the stack is shown in Fig. 18. Conventional materials were used in the stack, as shown in Table 1.

Table 1: Specifications for the H_2 ECOnomy polymer electrolyte fuel cell stack

Stack Component	Materials
Membrane-electrode assembly	Membrane: N115 Catalyst: 30% Pt on Vulcan XC-72 Loading: 0.5 mg Pt/cm^2 Anode 0.5 mg Pt/cm² Cathode
Gas Diffusion Layer (GDL)	Carbon cloth
Bipolar, Monopolar, and Cooling plates	Polymer-Graphite composite
Active area (Electrode/Flow field size)	48.5 cm^2 (approx 7 x 7 cm)
Total area (Membrane/Plate size)	Approx 100cm^2 (10 x 10 cm)
Gaskets	Sheet Silicone
Current collectors	Gold-plated copper
Body plates	Polished aluminum
Fittings	Stainless steel, barb type

The stack is rated to deliver 100 Watts peak power at 4V and at 60°C when running on hydrogen and oxygen. Heating of the stack is achieved through resistive losses in the cell reactions. Cooling of the stack is achieved through external cooling (e.g., a fan) and is facilitated by ten cooling channels drilled through the center two bipolar plates. To enable monitoring of the individual cell performances and conditions, we incorporated voltage and thermocouple leads into each bipolar plate and a thermocouple into one of the cooling channels. The cells have been numbered consecutively from closest to the stack gas inlets to closest to the stack gas outlets.

This task was initiated at Argonne National Laboratory and relatively brief durability studies were performed at Argonne. The majority of this report focuses on the results of the testing at Northern Illinois University.

The stack performance was first measured under conditions identical to those recommended by H2 ECOnomy in order to verify correct operation of the stack. As recommended by the vendor, the stack was pre-humidified while at room temperature with 100ml/m nitrogen humidified at 30°C. The vendor recommended that the stack be brought to operating temperature by cycling the potential between open circuits and decreasing voltages. The temperature of the stack was monitored in the innermost air cooling hole. It was found that the stack did not warm up to 50°C in a practical amount of time and the constant cycling of the stack could cause damage before the initial tests were performed. Therefore, the stack was heated to the operating temperature of 65°C by holding at a constant potential of 7.0 V. At this time, the initial performance of the stack was measured using the following conditions: stack temperature of 65°C, hydrogen input and humidifier temperature of 50°C, oxygen input and humidifier temperature of 55°C, hydrogen flow rate of 1.24 SLPM, oxygen flow rate of 1.18 SLPM, oxygen pressure of 0.9 bar, and hydrogen pressure of 0.75 bar.

Following this initial test of the stack performance under conditions specified by the vendor, all future experiments were performed with gas flows set at constant stoichiometric ratios of 1.05 and 2.0 for hydrogen and oxygen, respectively. Constant stoichiometry reactant flows more closely resemble the actual operation of the fuel cell stack in the automotive application.

Durability Test Protocol

The U.S. Department of Energy has established a recommended procedure for testing the long-term durability of polymer electrolyte membrane fuel cell stacks and single cells [101]. As a quantitative measure, they defined stack durability as the time it takes for the average cell voltage to decay by 10% from the initial voltage when tested according to the procedures described below. Degradation is to be measured against the initial polarization curve. This durability protocol involves stepping through a series of different current draws typical of automotive loads. The guidelines for this protocol specify that an initial polarization curve is used to establish current densities at which average cell voltages of 0.88, 0.80, 0.75, 0.65, and 0.6 V are obtained. These current densities are designated C_{88}, C_{80}, C_{75}, C_{65}, and C_{60}, respectively. The stack is then subjected to the current density profile shown in Table 2.

Table 2: Current density vs. time for the cycle profile shown in Figure 19.

Step	Duration (sec)	C_{XX}	Step	Duration (sec)	C_{XX}
1	15	OCV	9	20	C_{75}
2	25	C_{80}	10	15	C_{88}
3	20	C_{75}	11	35	C_{80}
4	15	C_{88}	12	20	C_{60}
5	24	C_{80}	13	35	C_{65}
6	20	C_{75}	14	8	C_{88}
7	15	C_{88}	15	35	C_{75}
8	25	C_{80}	16	40	C_{88}

The stack load cycle used in our durability tests, Fig. 19, was established based on the initial stack polarization curve.

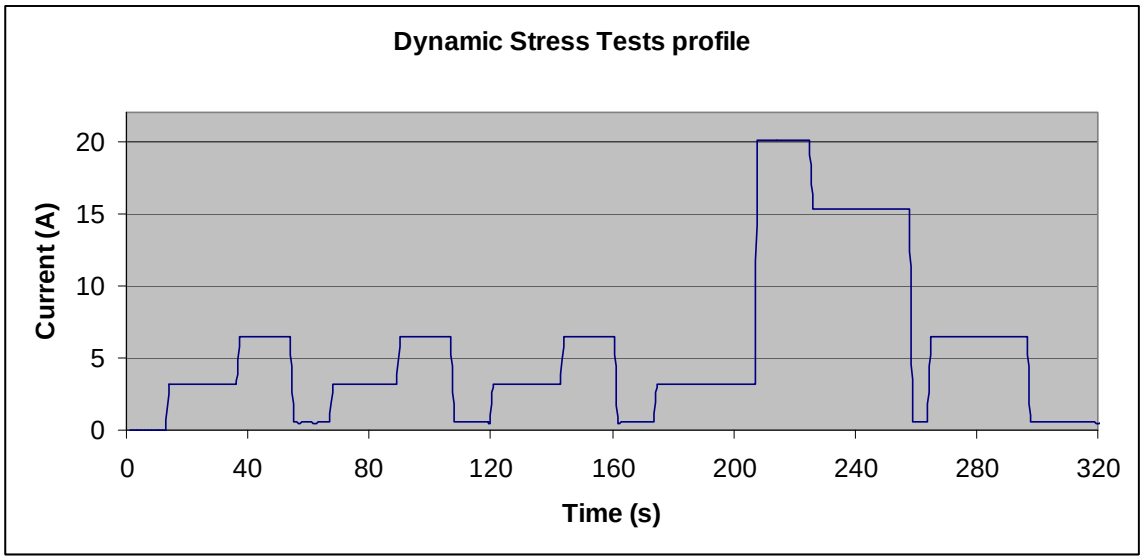

Figure 19: Load profile for the stack dynamic stress test.

In-Situ Diagnostics

During acquisition of the stack polarization curves a diagnostic procedure termed "current interrupt" was employed to determine the resistive losses due to the polymer electrolyte membranes, the bipolar plates, the gas diffusion layers, and to the contact resistance between the various stack components. The electrochemically-active surface area of the cathode platinum nanoparticle electrocatalyst and the hydrogen diffusion rate through the membrane were determined periodically using the procedures described in the appendix. Effluent from both the anode and cathode gas lines was collected periodically and analyzed for Pt content using inductively-coupled plasma-mass spectrometry (ICP-MS) with a Pt detection limit of 1 ppt.

Post-Mortem Diagnostics

Following the end of these experiments, the stack was disassembled and the membrane-electrode assemblies and gaskets were visually examined for signs of degradation. In addition, three MEAs (1, 5, and 7) were examined using scanning electron microscopy (SEM) and energy dispersive spectroscopy (EDS) elemental mapping. Approximately 1 cm^2 pieces of each MEA were cut out of the center of each cell. These pieces were then encased in epoxy (Epothin®, Buehler) such that a cross-section of the MEA was revealed. These epoxy-mounted samples were then polished flat using a vibratory polisher with kerosene as the carrier for the alumina polishing powder. The cathode and anode catalyst layers were removed from MEA 4 by swelling the MEA in isopropyl alcohol. X-ray diffraction analysis of these electrode layers was then performed to determine the mean size of the Pt nanoparticles through Debye-Scherrer analysis of the width of the (111) diffraction peak.

Power Conditioning

To determine the energy storage requirements for the fuel cell vehicle several methods were considered. Initially the energy storage requirements were considered based on just acceleration requirements. Later studies included a complete driving cycle.

Acceleration Study

Vehicle acceleration is one good method for determining fuel cell use. The maximum power demands generally occur during the acceleration so therefore the maximum system needs can be determined. Generally studies done for determine vehicle energy requirements assume a constant power demand throughout the acceleration. This is not very accurate as the power demand would need to change as the vehicle increases in speed. More typically the diver would command the desired force for the vehicle. Therefore, a constant force profile would be more useful in determining the power requirements. This first study compared the effect of a constant force to constant power acceleration in determining the energy storage needs.

The energy storage requirements for the vehicle are considerably different for the constant power and constant force operation. An example of this is shown in Figure 20. For constant power the auxiliary ESUs (batteries and supercapacitors) need to supply a large amount of power very quickly. For constant force, the power requirement builds up with speed so the auxiliary ESUs do not need to supply instantaneous power.

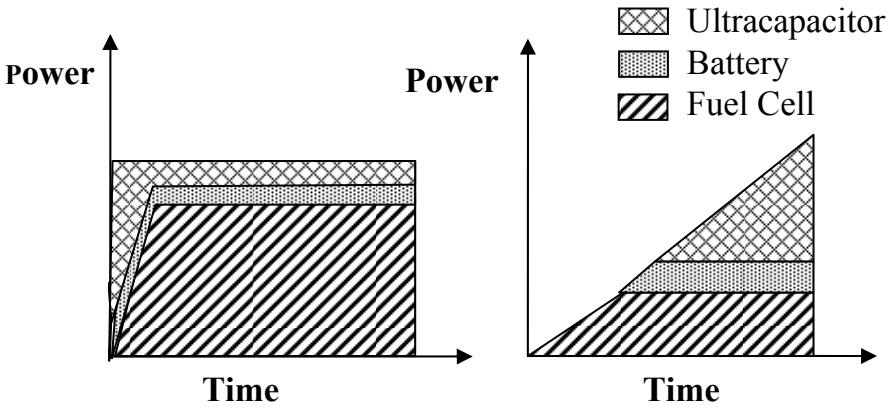

(a) Constant power profile (b) Constant force profile

Figure 20: Comparison of power requirements based on constant power and constant force acceleration.

The acceleration needs can be determined simply by using Newton's law. Basically, the acceleration can be determined as the difference between the applied tractive force (F_{TR}) and the other forces acting to oppose motion (F_O),

$$m\frac{dv}{dt} = F_{TR} - \sum F_O \,. \qquad (1)$$

For constant force acceleration this equation assumes the form

$$m\frac{dv}{dt} = K_1 - K_2 v^2 \,. \qquad (2)$$

Where, K_1 and K_2 are constants that depend on tractive force as well as drag and frictional forces acting on the vehicle [102]. This equation can be solved directly to find the velocity. Once the velocity is known, the power and energy requirements can be found.

For constant power the acceleration equation get modified to the form

$$v\frac{dv}{dt} = \frac{P_{TR} - v\sum F_O}{m} \quad . \tag{3}$$

In this form the velocity cannot be solved directly but solutions can be found using numerical techniques. Again power and energy can be determined once the velocity is known.

Once the total energy and power requirements are found the total storage capacity for each of the storage units can be determined. In this case the acceleration is used to determine the auxiliary ESUs, but the base power is considered to be supplied by the fuel cell. The battery and supercapacitor needs to supply the peak power used during acceleration and the store additional energy required for acceleration. The specific energy and power of the batteries and supercapacitors can be used to find the actual size of these components. The equations used to determine these components are:

$$P_{max} = \rho_B \cdot m_B + \rho_C \cdot m_C \tag{4}$$

$$W_A = \sigma_B \cdot m_B + \sigma_C \cdot m_C \tag{5}$$

Where, P_{max} is the peak power to be supplied by the combined batteries and supercapacitors; W_A is the additional energy storage needed for acceleration; m_B and m_C are masses of the batteries and supercapacitors respectively; ρ_B and ρ_C are the specific powers of batteries and supercapacitors respectively; σ_B and σ_C are the specific energies of the batteries and supercapacitors, respectively. Thus a system of two equations and two unknowns is established. It is therefore straightforward to solve for the required masses of the respective components.

Driving cycle study

Although periods of fast acceleration determine the largest demand on the power system, a study of an overall driving cycle might give a better understanding of ESU requirements. For this condition the energy storage capacities of the fuel cell along with its power capabilities are considered variables to be determined. This assumes some plug-in capability so the batteries can have an initial charge.

Two methods were used to determine the energy storage requirements. Method 1 minimized an objective function consisting of a weighted combination of component mass, volume, and cost. This method constrained the system by requiring minimum total energy storage, peak power, and cruising power. Method 2 maximized an objective function consisting of a weighted combination of energy storage, peak power, and average power. For this method, the system was constrained to a maximum volume, mass, and cost. In both of these methods solutions are obtained using the linear programming Simplex algorithm [103, 104]. Also in both of the methods the variables being manipulated are the masses of the battery, capacitor, hydrogen, and fuel cell.

For method 1 the constraint equations are

$$W_T = \sigma_B \cdot m_B + \sigma_H \cdot m_H \geq W_{min} \tag{6}$$

$$P_T = \rho_B \cdot m_B + \rho_C \cdot m_C + \rho_{fc} \cdot m_{fc} \geq P_{T\,min} \tag{7}$$

$$P_A = \rho_B \cdot m_B + \rho_{fc} \cdot m_{fc} \geq P_{A\,min} \tag{8}$$

where W_T is the total energy stored; W_{min} is minimum energy required for the driving cycle; P_T is the peak power capability; P_{Tmin} is the minimum peak power required to meet driving cycle demand; P_A is the average power capability; P_{Amin} is the minimum average power required to meet driving cycle demand; σ_H is the specific energy of the stored hydrogen; ρ_{fc} is the specific power of fuel cell; m_H is the mass of the stored hydrogen; m_{fc} is the mass of fuel cell.

The objective function for this method is given by

$$J = \alpha \cdot m_T + \beta \cdot V_T + \gamma \cdot C_T \tag{9}$$

Where m_T is the system total mass; V_T is the system total volume; C_T is the total monetary cost of the system.

The total system volume and cost can be put in terms of the mass as

$$V_T = \delta_B \cdot m_B + \delta_C \cdot m_C + \delta_H \cdot m_H + \delta_{fc} \cdot m_{fc} \tag{10}$$

$$C_T = \varepsilon_B \cdot m_B + \varepsilon_C \cdot m_C + \varepsilon_H \cdot m_H + \varepsilon_{fc} \cdot m_{fc} \tag{11}$$

Where
δ_B, δ_C, δ_H, δ_{fc} are the density of the battery, capacitor, hydrogen, and fuel cell respectively and
ε_B, ε_C, ε_H, ε_{fc} are the normalized cost of the battery, capacitor, hydrogen, and fuel cell respectively.

Thus the objective function can be written with only the masses of the various energy storage components as variables.

Determination of the masses of the various components is determined by minimizing the objective function while maintaining the constraints. The Simplex method of linear programming was used to obtain the final result. It should be noted that the Simplex method is generally applied to systems where the number of constraints is greater than or equal to the number of variables. Since in this method the number of variables is greater than constraints, one variable, the fuel cell mass, is set and the other variables are found based on that variable. A range of results for the different parameters are found for a range of fuel cell masses.

For method 2 the constraints are based on keeping the mass, cost, and volume less than a certain value. These constraint equations are

$$M_T = m_B + m_H \leq K_1 - m_{fc} \tag{12}$$

$$C_T = \varepsilon_B \cdot m_B + \varepsilon_C \cdot m_C + \varepsilon_H \cdot m_H \leq K_2 - \varepsilon_{fc} m_{fc} \tag{13}$$

$$V_T = \delta_B \cdot m_B + \delta_C \cdot m_C + \delta_H \cdot m_H \leq K_3 - \delta_{fc} \cdot m_{fc} \tag{14}$$

The objective function is based on the average power, peak power, and total energy. It is given as

$$J = \alpha \cdot P_A + \beta \cdot P_T + \gamma \cdot W_T \tag{15}$$

The objective function variables are defined in (6)-(8) above.

In this case the goal is to maximize the objective function based on the constraints given. Again the simplex method was used to find the values. As in method 1, the variables were determined in term of the fuel cell mass.

Power Flow Determination

Determining how to distribute power between the various ESUs is done in several steps. Based on a power demand calculation for a small time window, an optimization routine is used divide the power between the fuel cell and the other ESUs. Then a second optimization is used to determine the power flow from the batteries and supercapacitors.

Fuel Cell and Other ESU Optimization

In dividing the power between fuel cell and the other ESUs, the state of the battery is used as a control variable. The state of the battery is defined as the state of charge (SOC) times the maximum battery capacity. For this plant, the state of the battery (x_k) is given by

$$x_{k+1} = x_k + \left(\eta_k u_k - \varphi_k\right) Eff \tag{16}$$

Where x_k is the state of the battery, SOC*maximum capacity and η_k is the efficiency of the bi-directional converter from fuel cell side to power bus side. The efficiency can be either time varying or a constant. φ_k is a series of power requests depending on the driving cycle. It usually takes about 1 to 2 seconds for a fuel cell to respond to a power request. Thus, the state changing of battery and fuel cell is actually 1 or 2 seconds later than the load power request. So the φ_k here is actually the power request at an earlier time. u_k is the fuel cell output power to the power bus.

Eff is the battery charging/discharging efficiency, which is basically a nonlinear function with battery SOC, charging/discharging power.

The performance index to be minimized here for the control system is:

$$J_k = \frac{1}{2} P_k \left[x_N - 0.8C\right]^2 + \frac{1}{2} \sum_{k=i}^{N-1} \left[Q_k \left(x_k - 0.6C\right)^2 + R_k * u_k{}^2 \right] \tag{17}$$

Here J_k is the total cost function to be minimized. P_k, Q_k, R_k are weighting variables and C is the maximum capacity. x_N is the final battery state after N sampling points and x_k is an intermediate point between 0 to T.

The first term in (17) ($\frac{1}{2} P_k \left[x_N - 0.8C\right]^2$) represents the importance of having the final state for the window period achieve a charge of 0.8C. If the weighting, P, is chosen to be very high, then the final state x_N, need to be very close to 0.8C.

The second term of (17), ($\frac{1}{2} \sum_{k=i}^{N-1} Q_k \left(x_k - 0.6C\right)^2$), represents the charge variation in a given window period at a capacity of 0.6C. As it is desired to keep the battery charge within 40% to

80% of its maximum capacity, a state of 0.6C would maintain the charge at the median of these values.

And the third term of (17), ($\frac{1}{2}\sum_{k=i}^{N-1} R_k * u_k{}^2$), represents the importance of the fuel cell output power magnitude. If R is very large, then it is more important to limit the fuel cell output power.

In summary, first, the system dynamics are given by the physics of the problem (16), while the performance index (17) is chosen to achieve the desired system response. Second, to achieve different control objectives, appropriate weighting factors are chosen in the objective function J. Finally, sequences of control inputs are determined to minimize the objective function **J** [105].

To solve this problem, begin with the Hamiltonian function

$$H^k = \frac{1}{2}\left[Q_k \left(x_k - 0.6C \right)^2 + R_k * u_k{}^2 \right] + \lambda_{k+1}\left[x_k + \left(\eta_k u_k - \varphi_k \right) Eff \right] \tag{18}$$

which yields the state and co-state equations

$$x_{k+1} = \frac{\partial H^k}{\partial \lambda_{k+1}} = x_k + \left(\eta_k u_k - \varphi_k \right) Eff \tag{19}$$

$$\lambda_k = \frac{\partial H^k}{\partial x_k} = Q_k x_k - 0.6C * Q_k + \lambda_{k+1} \tag{20}$$

and the stationarity condition

$$0 = \frac{\partial H^k}{\partial u_k} = R_k * u_k + \eta_k * Eff * \lambda_{k+1} \tag{21}$$

Solving (21) for u_k gives

$$u_k = \frac{-\eta_k * Eff * \lambda_{k+1}}{R_k} \tag{22}$$

Using (22) to eliminate u_k in (19) gives

$$x_{k+1} = x_k - \left(\frac{\eta_k{}^2 * Eff * \lambda_{k+1}}{R_k} + \varphi_k \right) Eff \tag{23}$$

Given an initial condition, x_1, and the desired final state, x_N, the intermediate states, x_N, is determined to minimize the cost function. Hence $dx_N \neq 0$, according to boundary conditions, then it is required that

$$\lambda_N = \frac{\partial \phi}{\partial x_N} \tag{24}$$

The final state weighting function is $\phi = \frac{1}{2} P_N (x_N - 0.8C)^2$, so that

$$\lambda_N = P_N \left(x_N - 0.8C \right). \tag{25}$$

Equations (20) and (23) are rewritten in a state equation form

$$\begin{bmatrix} x_{k+1} \\ \lambda_k \end{bmatrix} = \begin{bmatrix} 1 & -\eta_k^{\,2} * Eff / R_k \\ Q_k & 1 \end{bmatrix} \begin{bmatrix} x_k \\ \lambda_{k+1} \end{bmatrix} + \begin{bmatrix} -\varphi_k * Eff \\ -0.6CQ_k \end{bmatrix} \tag{26}$$

It can be assumed that the co-state, λ_k, is composed of two auxiliary control series, which can be written as

$$\lambda_k = S_k x_k - v_k \tag{27}$$

where S_k and v_k are both unknown sequences. This is a valid assumption if a continuous relationship is found.

The relationship for λ_k from (27) can be substituted into (26). After simplifying the equation becomes

$$x_{k+1} = x_k - \left(\eta_k^{\,2} * Eff * S_{k+1} / R_k \right) x_{k+1} + \eta_k^{\,2} * Eff * v_{k+1} / R_k - \varphi_k * Eff \tag{28}$$

The co-state equation (20) is rewritten as

$$\lambda_k = \frac{\partial H^k}{\partial x_k} = Q_k x_k - 0.6C * Q_k + \lambda_{k+1} \tag{29}$$

Putting (27) into (29) gives

$$S_k x_k - v_k = \left[x_k - 0.6C \right] * Q_k + S_{k+1} * x_{k+1} - v_{k+1} \tag{30}$$

Combining (13) and (30) and simplifying gives

$$\left[Q_k + S_{k+1} * \frac{1}{1 + \eta_k^{\,2} * Eff * S_{k+1} / R_k} - S_k \right] * x_k + \left[-0.6C * Q_k + S_{k+1} * \frac{\eta_k^{\,2} * Eff * v_{k+1} / R_k - \varphi_k * Eff}{1 + \eta_k^{\,2} * Eff * S_{k+1} / R_k} - v_{k+1} + v_k \right] = 0 \tag{31}$$

Since this equation holds for all x_k, the bracketed terms turn out to be zero. Independently setting these terms to zero yields

$$S_k = Q_k + S_{k+1} * \frac{1}{1 + \eta_k^{\,2} * Eff * S_{k+1} / R_k} \tag{32}$$

$$v_k = 0.6C * Q_k - S_{k+1} * \frac{\eta_k^{\,2} * Eff * v_{k+1} / R_k - \varphi_k * Eff}{1 + \eta_k^{\,2} * Eff * S_{k+1} / R_k} + v_{k+1} \tag{33}$$

The boundary conditions for (32) and (33) are by comparing similar terms in (25) and (27). The resultant boundary conditions are

$$\begin{aligned} S_N &= P_N \\ v_N &= 0.8C * P_N \end{aligned} . \tag{34}$$

Combining (16), (22) and (27) gives

$$u_k = \frac{-\eta_k * Eff * (S_{k+1}\left[x_k + (\eta_k u_k - \varphi_k) * Eff \right] - v_{k+1})}{R_k} . \tag{35}$$

A feedback gain sequence is defined as

$$K_k = \frac{\eta_k * S_{k+1} * Eff}{\eta_k{}^2 * Eff^2 * S_{k+1} + R_k} . \tag{36}$$

Similarly a feed-forward gain is defined as

$$K_k^v = \frac{\eta_k * Eff}{\eta_k{}^2 * Eff^2 * S_{k+1} + R_k} . \tag{37}$$

Using these gains, the control sequence over the given time window is

$$u_k = -K_k x_k + K_k^v v_{k+1} + \frac{\eta_k * S_{k+1} * \varphi_k * Eff^2}{R_k + \eta_k{}^2 * S_{k+1} * Eff^2} . \tag{38}$$

The resultant system based on this control sequence is

$$X_{k+1} = (1 - \eta_k * K_k * Eff) x_k + \eta_k * Eff * K_k^v v_{k+1} - \frac{\varphi_k * R_k * Eff}{R_k + \eta_k{}^2 * S_{k+1} * Eff^2} \tag{39}$$

For urban or highway driving, it is expected that different control variables “R”, “Q” should be used for optimization, however, the variable “P” is only related to battery final state. Since this vehicle is considered to be a plug-in hybrid, “P” is not important. Therefore it can be set at a constant “1”. “R” and “Q”, on the other hand, affect vehicle behavior so much that they have to be considered inversely proportional to each other. Furthermore, to generate the feedback and feed-forward control gain sequence, it seems that the future driving situation should be known first. As this is impossible, the driving cycle is used to cut into short time window. For each window, the control variables are updated. It becomes apparent that the optimum length of the averaging window may change based on the driving cycle. Practically speaking, since highway driving usually has more rapid changes in power, its window length can be used in both urban and highway driving. When the vehicle is starting, the battery will charge the fuel cell auxiliaries and provide traction power for a period of the window length. Thus at startup, the controller will have a previously determined R and Q is first used and follow a previously nerated control sequence. During this first window, R and Q are updated for the next window.

Since the speed of a vehicle is always low at startup, the weights are initially updated using the urban driving. If the vehicle is accelerating and needs more power than urban driving, the battery SOC will fall lower than assumed. To keep the SOC in the proper range, the weighting

coefficients must be re-adjusted until SOC goes up again. If SOC is higher than expected, the coefficients are again adjusted to limit the fuel cell output power. In this way, the controller coefficients are updated just by observing the battery SOC.

For every window length, R and Q are updated using the following

$$\begin{aligned} \mathrm{R} &= \mathrm{R} \pm \left|\mathrm{SOC}_{\mathrm{ref}} - \mathrm{SOC}\right| * \mathrm{Gain} * \mathrm{R} \\ \mathrm{Q} &= 1/\mathrm{R} \end{aligned} \tag{40}$$

Where SOC_{ref} is the reference state of charge (0.6C) and SOC is the battery state of charge.

Battery and Capacitor Optimization

Using the above a power command sequence during the time widow is determined for the fuel cell. The difference between the power requested for the desired response and the power commanded from the fuel cell needs to be supplied from the batteries and capacitors. A separate optimal control is developed to split the power between these two elements.

The split between the battery and supercapacitor is described as

$$x_k \eta_c + y_k \eta_{bat} = \phi_k \tag{41}$$

Where,

x_k is the super-capacitor output power and y_k is the battery output power

η_{bat}, η_{cap} are the battery and super-capacitor's converter efficiency

ϕ_k is the power requirement over the whole sampling time.

This is the difference between the driving cycle load requirement and the fuel cell control input power given by

$$\phi_k = \varphi_k - u_k \tag{42}$$

Where, φ_k is the load condition.

When ϕ_k is positive, the energy storage system is discharged, and when ϕ_k is negative, the battery/supercapacitor are charged. Note that the power split control is valid for both acceleration and deceleration situations.

The cost equation that needs to be minimized is given as

$$J_k = \alpha \sum_{k=i}^{N-1} \left[\left(x_k - x_{\max} \right)^2 + \left(y_k - y_{\max} \right)^2 \right] + \beta \sum_{k=i}^{N-1} \left(x_k{}^2 \right) + \gamma \sum_{k=i}^{N-1} \left(y_k{}^2 \right) + \delta \sum_{k=i}^{N-1} \left(\phi_k / \eta - x_k - y_k \right)^2 \tag{43}$$

Where

$\alpha, \beta, \gamma, \delta$ are weighting variables,

x_k is the supercapacitor discharge power at instant k,

y_k is the battery discharge power at instant k,

$x_{\max}$ is the maximum supercapacitor discharge power, and

$y_{\max}$ is the maximum battery discharge power.

To extend the life of the supercapacitor is important to limit the power flow into or out of the device. This importance is reflected in the cost function with the term

$$\left(x_k - x_{\max}\right)^2 \tag{44}$$

Similarly, to protect the battery it is important to limit the flowing into or out of it. This importance is reflected in the cost function with the term

$$\left(y_k - y_{\max}\right)^2 \tag{45}$$

It is also desirable to limit the total energy used in the system. In the cost function his is reflected in the weighting terms

$$\beta\sum_{k=i}^{N-1}\left(x_k{}^2\right)+\gamma\sum_{k=i}^{N-1}\left(y_k{}^2\right) \tag{46}$$

It may be necessary to tolerate some difference between the requested power and the actual power delivered. The tolerance is reflected in the function by the term

$$\delta\sum_{k=i}^{N-1}\left(\phi_k/\eta - x_k - y_k\right)^2 \tag{47}$$

To make the objective function simple, it is assumed that converter efficiencies are the same. Then, y_k can be written in terms of x_k. With this assumption the cost function (43) becomes

$$J_k = \alpha\left[\left(x_k - x_{\max}\right)^2 + \left(\phi_k/\eta - \left(x_k + y_{\max}\right)\right)^2\right] + \beta x_k{}^2 + \gamma(\phi_k/\eta_k - x_k)^2 + \delta(\phi_k/\eta_k - x_k - y_k)^2 \tag{48}$$

Combining like terms while ignoring the subscript k for simplicity gives

$$\begin{aligned} J_k &= (2\alpha+\beta+\gamma+\delta)x^2 + (-2\alpha x_{\max} - 2\alpha\left(\phi/\eta\right) + 2\alpha y_{\max} - 2\gamma\left(\phi/\eta\right) + 2\delta y - 2\delta\left(\phi/\eta\right))x \\ &+\alpha x_{\max}{}^2 + \alpha\left(\phi/\eta\right)^2 - 2\alpha\left(\phi/\eta\right)y_{\max} + \alpha y_{\max}{}^2 + \gamma\left(\phi/\eta\right)^2 + \delta y^2 - 2\delta\left(\phi/\eta\right)y + \delta\left(\phi/\eta\right)^2 \end{aligned} \tag{49}$$

The local minimum of the cost function with respect to the battery power occurs at:

$$\begin{aligned} &(2\alpha+\beta+\gamma+\delta)x \\ &+(-\alpha x_{\max} - \alpha\left(\phi/\eta\right) + \alpha y_{\max} - \gamma\left(\phi/\eta\right) + \delta y - \delta\left(\phi/\eta\right)) = 0 \end{aligned} \tag{50}$$

Thus,

$$x = \frac{\alpha x_{\max} + \alpha\left(\phi/\eta\right) - \alpha y_{\max} + \gamma\left(\phi/\eta\right) - \delta y + \delta\left(\phi/\eta\right)}{(2\alpha+\beta+\gamma+\delta)} \tag{51}$$

Since

$$x = \phi/\eta - y$$

The power out of the battery becomes

$$y = \frac{(\alpha + \beta)(\phi / \eta) - \alpha x_{\max} + \alpha y_{\max}}{(2\alpha + \beta + \gamma)} \tag{52}$$

It should be kept in mind that the power in the supercapacitor and battery needs to be limited to reduce stress on those components.

This system has not taken into account the battery and supercapacitor capacity. Also the optimal control sequence cannot find a good choice of power split when the optimal result actually exceeds the limits of the input/output power. Therefore, a control logic considering all these effects needs to be found for the final implementation. The basic rules for the control logic are discussed in the following paragraphs.

Control Law Rules

As there are several auxiliary loads on the system, their power requirements must be continuously supplied by the ESUs. During startup the fuel takes some time for it to achieve rated power and would not be able to supply the auxiliary power. Therefore, this auxiliary load should be considered the minimum load for the battery.

Also because of the relatively long turn on time for the fuel cell, it is not very efficient to turn it off during periods of low power demand. Thus, when its power is not required for traction, it is at rest but still operating at a minimum power. The fuel cell is fully turned off only if the key is pulled out.

It could be possible that regenerative braking could be needed when both the battery and supercapacitor are almost fully charged. Thus, a power resistor is used to avoid over-charging those components. When either the battery's or supercapacitor's SOC is too low, they will be protected from giving out power. The limits used in this study are 40% for the battery and 25% for the capacitor. However, if traction power is not enough, they will still be used to supply power. When either the battery or the fuel cell has a SOC that is too high, they will be forced to deliver power but never absorb any. For battery, the limit is 80%; and for supercapacitor the limit is 100%. If both the battery and supercapacitor have states of charge that are too low, then they are both protected from discharging. Under this condition only the fuel cell gives power. The priority given to recharging them is determined by the difference between their individual SOC and their reference SOC along with the optimal control strategy.

If both SOCs are too high, then they are forbidden to take in any power. In this case any regenerative power needs to be dissipated in a power resistor. If the incoming power request is too large, then fuel cell would give more power than the optimal results would normally command. This would continue until the fuel cell power reaches its maximum sage limit.

Motor Control Method

In a vehicle, diver commands for acceleration and braking can be considered torque commands for the traction motor. Increasing the torque would cause the speed to increase. Likewise, decreasing the torque would cause the speed to decrease. At a constant cruising the driver would command a torque that would balance the opposing frictional forces. Thus the motor needs to be able to directly respond to these torque commands.

Because induction machine are rugged and highly reliable, they are often used in traction applications. An induction machine under load will run slightly below a synchronous speed set by the supply frequency. The difference between the synchronous speed and the motor speed is referred to as the slip speed of the machine. It is well known that the torque developed in an induction machine is directly proportional to the slip of the machine near synchronous speed. This relation can be used to develop a simple slip torque control for the machine.

Slip has been used as a method of torque control for many years [106]. It is not often used in precision torque control applications because it is only an approximate method. However, as the driver torque command is not very precise, it is felt that such a control would be acceptable in a traction application.

In an induction machine the slip frequency (ω_{sl})is given as

$$\omega_{sl} = \omega_e - \frac{P}{2}\omega_m \tag{53}$$

where , ω_e is the electrical synchronous frequency; ω_m is the mechanical speed and P is the number of magnetic poles in the machine.

Near synchronous speed, the electrical torque developed (T) is related to the slip

$$T = 3\frac{P}{2}\left(\frac{V}{\omega_e}\right)^2 \frac{1}{R_2}\omega_{sl} \tag{54}$$

where, R_2 is the rotor resistance.

From this equation it is quite clear that for a constant V/ω_e the torque would remain directly proportional to the slip frequency. As common electric motor drives operate in a constant V/ω_e mode, these standard converters can be used as part of the simple control scheme. A block diagram of the proposed control scheme is shown in Figure 21. This system is based around a digital controller. The controller reads the torque command and mechanical speed. The torque command is converter to a slip frequency and added to the mechanical speed to get the desired electrical speed. The controller then outputs the desired electrical frequency to the electric drive for the motor.

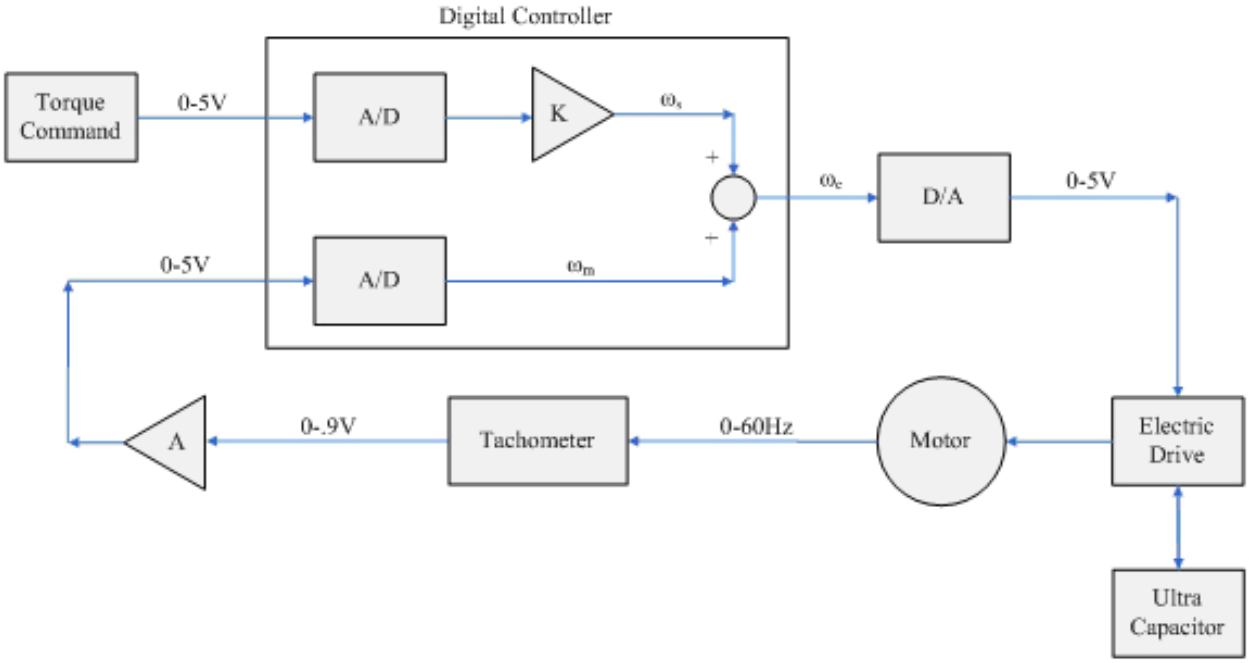

Figure 21: Torque Control System

Solid Oxide Fuel Cell Cathode

The synthesis method of novel solid oxide cathode materials was developed to produce new perovskite $La_{1-x}Sr_xMnO_3$ LSM ($x > 0.5$) compositions beyond normally achievable solubility limit at $x \sim 0.55$ in order to obtain oxygen vacancy ordered phases. This approach is based on yttrium stabilized ZrO_2 electrolyte.

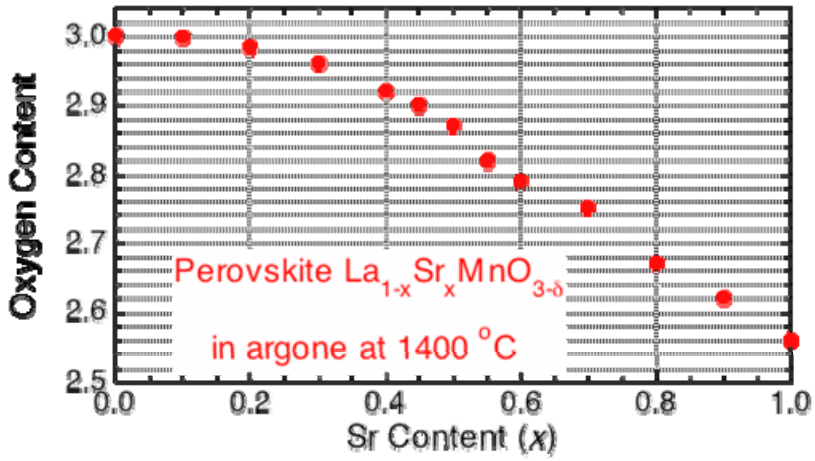

Figure 22: Oxygen contents of La1-xSrxMnO3-d perovskites produced in Ar.

The method consists of three steps. In the first step, highly oxygen deficient $La_{1-x}Sr_xMnO_{3-d}$ perovskites are produced in argon, Figure 22. The ionic sizes of La/Sr and reduced Mn^{3+x-2d} satisfy stability condition of tolerance factor $t \leq 1$ at the synthesis temperature ~ 1400°C. During

this step the uninteresting hexagonal structure exhibits high electronic and ionic conductivity and is converted to perovskite phase, Figure 23.

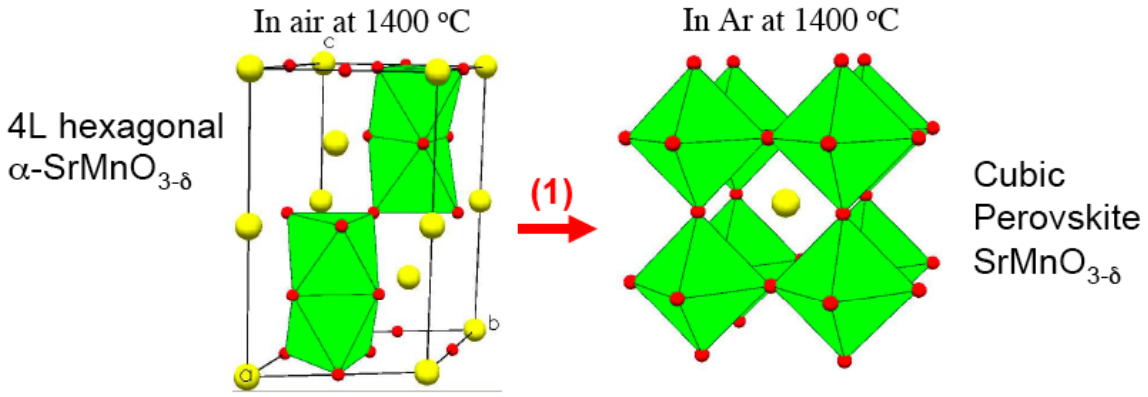

Figure 23: First step of the synthesis of kinetically stable perovskites.

During the second synthesis step the oxygen deficient $La_{1-x}Sr_xMnO_{3-d}$ perovskites are oxidized in oxygen or air at low temperatures, Figure 24. This results in materials suitable for further study of physical and structural properties. To obtain materials with well-developed oxygen vacancy ordered phases the final step of synthesis is performed in hydrogen, Figure 25.

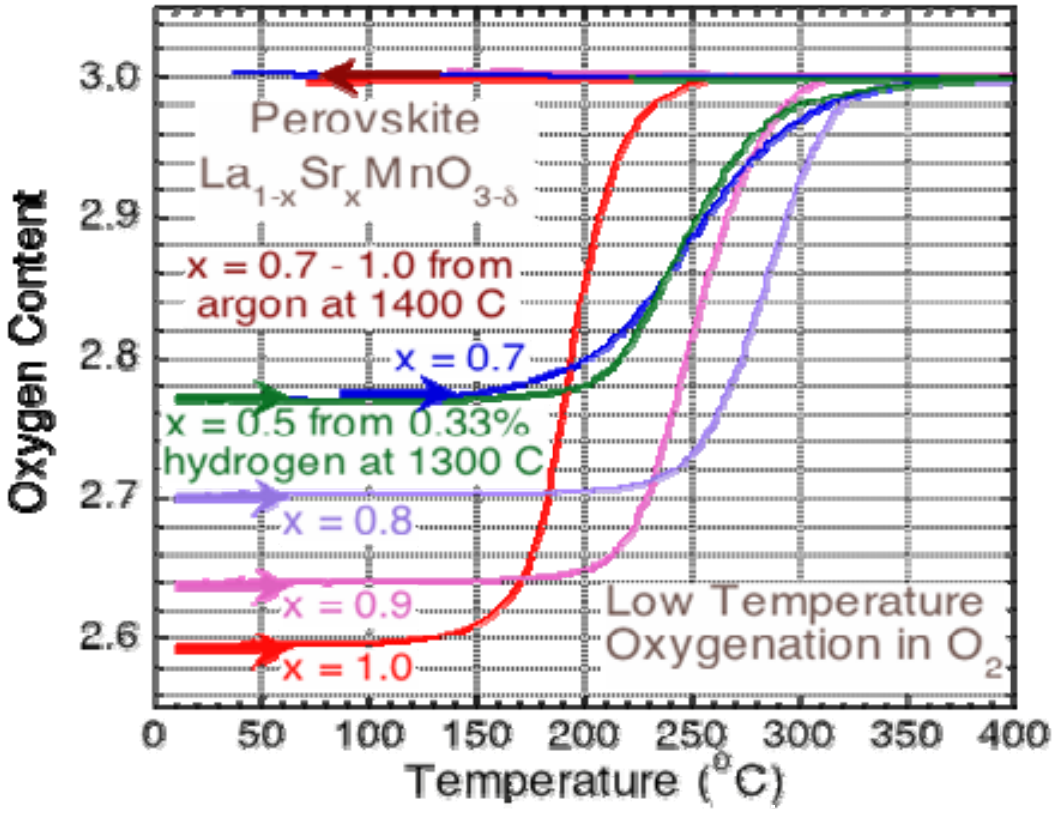

Figure 24: Low-temperature oxygenation of $La_{1-x}Sr_xMnO_{3-d}$ in oxygen.

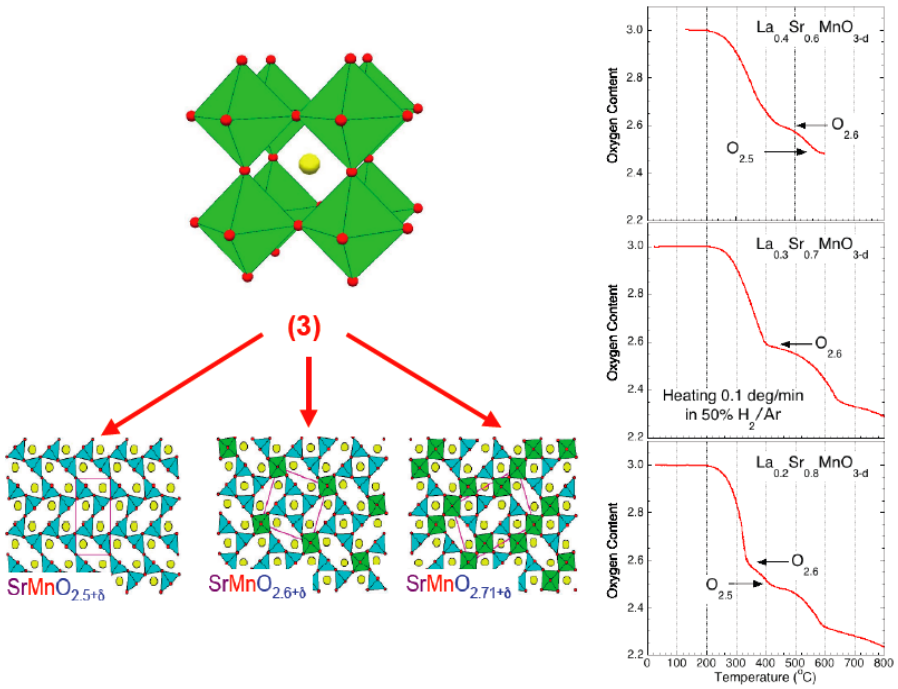

Figure 25: Low-temperature reduction of $La_{1-x}Sr_xMnO_3$ in hydrogen.

Synthesis of Samples for Special Experiments

Large-size batches of LSM compounds have been produced by wet-chemistry and ceramic methods. Dense tubes and pellets were made for "in situ" neutron diffraction structural experiments, Figure 26, and ionic/electronic transport measurements.

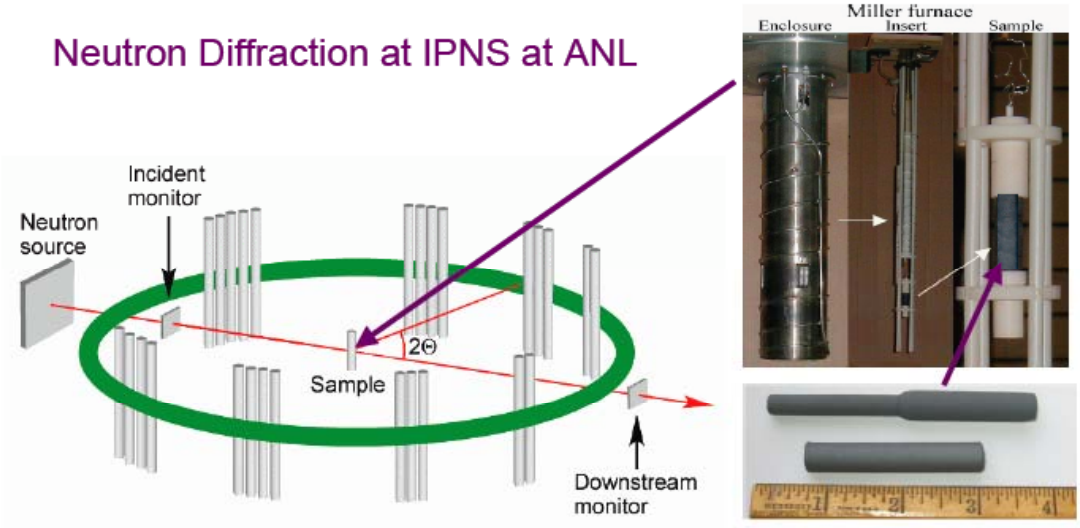

Figure 26: Schematic design of "in situ" neutron diffraction structural experiments performed on dense tubes using improved Miller furnace as a function of composition, temperature, and oxygen pressure.

Synthesis and Measurement of Mixed Conducting Cathodes

Similar synthesis techniques to that used for obtaining $La_{1-x}Sr_xMnO_{3-d}$ perovskites were used to produce the following materials: transition metal substituted $SrMnO_{3-d}$, $Sr(Fe,Mn,Co)O_{3-d}$, $(La,Sr)(Fe,Co)O_{3-d}$, $(La,Sr)CoO_{3-d}$, and $La(Fe,Ni)O_{3-d}$. Large-size batches of SFMC and LSFC compounds have been produced by wet-chemistry and ceramic methods from which dense tubes and pellets were made for "in situ" neutron diffraction structural experiments and ionic/electronic transport measurements. All these compounds are stable in O_2 and argon to at least 1100^oC.

Chapter 3 Results and Discussion

Chapter 3 Results and Discussion 45
Thin-Film of Ultralow Platinum Electrocatalyst by Chemical Electropolymerization 46
Tunable Platinum Phosphate Composite Thin-Film Electrocatalysts 48
Oxygen Reduction Ability by the Platinum Phosphate Matrix Catalyst 48
Catalyst at Potential Higher Than 1.0 V 51
Oxygen Reduction Efficiency 53
Minimization of Hydrogen Adsorption Property 54
Oxygen Reduction Efficiency of Mixed Metal Phosphate Composite Catalyst 55
Methanol Oxidation 56
Novel Catalyst Support 57
Bipolar Plates 59
Testing and Performance Evaluation of Bipolar Plates 61
PEM Fuel Cell Simulation Results 62
Hydrogen Concentration Distribution in Tri-Layer PEMFC 63
Oxygen Concentration Distribution in Tri-layer PEMFC 64
Temperature Distribution in Tri-Layer PEMFC 66
Water Distribution in Tri-Layer PEMFC 67
Cell Performance 68
Effect of Bi-Polar Plate Design on Polarization Curve 69
Thermo-Mechanical Analysis of Fuel Cell with Bi-Polar Plate 71
Single Cell Performance Evaluation 72
Platinum Phosphate Blue Cathode Catalyst 72
Nafion® and Commercially Available Catalyst 73
Multi- Cell Durability and Degradation Mechanisms 79
Initial Performance 79
Post-mortem diagnostic results 91

Six topics discussed in this chapter include (1) thin-film of ultralow platinum electrocatalyst by chemical electropolymerization, (2) novel catalyst support, (3) bipolar plates, (4) testing and performance evaluation of bipolar plates, (5) single cell performance evaluation, (6) multi- cell durability and degradation mechanisms, (7) fuel cell vehicle transient power, and (8) cathode catalyst development for solid oxide fuel cell.

Thin-Film of Ultralow Platinum Electrocatalyst by Chemical Electropolymerization

Thin-films of ultralow platinum loading was created based on the adsorption and electrochemical properties of platinum phosphate blue (Figure 5). The platinum phosphate blue exhibited two successive quasi-reversible redox waves on a pure platinum working electrode corresponding to the electrode reactions:

$$Pt_4^{(II,II,II,III)} + e^- = Pt_4^{(II,II,II,II)} \quad (55)$$

$$Pt_4^{(II,II,II,II)} + 8e^- = 4Pt \quad (56)$$

The reduction potentials at pH 6.0 can be estimated as – 0.47 V and –0.68 V vs. Ag/AgCl electrode. On the other hand, the appearance of an almost featureless voltammogram with a shoulder at –0.95V, recorded in the first cycle using carbon as the working electrode, indicates that platinum phosphate blue is weakly electroactive on this carbon surface. The replacement of the shoulder by well defined reduction waves and dramatic increases of current in the next few successive cycles are indicative of the formation of a modified electrode on which the phosphate blue is easily reducible. Such an increase in current in subsequent cycles is a characteristic of an electropolymerization process [107-109]. This modified electrode functions in completely the same way as a platinum metal electrode as indicated by several independent chemical and electrochemical experiments described below. First, subsequent cycles revealed two well defined quasi-reversible redox couples as were observed on a pure platinum working electrode. After a few cycles, a shiny platinum layer was quite transparent on the carbon surface. Secondly, an analysis of platinum content on the carbon electrode by ICP revealed a cycle dependent platinum coating. By using 2.0 mM phosphate blue solution and a carbon rod of 3.18 mm diameter, this coating varied from 0.03 mg/cm^2 to 0.25 mg/cm^2. Thirdly, the voltammograms of $Fe(CN)_6^{2-/3-}$ redox couples exhibit identical features, both in peak positions and magnitude of current, when the equal electrode surface areas of a platinum metal electrode and platinum coated carbon electrode were utilized.

Some comment the mechanism of electrode deposition on the carbon surface deserves. First, the remarkable increase in current at and near the reduction potentials of the blue in the second cycle implies that a catalytic nucleation process must be involved. This is due the fact that uncatalyzed deposition of platinum would be accompanied by an equal or less gradual increase in current density compared to the first cycle. Since the platinum phosphate blue is an oligomeric species, it is likely that further polymerization of the oligomers by adsorption on the carbon surface might have led to this very efficient electrodeposition process. Furthermore, the adsorption process perhaps overcame the activation energy barrier for such polymerization and the potential applied during the voltammetry experiments.

Further evidence for the catalytic electrodeposition process can also be found by comparing the amount of platinum deposition onto the carbon surface by reduction of $PtCl_4^{2-}$ with that obtained from the platinum blue. By using identical concentrations of the platinum complexes, a much reduced coating of platinum on carbon surfaces was observed from the chloro-complex even when a more negative cut-off potential (-1.2 V vs. Ag/AgCl) was employed. In addition, the electrodeposition from the tetrachloro-complex appears to be gradual and linearly proportional to the number of scans.

The second interesting feature of the limiting current after a few cycles of voltammetry points to a unique characteristic of the electrode, e.g., monolayer formation. Once the carbon surface is covered with a monolayer, further deposition did not increase the effective surface area of the electrode and therefore no significant increase in current density was observed. Furthermore, after 15 to 20 cycles no significant changes in the platinum deposition were observed. This is due to the fact that pure platinum metal electrode revealed only redox waves and no deposition of platinum on to platinum surface was observed, as the carbon surface converted to a platinum surface, the completely coated electrode functioned just as the pure platinum surface does.

The current method of electro deposition needs to be compared with other electrochemical methods. In an excellent article, Litster and McLean [109] have recently reviewed the performance of PEM fuel cell electrodes including those prepared by electrochemical depositions. Reddy et al. [110,111] have described electrode deposition of platinum by utilizing pulse current methodology in chloroplatinic acid baths. This patented technology exhibited comparable performance of the fuel cell even with ten-fold reduced platinum loading. Verbrugge [109] has also utilized pulse current methodology in loading platinum; his methodology differed from Reddy's in its use of sulfuric acid, starting platinum substrate, and the application of a membrane (not nafion). In this method, currents of magnitude of a couple of amps were used in a 10 mM $Pt(NH_3)_4^{2+}$ solution. Verbrugge [109] commented that the voltage during this high pulse current application reached several volts. Certainly, this method requires ultrapure platinum solutions since almost all metals can be reduced on the surfaces due to the large change in voltage during the pulse current applications. As the concentrations of platinum decrease due to the progression of the coating process, larger potential change is required to maintain the constant pulse current. Other researchers have reduced platinum compounds by first adsorbing platinum cations on nafion membranes or carbon surfaces followed by electrochemical reduction by applying appropriate voltage [112-114].

Our method seems to be simple because the catalytic process accelerates the deposition of platinum with a relatively low cut-off voltage. Furthermore, since the catalytic activity of platinum depends on the structures and particle sizes [114, 115], our method may afford different structures with variable particle size than those obtained by the pulse current method. The reason for this is that in the pulse current technology, platinum is forced to deposit on the carbon surface by applying a large electromotive force and therefore there is no control over the surface structure. In our method, natural crystal growth may be accomplished due to catalytic nature of the growth process. Also, the deposition seems to be uniform and can be controlled at any level until saturation. Finally, the active surface area obtained from this method with ultra-low platinum coating is much larger than other electrodes either commercially available or reported in the literature [116].

This technology is currently being used in our laboratory to prepare membrane electrode assembly for both membrane exchange and phosphoric acid fuel cell. The structure and adsorption processes of the platinum substrate, platinum phosphate blue, might also be helpful in creating a structural lattice that may be responsible for the higher active surface area. It is interesting to note that Bouwman et al [117] recently reported that the electrocatalytic activity of oxygen reduction by platinum was enhanced in the presence of dispersed iron phosphate. It remains to be seen whether such enhancement was aided by the phosphate ligand or by the different oxidation states of platinum center.

Tunable Platinum Phosphate Composite Thin-Film Electrocatalysts

Platinum phosphate composite thin-films surfaces on carbon support are prepared from electropolymerization and reductive electropolymerization of platinum phosphate blue by cycling voltages between two predetermined values as described earlier. These thin-film electrocatalysts are capable of reducing oxygen and oxidizing methanol, and generating additional oxygen at the surface of the catalyst. The platinum surface is a tunable active catalyst with a variety of compositions that range from phosphate coordinated metal ions to pure metallic formed from mixed valence platinum precursors by an electropolymerization technique. The platinum surface can have various oxidation states such as 0, (II), or (III). For example, the platinum surface can have an oxidation state of (II) and (III) and be bound to phosphate. The platinum surface is thus truly "tunable" based on the use of the platinum surface, such as for a fuel cell catalyst. The platinum surface is tunable because it can be designed with the desired valence states with variable compositions. For example, the platinum surface can be 100% platinum(II,III)- phosphate polymer, or a mixture of platinum(II,III)- and platinum(III,III)-phosphate polymer, or a mixture of platinum(II,III)- , platinum(III,III)- phosphate polymer, and platinum metal. The relative composition for each one of the components can be manipulated based on the selection of the voltage range during the preparation of the catalyst. Additionally, other non-platinum metals can also be coordinated on to the platinum phosphate composite surface. Therefore, one should be able to design a specific catalyst based on the desired needs. For example, a mixture of platinum (II, III)-, platinum (III, III)-phosphate polymer and platinum metal is expected to perform better for oxygen reduction by providing both metallic and ionic surface protected by phosphate moiety. On the other hand, methanol oxidation can be performed by the ionic surface without exposing CO poisoning the metallic surface.

The unique properties are the combination of efficient oxygen reduction by engaging platinum (II) and platinum (III) oxidation states anchored to phosphate and methanol oxidation by minimizing carbon monoxide poisoning at the catalyst surface due to a reduced affinity to absorb carbon monoxide. Phosphate protects the catalyst from oxidation at higher voltages, in the range 1.0-1.5 V where conventional catalysts substantially lose their activity, for durable performance. Phosphate also acts as a ligand (or binder) for tightly anchoring the metal ions of the electrocatalyst to a substrate. The phosphate has proton conducting properties to blend with the substrate, especially an ionomer, and is a required electrolyte to shuttle protons from anode to cathode. All these novel and improved properties are demonstrated below with supportive experimental data.

Oxygen Reduction Ability by the Platinum Phosphate Matrix Catalyst

To demonstrate the properties of the platinum phosphate thin-films rotating disk electrode (RDE) voltammetry and steady-state voltammetry experiments were performed. Representative oxygen reduction properties are displayed in Figures 27- 31 on various carbon surfaces stated and their superior characteristics are elaborated below.

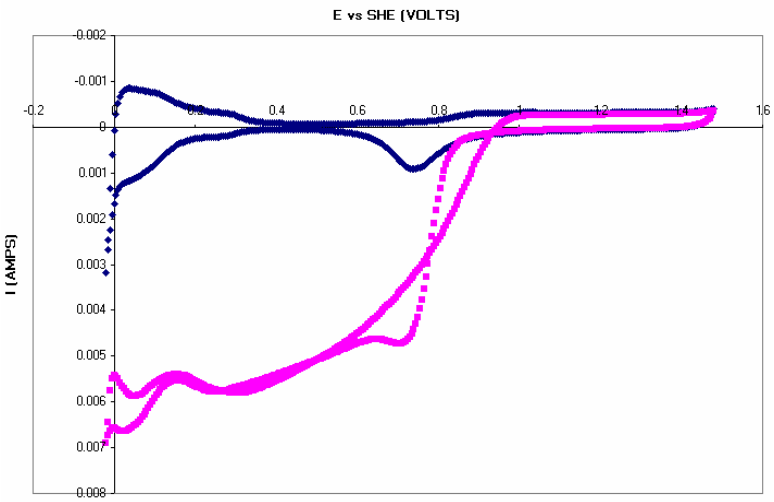

Figure27: A graph of current potential curves generated from the thin-film platinum phosphate catalyst on carbon paper (0.08 mg/cm2) utilizing a three-electrode cell by using a voltage scanning rate 25 mV/s. The total geometric surface area exposed was 1.12 cm2

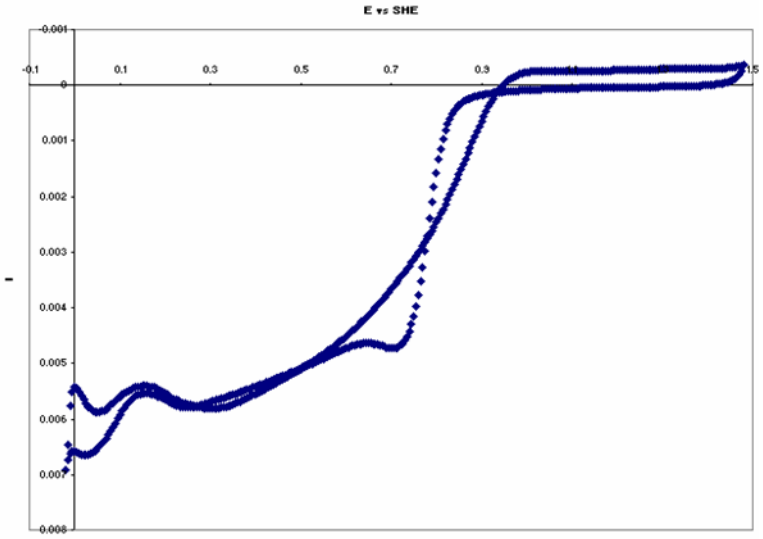

Figure28: A graph of net current (oxygen saturated minus argon saturated cells)-potential curve demonstrating the oxygen reduction and presence of additional current after the reduction peak presumably due to water oxidation properties of the thin-film catalyst as in Figure 27.

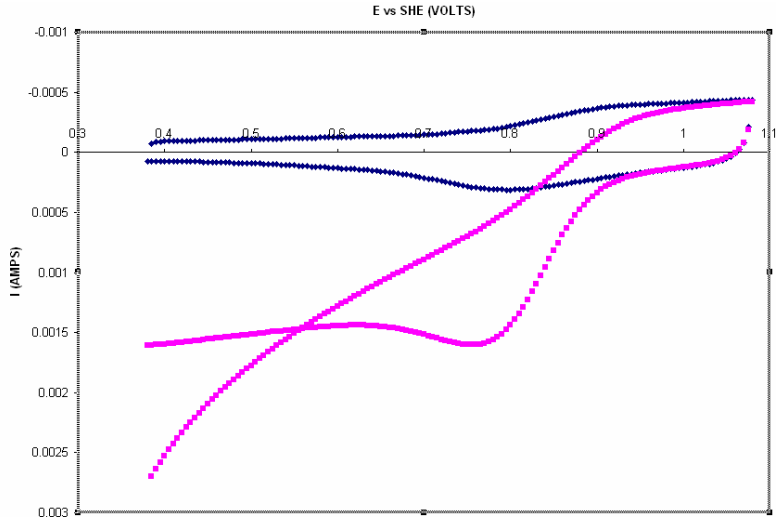

Figure 29: A cyclic voltammogram of oxygen reduction by a platinum phosphate composite catalyst on carbon cloth: the blue curve was recorded in argon while the red curve in the presence of oxygen. The voltage scan rate was 25 mV/s.

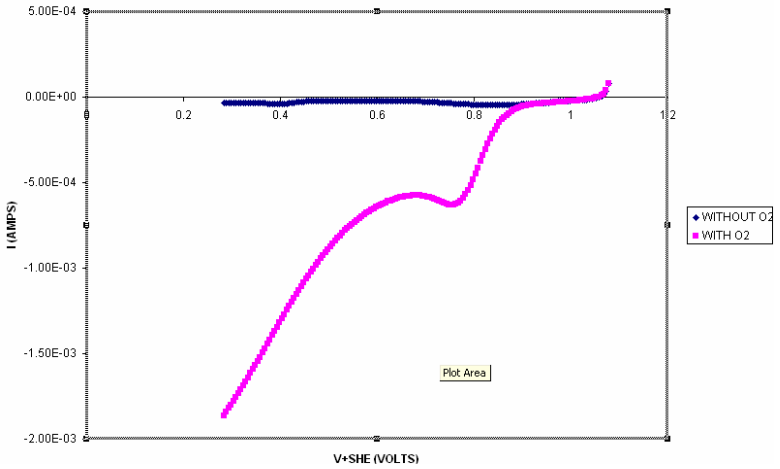

Figure 30: A cyclic voltammogram of oxygen reduction by a platinum phosphate composite catalyst on carbon rod: the black curve was recorded in argon while the red curve in the presence of oxygen. The voltage scan rate was 5 mV/s and geometric area was 0.713 cm^2. Similar features were observed for all scan rates from 10-100 mV/s expect that currents were higher for higher scan rates.

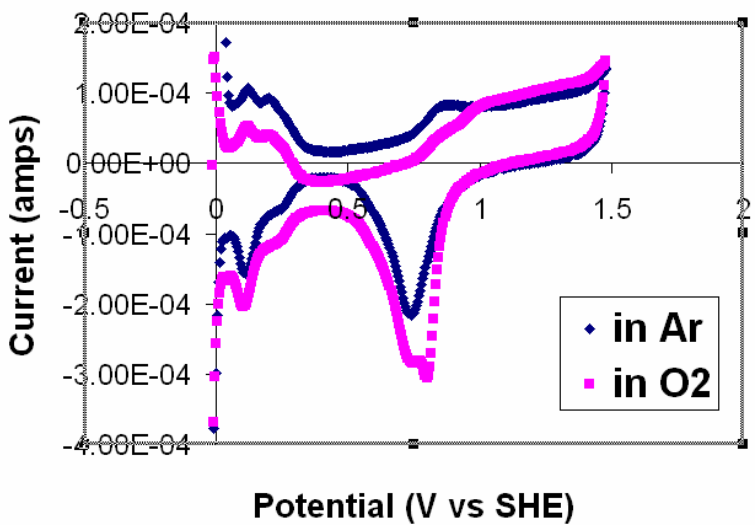

Figure 31: Cyclic voltammograms of an oxygen reduction reaction on commercial Pt-catalysts with comparable loadings as in Figure 27: the black curve was recorded in argon while the red curve in the presence of oxygen.

The blue plots were taken in the absence of oxygen (argon purged) and the red curve is in the presence of oxygen. Note that the current continues to grow beyond the peak potential at 0.75 V due to additional reduction of oxygen. These figures show that platinum phosphate thin-films are capable of reducing oxygen yielding much higher current densities than conventional catalysts.

Catalyst at Potential Higher Than 1.0 V

The superior properties of platinum phosphate composite catalyst is seen by comparing Figures 27 and 31. Figure 31 shows the current-potential curve in argon and oxygen purged solution for the commercial catalyst (0.1 mg/cm^2).

In Figure 31, blue and red curves were recorded in the presence of saturated argon and oxygen atmosphere. Note that the decline in current after the peak potentials (0.75 V) is quite substantial. In fact, at 0.4 V, the current almost approaches zero. The forward scan (positive potential to negative potential) in argon solution shows a peak at 0.8 V due to the reduction of platinum oxide. In the oxygen purged solution, the reduction current rapidly increases below 0.85 V and levels off below 0.8 V vs. SHE. This increase in current is due to the reduction of oxygen. Figure 27 shows the same experiments with the newly developed platinum phosphate composite catalysts.

As can be seen from Figure 27, there is small reduction peak of platinum oxide in argon which usually appears at about 0.8 V vs. SHE. The oxygen reduction is seen by the rapid rise of current below 0.8 V and leveling off at about 0.6 V. Note that the platinum content in this new platinum phosphate composite catalyst electrode is 0.08 mg_{pt}/cm^2, less than the commercial electrode in Figure 31, yet the net current is almost double that of the commercial catalyst.

As indicated earlier, conventional platinum catalyst forms oxide layer which is not an active catalyst for oxygen reduction and detrimental for fuel cell operation. This oxide formation is severe when the potential increases above 1.0 V due to the oxidation of platinum metal. Figures 32 and 33 show current-voltage curves recorded by RDE technique both for mixed-valence

platinum phosphate catalyst and one of the conventional platinum catalyst (platinum on carbon; 40% Pt by weight).

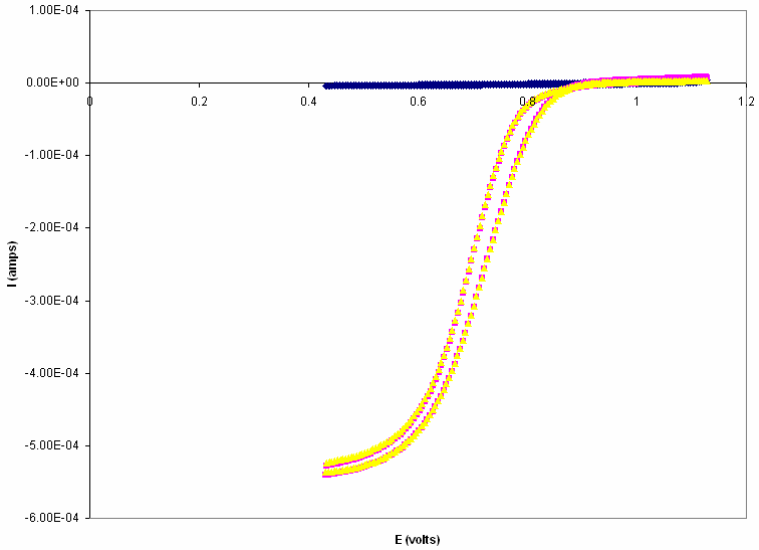

Figure 32: A graph of a rotating disk electrode voltammetry (900 rpm) of oxygen reduction by platinum phosphate composite catalyst (0.09 mg/cm^2; geometric surface area 0.196 cm^2): the blue curves are recorded in argon, red curves in oxygen, and the yellow curves are the net current due to oxygen reduction, and note that red and yellow curves overlapped due to the absence of platinum oxide layer.

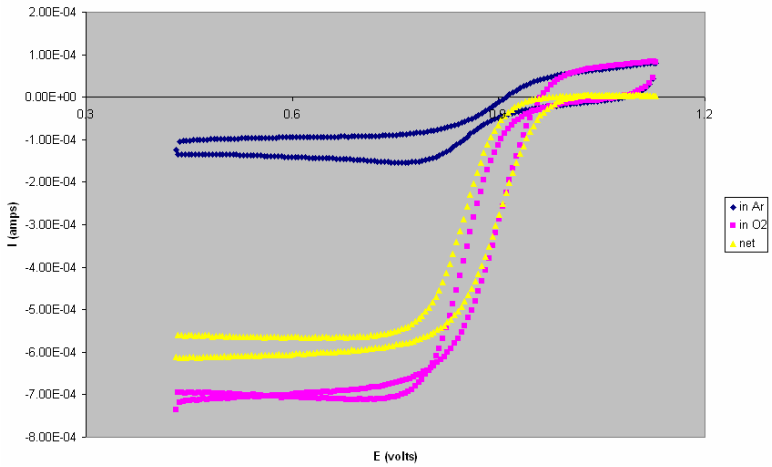

Figure 33: A graph of rotating disk voltammetry of oxygen reduction by a commercial catalyst (0.25 mg Pt/cm^2; geometric surface area 0.196 cm2) (Alfa Aesar, 40 wt% Pt/C) at 1600 rpm: the blue curves are recorded in argon, red curves in oxygen, and the yellow curves are the net current due to oxygen reduction.

In Figures 32 and 33, the blue line was taken in the presence of argon and red in oxygen. The yellow curve represents the net current due to oxygen reduction. Note that there is no significant current in argon purged due to the lack of formation of platinum oxide. Note that significant

oxidation of the commercial catalyst is observed above 1.0 V due to the presence of oxidation current (Figure 33) while such oxidation is virtually absent in the platinum phosphate catalyst (Figure 32). Also, note that platinum loading for the commercial catalyst is 2.5-fold higher than the new developed platinum phosphate composite catalyst. Lack of deactivation of the platinum phosphate composite catalyst is also seen in Figure 27 where the voltage was increased to 1.5 V. In contrast, tremendous oxidation of the commercial catalyst is observed (Figure 31) due to the presence of large oxidation current.

The experiments on mixed-valence platinum phosphate catalyst minimizes the formation of oxide and clearly show that the leveling current due to oxygen reduction in Figure 33 is not 2.5-times more than in Figure 32 as expected based on the amount of platinum catalyst loaded on to the electrode. The current density calculated at 700 mV for the mixed-valence catalyst appears to be at least three-times more than the commercial catalyst.

Oxygen Reduction Efficiency

Steady state voltammetry experiments were performed to demonstrate unusual oxygen reduction efficiency. Like RDE experiments, current-potential curves were recorded in argon and oxygen purged solutions both for the commercial and platinum phosphate composite catalyst. For the platinum phosphate catalyst, in the forward scan (starting 1.5 V and scanning toward 0.0 V) for oxygen saturated cells revealed a steady increase in current from potential 1.0 to 0.9. This followed a steep rise in current up to 0.74 V and then a small decrease followed by small but continuous increase rather than a decrease in current (Figure 27), red curve forward scan. In the reverse scan (starting at 0.0 V and moving toward 1.5 V), a continuous decrease in current until 0.9 V followed by a level-off of current in the region above 0.9 V was observed (Figure 27, red curve reverse scan). The current-voltage curves, recorded by forward and reverse scans, in argon purged solution are also displayed in Figure 27 (blue curves). The blue curves exhibit conventional features due to the formation and depletion of platinum oxide layer in the forward scan and reverse scans. However, this oxide layer is very small as revealed by the presence of small current at 0.8 V. The net current-voltage curves, obtained by subtracting currents in argon solution from oxygen saturated solution at every potential, is shown in Figure 28. In Figure 29, the scanning rate was 25 mV/s. The blue plot is taken in the absence of oxygen (argon purged) and the red curve is in the presence of oxygen. Note that the current levels off at 0.75 V and did not decline at voltages less than 0.75 V. When the experiments were conducted by using higher scan rates, similar leveling off features was observed.

The continuous increase followed by an almost leveling off of current (Figures 27 & 28) in the present invention is due to the continuous supply of oxygen at the electrode surface due the activation of mixed-valence composite catalyst and perhaps augmented by oxidation of water which remained abundant in the cell. The participation of the activated mixed valence platinum phosphate layer is verified based on the nature of current-voltage curve in the reverse scan, i.e., varying the potential from negative values to the positive value, 1.5 V. vs. SHE as shown in Figures 27 and 28. As can be seen from Figure 28, the current values in the reverse scan up to 0.9 V do not reflect any anodic current as commonly observed for all electrocatalysts reported to date, rather it displays almost equal reduction currents as was observed in the forward scan. This behavior is seen at all scan rates from 10 mV/s to 100 mV/s. These data imply that that several different catalysts are participating in oxygen reduction reaction and perhaps water is continuously oxidized at the thin-film surfaces to supply oxygen which is reduced to generate current.

To compare the performance of our activated catalysts, identical experiments were performed with 40% Pt/C (Alfa Asear) catalyst which is commonly used in commercially available fuel cells. In these experiments, platinum catalyst (Alfa Asear) ink was spread on a carbon surface with platinum loadings higher than those thin-films described in the previous section. Figure 31 shows a typical current-voltage response in the forward scan (going from positive to negative potentials). In the argon purged solution, a large reduction of oxide layer was observed. In the oxygen saturated solution, the current initially increases in the region 0.9 to 0.7 V due to oxygen reduction followed by sharp decrease in current due to the depletion of oxygen at the electrode surface. Note that two reduction peaks of almost equal current, one for the oxygen reduction and the other for the platinum-oxide reduction, were observed. These data imply that as much as 40% of the platinum surface was covered by the oxide which is not an oxygen reduction catalyst. In the reverse scan, the current rapidly decreases below the zero base-line.

Minimization of Hydrogen Adsorption Property

Hydrogen adsorption and desorption properties for two electrocatalysts prepared with two different compositions are shown in Figures 34 and 35. These experiments are conducted using a working electrode containing the electrocatalyst, a Pt-wire as an auxiliary electrode, and Hg/HgSO4 as the reference electrode.

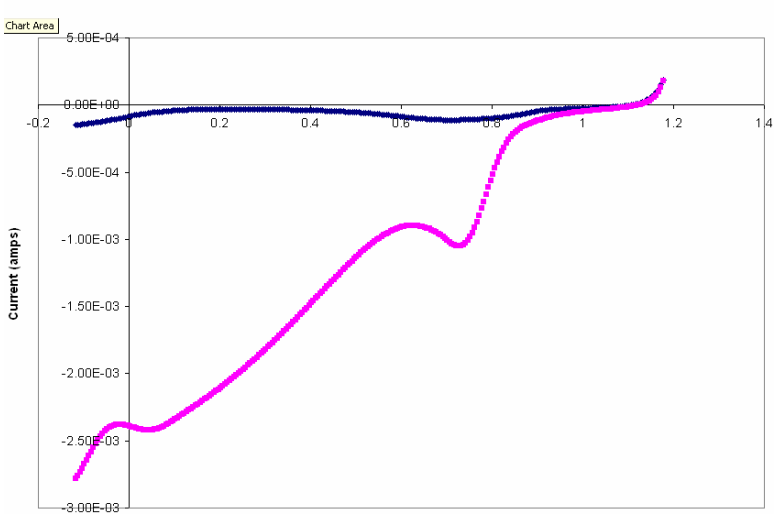

Figure 34: a graph of hydrogen adsorption/desorption behavior (blue curve) for a platinum phosphate composite with predominant mixed valence platinum (II,III) species. The voltage scan rate was 10 mV/s.

A solution of 0.5 M H_2SO_4 was used as an electrolyte and purged with ultrapure argon for 45 minutes. The potential was scan at a rate of 10 mV/s from positive to negative direction and currents were measured at different potential.

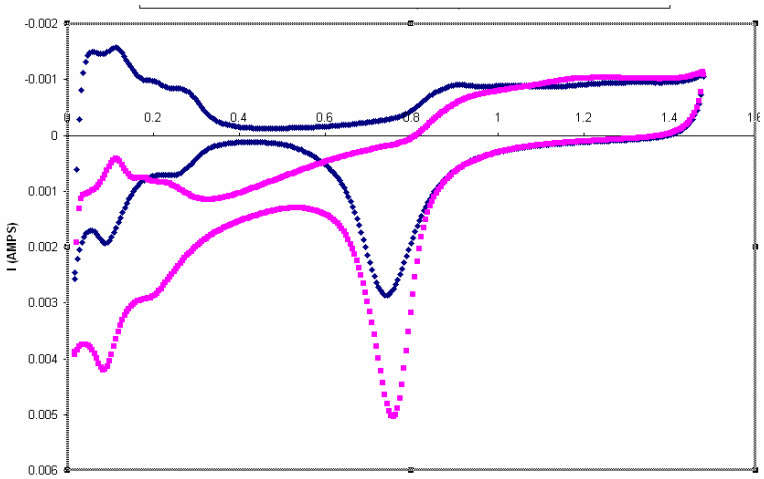

Figure 35: A graph of hydrogen adsorption behavior (black curve) for a platinum phosphate composite catalyst that contains 2/3 platinum metal and 1/3 mixed valence platinum (II,III) species. The voltage scan rate was 25 mV/s.

Figures 34 and 35 show the current-potential plots for two different electrocatalyst. Hydrogen adsorption on platinum surface is characterized by several adsorption desorption peaks in the voltage range 0.0 to 0.4 V. In Figure 35, the electrocatalyst clearly shows the hydrogen adsorption/ desorption features at 0.25 and 0.08 V in the reduction side and 0.18, 0.21, and 0.27 V on the oxidation side indicating substantial metallic character. In Figure 35, note that distinct hydrogen adsorption peaks are present due to the presence of metallic platinum in the composite. In Figure 34, those features are barely observed, indicating that the mechanism of catalysis is different than platinum metal catalysts. Note that hydrogen adsorption properties are strongly observed in commercial catalyst presented in Figure 31.

Oxygen Reduction Efficiency of Mixed Metal Phosphate Composite Catalyst

The oxygen reduction ability of the mixed metal phosphate composite was evaluated using mixed-metal phosphate composite loaded on a variety of carbon surfaces. Figure 36 shows the enhancement of oxygen reduction when mixed-valence platinum phosphate species is coated with ruthenium. Note that incorporating ruthenium does enhance oxygen reduction on platinum metal catalysts. Figure 37 shows the oxygen reduction ability of the iron coated platinum phosphate composite catalyst. Here again, some enhancement was also observed.

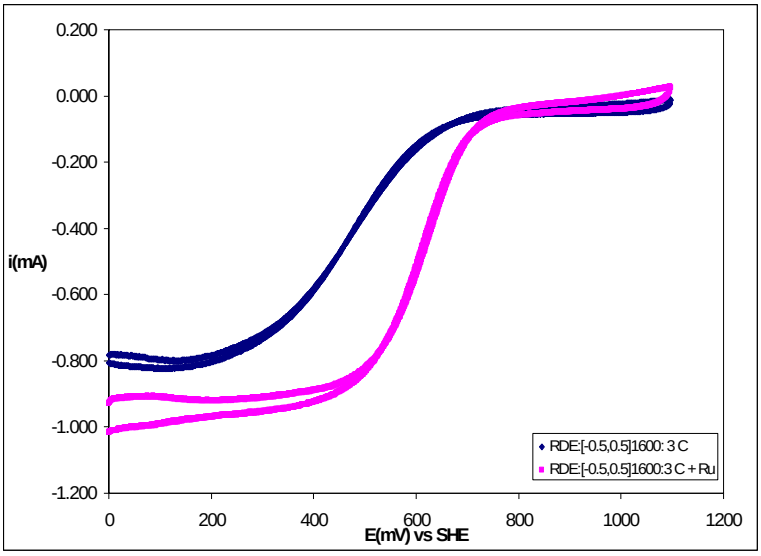

Figure 36: graph of rotating disk voltammetry (1600 rpm) of oxygen reduction by platinum phosphate composite catalyst composed of predominantly mixed-valence species (0.05 mg/cm^2) and augmented by ruthenium (<0.02 mg/cm^2).

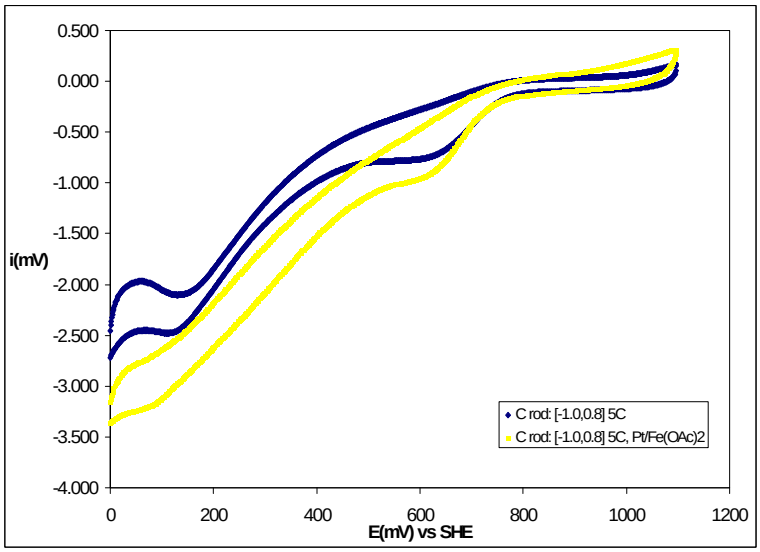

Figure 37: A graph of rotating disk voltammetry (1600 rpm) of oxygen reduction by platinum phosphate composite catalyst composed of predominantly mixed-valence species (0.05 mg/cm2; geometric area 0.196 cm2) and augmented by iron (<0.02 mg/cm2).

Methanol Oxidation

The voltammograms obtained from methanol oxidation using the composite catalyst was compared with those obtained using a pure metallic platinum wire. In this case, Pt-wire was used as the working electrode. The auxiliary and reference electrodes remained the same.

The two peaks observed at 908 mV and 708 mV for the composite catalyst are due to the methanol oxidation and CO oxidation. These two peaks can be compared with the corresponding two peaks at 990 mV and 708 mV for the bare platinum wire. Note that the position of the

methanol oxidation peak has been shifted 80 mV toward less positive voltage indicating that the platinum-phosphate composite is a better catalyst than platinum metal. Second, repeated scans on the composite catalyst did not show any signs for deactivation of the composite catalyst due to CO poising as indicated in Figure 38.

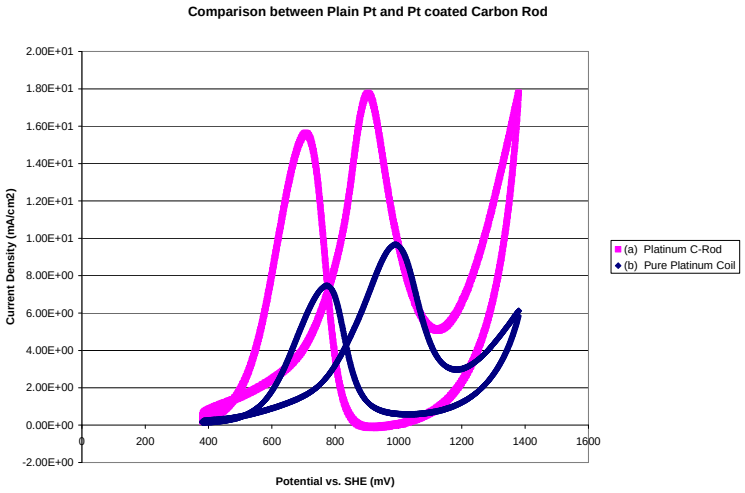

Figure 38: A current-voltage diagram for methanol oxidation by a platinum phosphate composite catalyst (pink) (0.08 mg/cm^2) on carbon rod and by bare platinum metal (blue) of platinum oxide for the conventional platinum metal.

Furthermore, when ruthenium was incorporated into the metal phosphate composite, no additional advantages in CO oxidation or potential shifting towards less potential were gained. These features indicate that metal phosphate catalyst is superior over other methanol oxidation catalyst.

Novel Catalyst Support

The novel catalyst support, nanoporous BCMS was characterized through X-ray photoelectron spectroscopy (XPS) shown in Figure 39 clearly indicate that the elemental composition of Boron Carbon ratio of 1:9 with high purity.

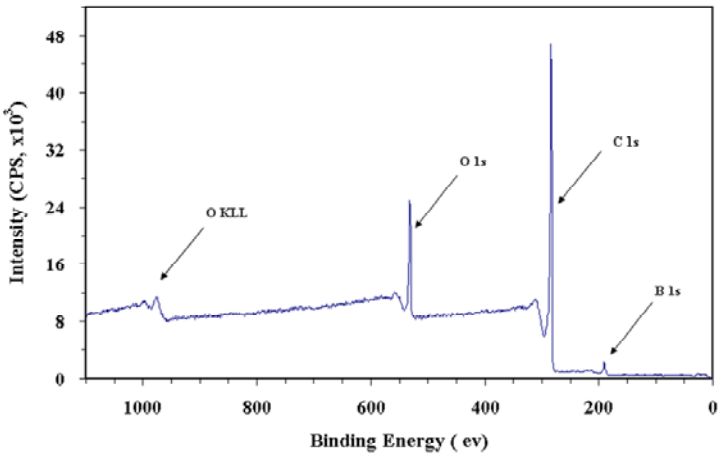

Figure 39: X-ray photoelectron spectroscopy (XPS) of nano-porous Boron carbide micro-spheres (BCMS).

High resolution scanning electron microscopy (SEM) in Figure 40 distinctly indicates uniformly distributed spheres with mesopores separation. The high purity uniform BCMS are about 500nm in diameter and reasonably high surface area, approximately 220 m^2/g obtained from Nitrogen Adsorption measurement. The beauty of these BCMS would allow uniform packing with mesoporous spacing because of their spherical nature.

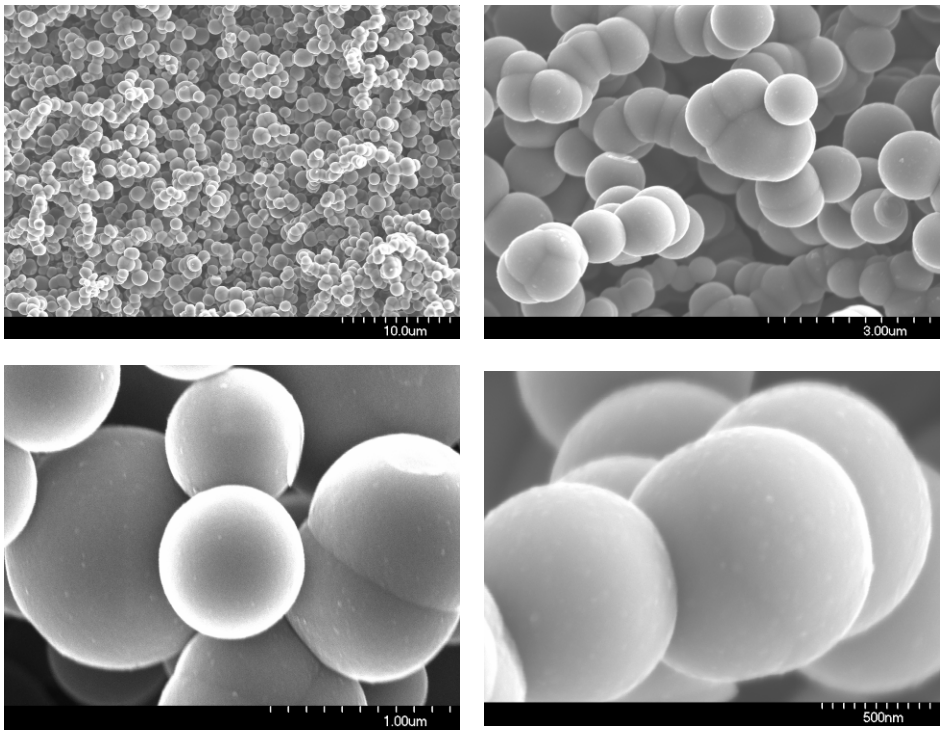

Figure 40: SEM micrograph of novel nanoporous Boron Carbide Micro-Sphere (BCMS)

Thermo Gravimetric Analysis (TGA) measurement in Figure 41 clearly demonstrates that the oxidation stability is quite high, very much comparable to pure multi-wall nano-tubes. Result also indicates that BCMS posses the electrical conductivity higher than carbon black and comparable to carbon nono-tubes.

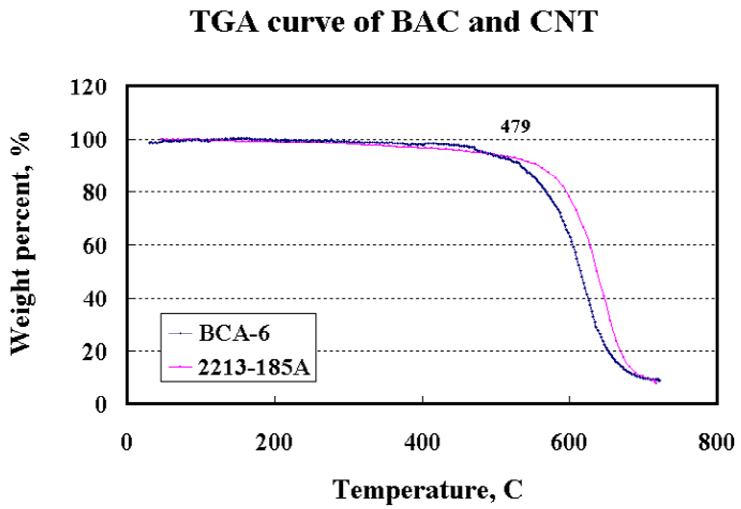

Figure 41: The thermal oxidation comparison of Boron-Carbide micro-sphere (BCMS) and carbon nano-tubes (CNT) through Thermo Gravimetric Analysis (TGA) measurement.

High thermally stable, high electrical conductive, highly porous specially spherical nature pure BCMS would be the candidate from supporting catalyst to replacing ITO in electronic devices to filling the solar radiation absorbing liquid to fluid filtering bed for medical application to anchoring drug for drug delivery and others. The spherical shape would bring advantages over all form of carbon materials such as carbon nanotube, carbon nanofiber, etc.

This novel nanoporous BCMS structure and oxidation stability would bring tremendous potential advantages over conventional Vulcan XC-72 (Cabot) in corrosion of catalyst support that move forward in improving the durability of low and medium temperature fuel cells, especially PEMFC. The BCMS material is a very promising catalyst support with several potential advantages over conventional Vulcan XC-72 (Cabot): 1) enhanced interaction with the catalyst which can potentially improve the catalyst stability [118], 2) high electronic conductivity, 3) spherical particle shape resulting in uniform packing density [119-121], and 4) the ability to maintain the porous structure during fuel cell operation.

Bipolar Plates

Typical contour plots for static, dynamic and total pressure over the surface of the bipolar plate by using multiple parallel bipolar plates are shown in Figure 42. With the consideration of this design a more uniform pressure distribution as well as lower pressure drop across the plate is achieved.

Figure 43 shows a comparison of different bipolar plate design in term of pressure drop (coefficient of pressure). Results show considerable enhancement of pressure drop with four-channel design compared to any other design considered.

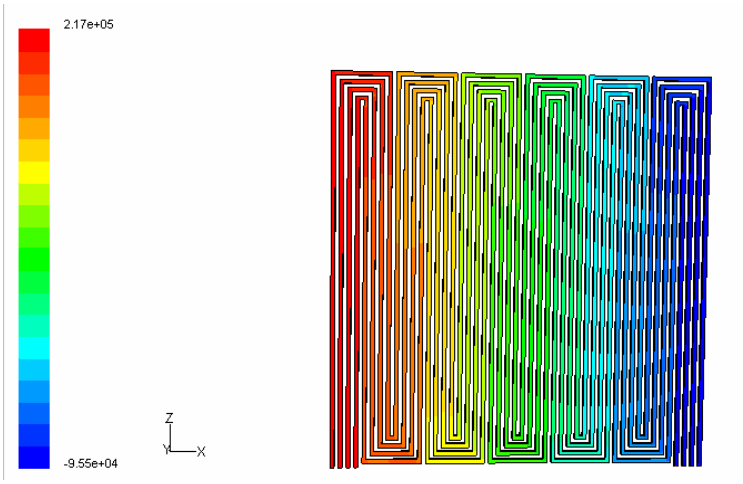

(a) Static pressure contours

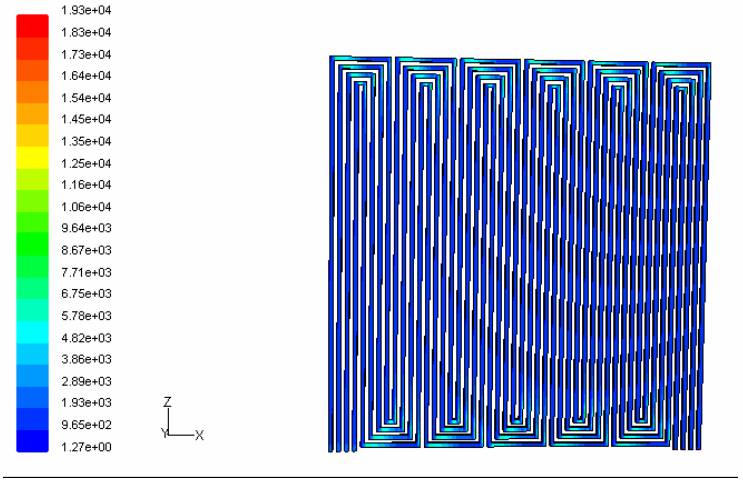

(b) Dynamic pressure contours

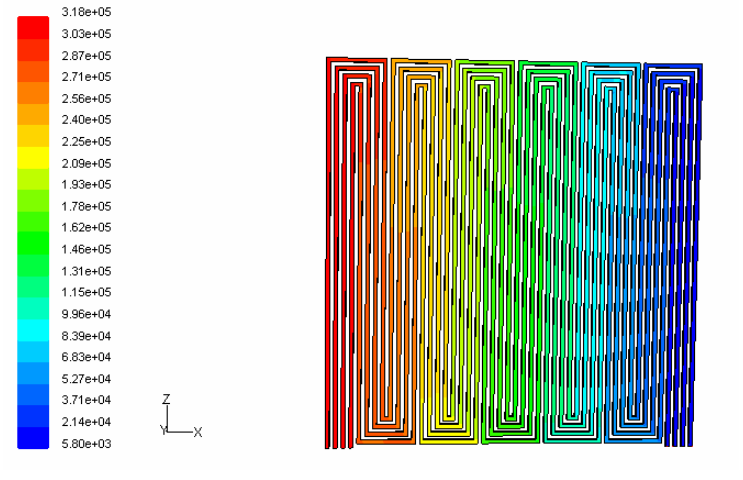

(c) Absolute pressure contours

Figure 42: Four channel bipolar plate design with pressure contours

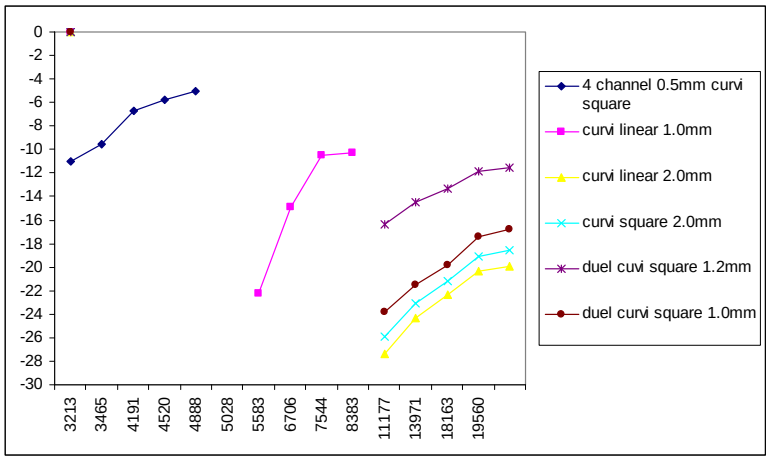

Figure 43: Comparison of pressure drops for different bipolar plate design.

The entry region correlations for Nusselt number and Sherwood number are derived for each type of bi-polar plate using the computational fluid dynamic simulation model. The curve fitted equation of the correlation of heat and mass transfer coefficient are integrated in the PEM fuel cell simulation model as discussed in the later section.

Testing and Performance Evaluation of Bipolar Plates

Figure 44 shows the simulated results for a bipolar plate with multiple straight parallel channels in comparison with experimental results for pressure drop. Results show close prediction of the computer simulation model. The deviation is primarily due to the inclusion of additional losses due to the entrance and exit port of the bipolar plate where the pressure tap is located. The experimental data were collected multiple times with both increasing and decreasing manner to ensure statistical reliability and precision of the experiment. Figure 45 shows the variation of Nusselt number with Reynolds number.

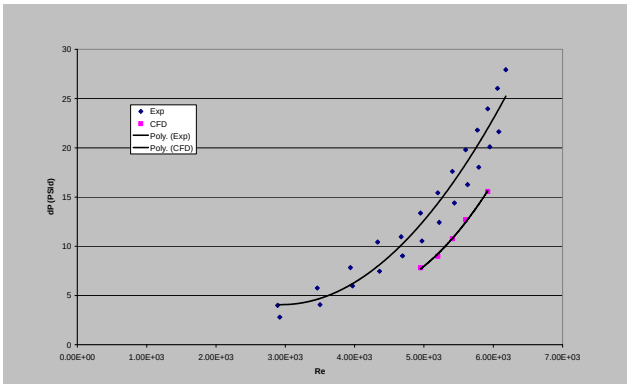

Figure 44: Comparison of simulated results with experimental data

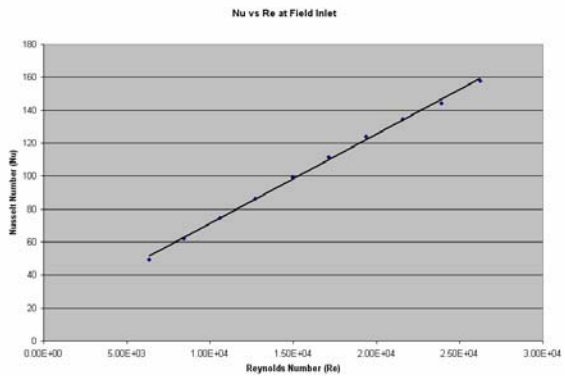

Figure 45: Variation of Nusselt number pressure drop with Reynolds number

Tests for pressure drop and heat transfer properties of two geometrically-identical bipolar plate flow fields fabricated out of stainless 303 and stainless 316 examined under transient condition

to evaluate heat dissipation capability with different gas flow rates. Cool-down data, both in terms of temperature and power for stainless steel apparatus follows shown in Figure 46.

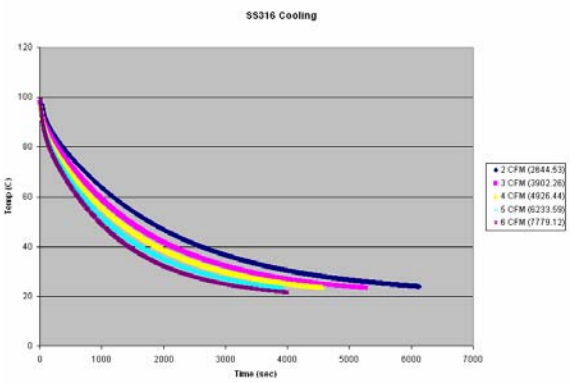

(a) SS-316 bipolar plate cool-down

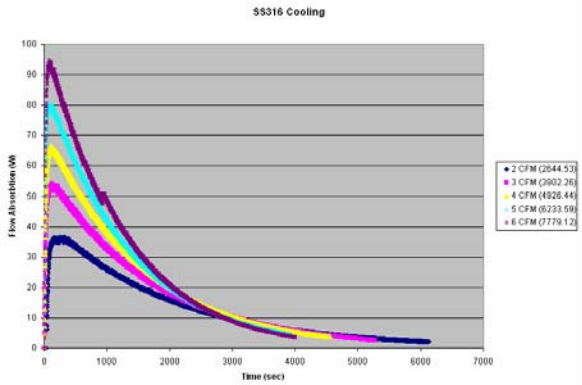

(b) SS-316 thermal power of gas flow.

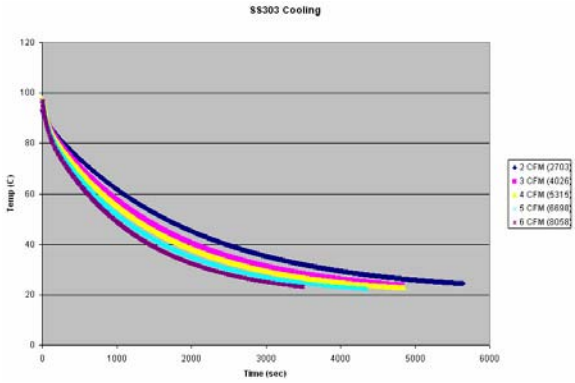

(c) SS-303 bipolar plate cool-down

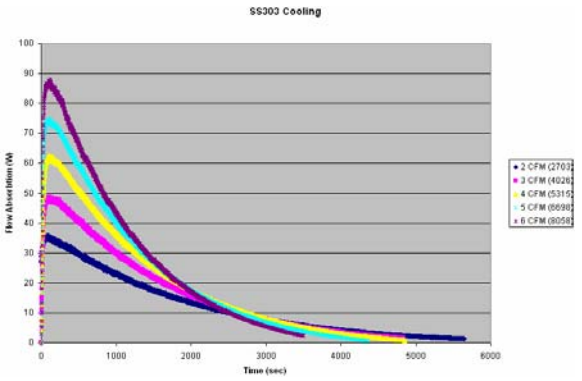

(d) SS-316 thermal power of gas flow

Figure 46: Bipolar plate cool down and thermal power of gas flow.

Based on the operational understanding gleaned from the small-scale tests, the future work focus on a full bipolar plate with integral cooling/heating, multi channel full bipolar design operating conditions that would be present in the sort of high-power fuel cell stacks used in transportation.

PEM Fuel Cell Simulation Results

In order to evaluate effect of the bipolar plate design on the PEM fuel cell performance in terms of mass transfer losses at higher current density, two-dimensional and three-dimensional simulation is carried out. A mesh refinement study is conducted to ensure the computational accuracy and convergence of the PEM fuel cell simulation model. Figure 47 shows typical three-dimensional mesh using tetrahedral element.

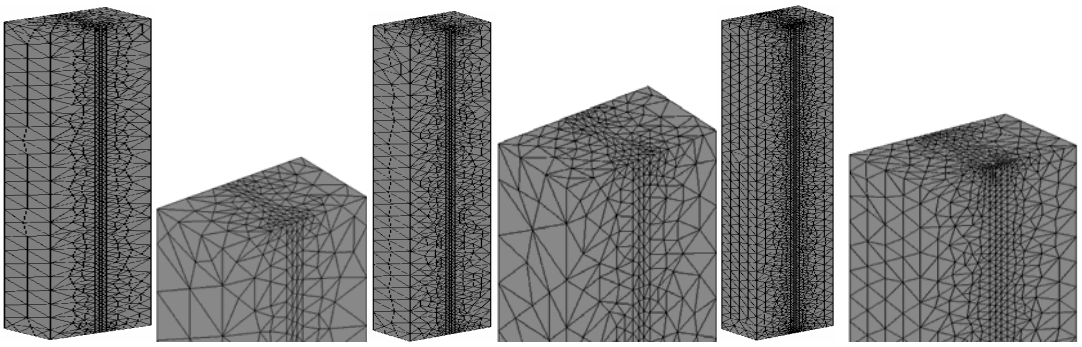

Mesh Case-1 Mesh Case -2 Mesh Case- 1

Figure 47: Different meshes for PEM fuel cell simulation.

Tri-layer PEM fuel cell is analyzed over arrange operating and geometrical parameters such current density, stoichiometric ratio and number and size of gas flow channels in the bipolar plate. Results gave considerable insight into the operating mechanism of PEM fuel cell as shown in the following figures. The base-case analysis is performed for a 2-mm square channel of 22,885 elements and solved at operating current densities of 0.5, 1.0 and 1.5 Amp/cm^2.

Hydrogen Concentration Distribution in Tri-Layer PEMFC

Figures 48a-c show hydrogen concentration distributions across the anode channel and anode gas diffusion layers for current densities of 0.5 Amp/cm^2 , 1.0 Amp/cm^2 and 1.5 Amp/cm^2, respectively. Results in contour plots show decrease in hydrogen gas concentration in gas diffusion layer and in the channel down channel length. The decrease is mode predominant at higher current densities. Also, as expected there are non-uniform gas distributions in the diffusion layer with lower gas concentration near the land areas compared to the areas in contact with the channel. A detail sectional analysis of the data show that at higher current density, the consumption rate increases at the electrode-membrane interface and the hydrogen concentration under goes a wider variation across the diffusion layer and channel. Results show decrease in hydrogen gas concentration in gas diffusion layer and in the channel down channel length. The decrease is more predominant at higher current densities. Effect is more critical for the anode – membrane interface where the concentration value becomes zero and even negative to sustain the constant reaction. In reality, the reaction slows down or even stops as the gas supply system cannot supply required amount of gas to the interface. This scenario, however, strongly depends on the current density, and deferred with increase in stoichiometric ratio. Results show that at higher current density, the consumption rate increases at the electrode-membrane interface and the hydrogen concentration under goes a wider variation across the diffusion layer and channel. The variation is also steeper near the inlet section of the channel than the near the exit.

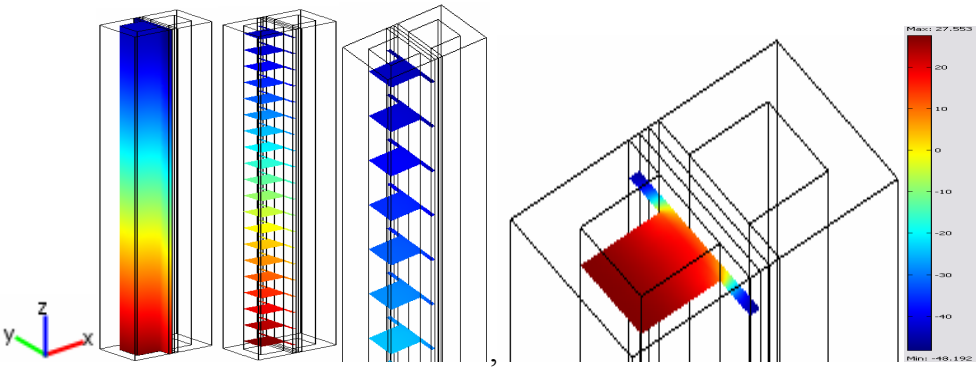

(a) hydrogen concentration distributions at 0.5 Amp/cm^2

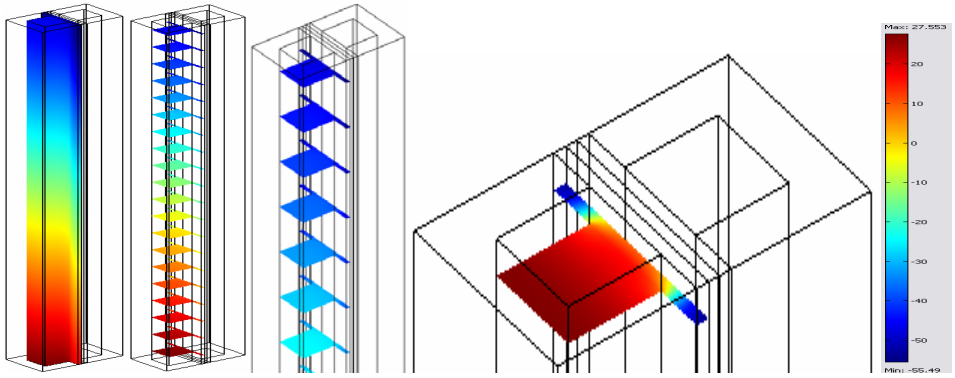

(b) hydrogen concentration distributions at 1.0 Amp/cm^2

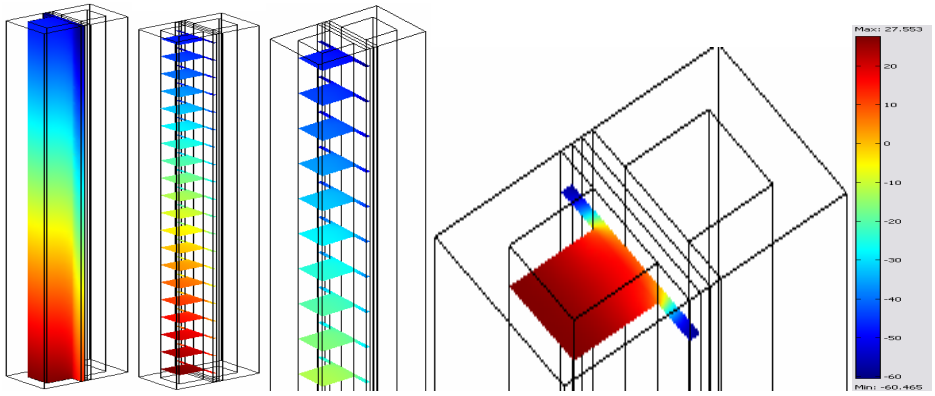

(c) hydrogen concentration distributions at 1.5 Amp/cm^2

Figure 48: Contour plots for hydrogen concentration distribution across the anode channel and anode diffusion layer.

Oxygen Concentration Distribution in Tri-layer PEMFC

Figures 49a-c show oxygen concentration distributions across the cathode channel and cathode gas diffusion layers for current densities of 0.5 Amp/cm^2, 1.0 Amp/cm^2 and 1.5 Amp/cm^2, respectively.

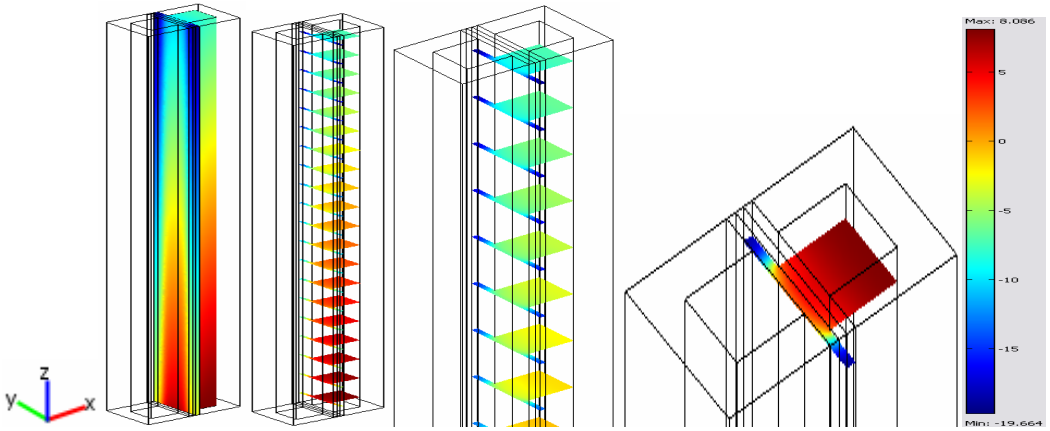

(a) oxygen distribution at 0.5 Amp/cm^2

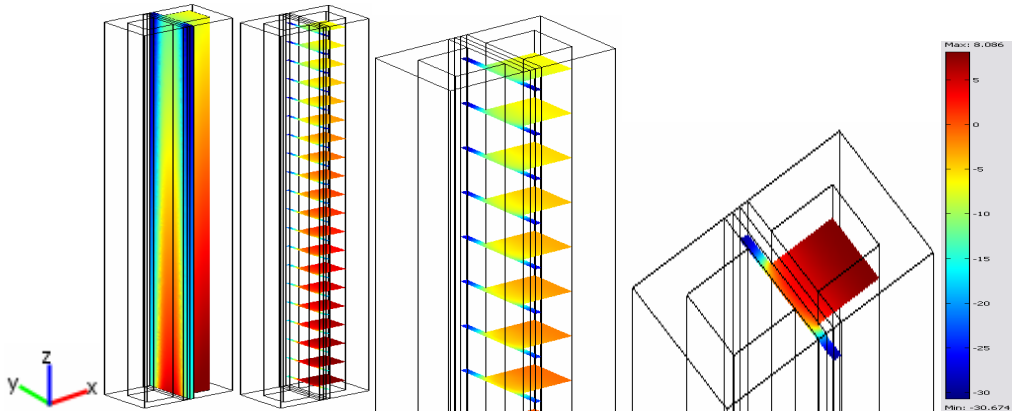

(b) oxygen distribution at 1 Amp/cm^2

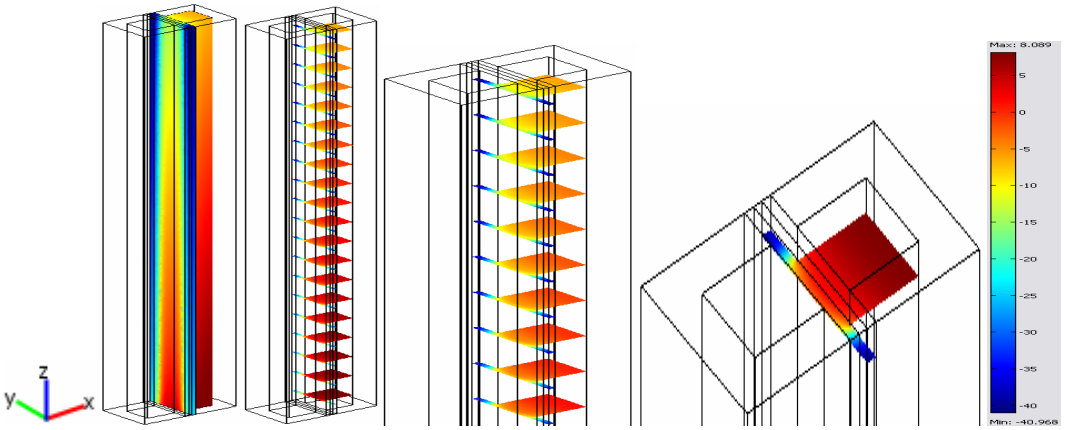

(c) oxygen distribution at 1.5 Amp/cm^2

Figure 49: Contour plots of oxygen concentration across the cell.

Contour plots of oxygen distribution show strong two-dimensional variation of concentration at the anode-membrane interface and also around the regions near the land areas. The line plots at different sections of the cell show stronger variation of oxygen concentration across the cell. Again the variations are stronger in the channel as well as in the gas diffusion layer with higher current densities.

Temperature Distribution in Tri-Layer PEMFC

Figure 50 shows temperature distribution plots across the cell from anode side to cathode side. It can be mentioned again here that the heat generation is primary due to irreversibility of reaction at cathode-membrane interface and implemented as surface phenomena. In addition, the objective would be to maintain the cell at a uniform cell temperature level.

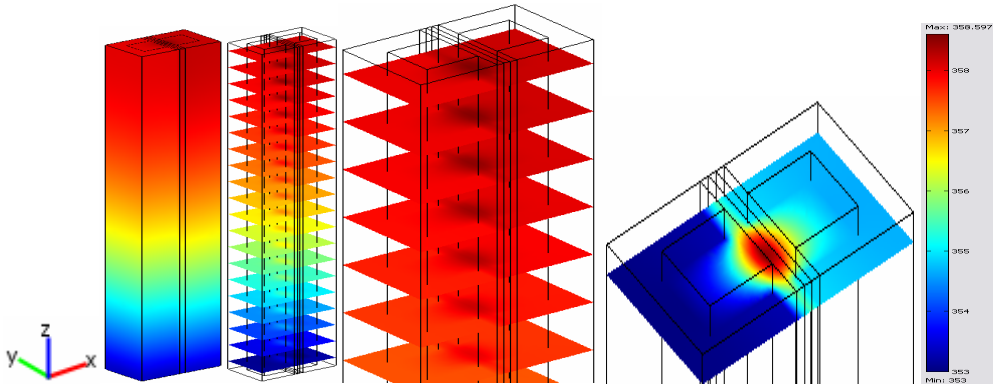

(a) Temperature profile at 0.5 Amp/cm^2

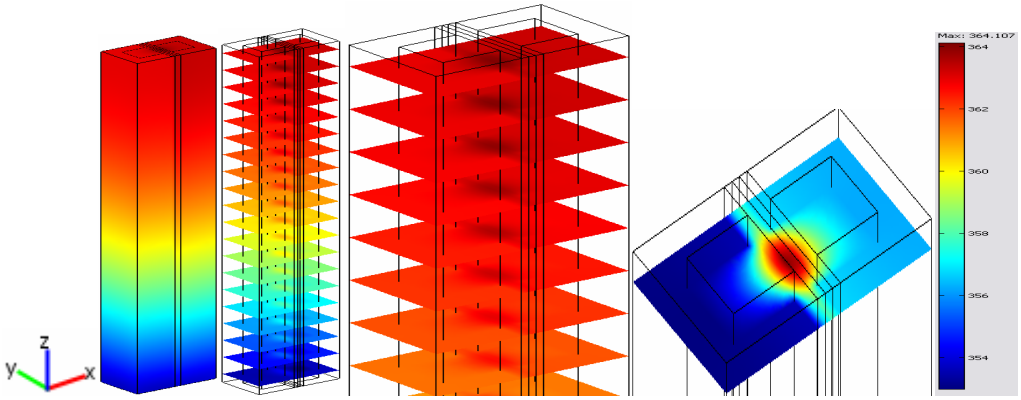

(b) Temperature profile at 1 Amp/cm^2

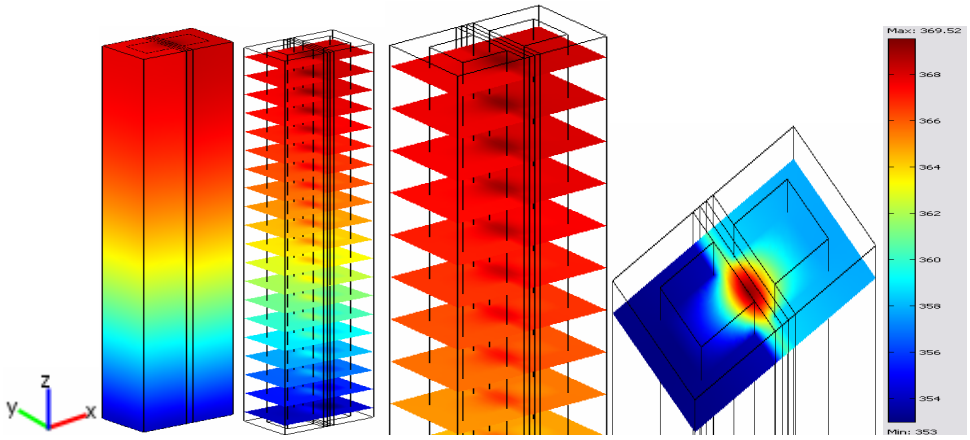

(c) Temperature profile at 1.5 Amp/cm^2

Figure 50: Contour plots of temperature across a cell for different current densities.

Results show the anode and cathode gas flows are more effective in transferring heat away from the cell at the inlet section because of the bigger temperature difference and entry length effect. The maximum and average temperature levels increase slightly with higher operating current density and the temperature is increasing from inlet to outlet. This indicats that the gas stream is effective in carrying away the heat generated in the cell. Temperature profile shows higher temperatures at core of the fuel cell.

Water Distribution in Tri-Layer PEMFC

Water concentration maps show in Figure 51 the increased level of water content in the cathode side over the anode side. Gas flows in the cathode side carries away more amount of water as evident by the increase in concentration at the exit section. Water generation as well as level of water content increases with operating current densities.

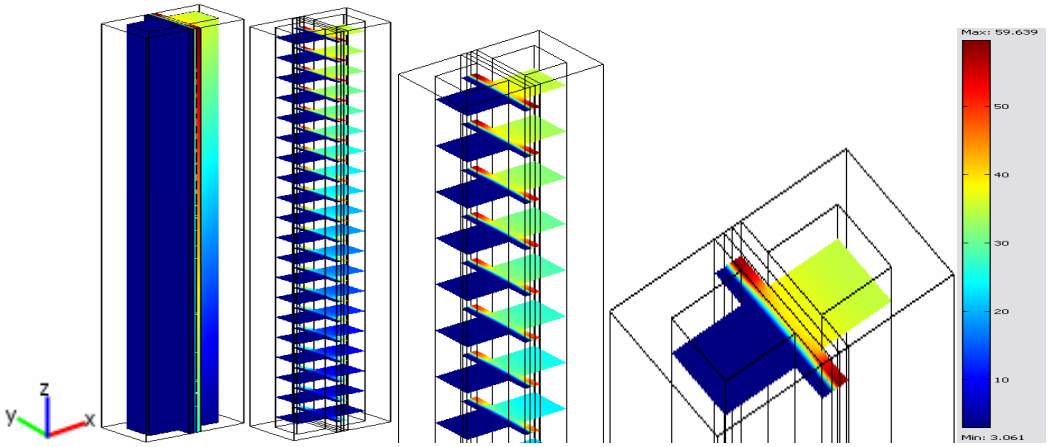

(a) Water concentration at 0.5 Amp/cm^2

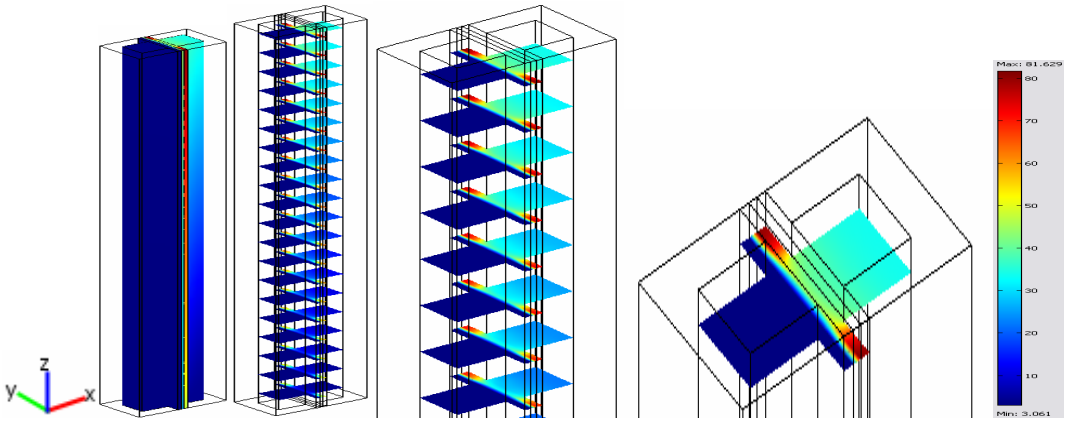

(b) Water concentration at 1 Amp/cm^2

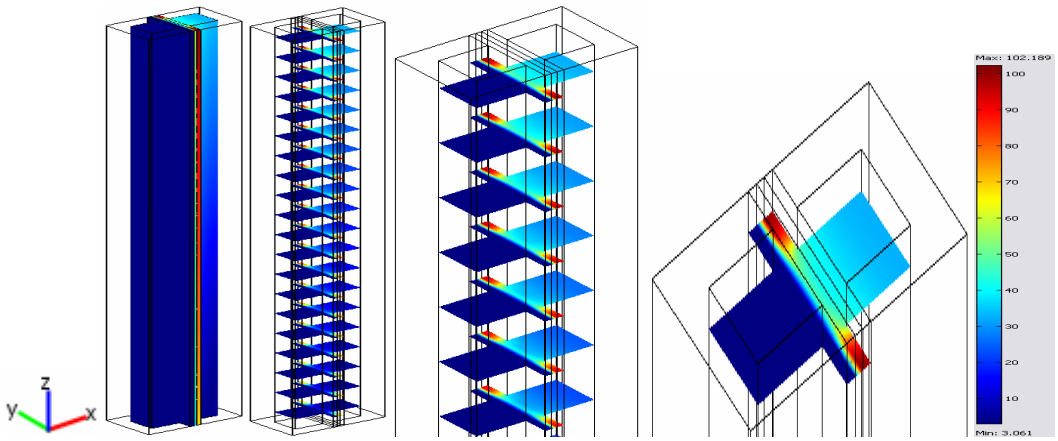

(c) Water concentration at 1.5 Amp/cm^2

Figure 51: Contour plots of water across the cell at different current densities.

It is evident that the pickup of water is higher on cathode side channel compared to anode side channel. As the current density increases, there is a slight increase in pickup of water on anode side. However, as we go along the channel, the pickup of water on cathode side decreases slightly because of accumulation of water between membrane and cathode gas diffusion layer.

Cell Performance

Figure 52 shows performance of the cell for both single channel and twin channel for different level of stoichiometric ratios. With increased level of gas mass flow rate, by using higher stoichiometric ratio, mass transfer losses significantly improve. This helps to increase the limiting current density and operating current-voltage level for channel case. The cell potential drops out early because of lack of supply of fuel at lower stoichiometric ratios. But as the stoichiometric ratio increases the cell burns out at much higher current densities, i.e. increasing the limiting current density.

However, for twin channel the mass transfer losses are significantly reduced and hence improve the operating voltage at a given operating current density. Since the concentration distribution improved with the use of the twin channel, there is no additional benefit with increasing stoichiometric ratio from 1.5 to 2.5.

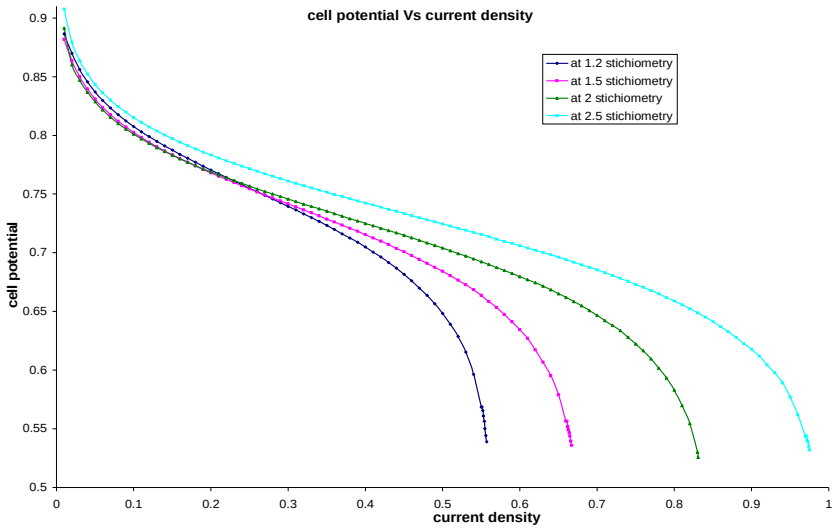

(a) 1-mm channels

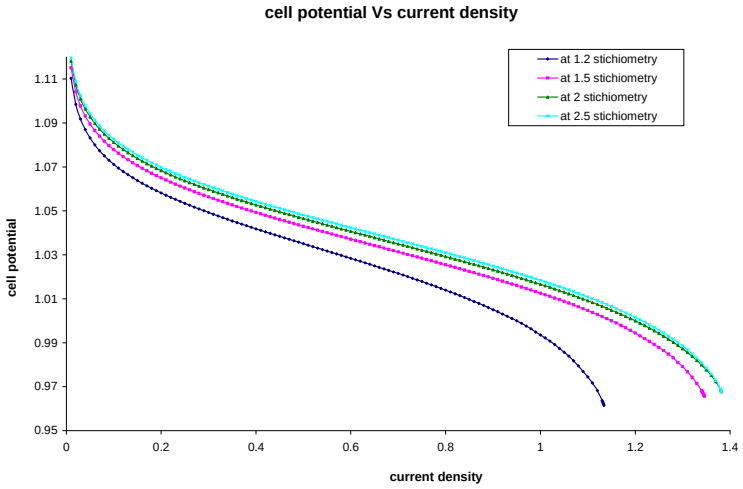

(b) 0.5 mm channel

Figure 52: PEM fuel cell performance with varying level of stoichiometric ratios.

Effect of Bi-Polar Plate Design on Polarization Curve

Bi-polar plate plays a significant role on the performance of a PEM fuel cell in terms of mass transfer losses, particularly at higher current densities. The bi-plate has its less effect on activation losses also, but less compared to that of mass transfer losses. In order to show the effect of bipolar plate design on the performance of the fuel cell, voltage-current polarization curves are drawn as function operating current density for different designs. Figure 53 shows the polarization curve for different bi-polar plate designs for a stoichiometric ratio 3.0, 2.5 and 1.5.

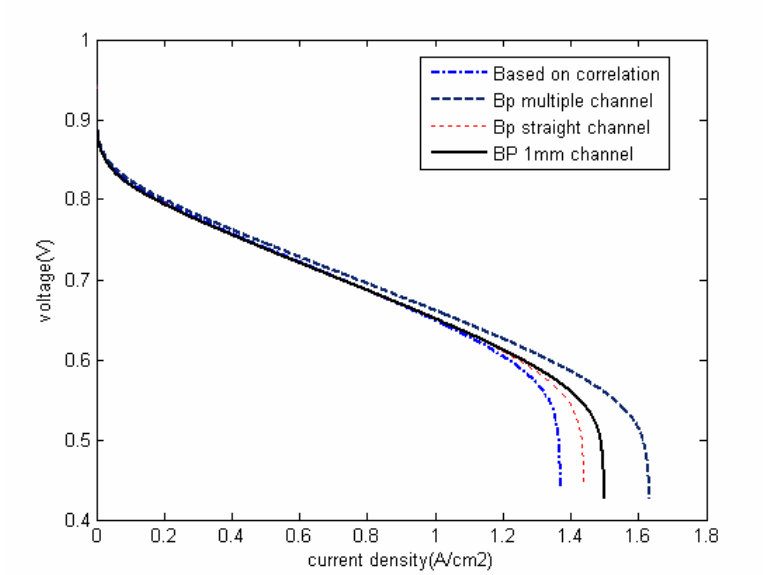

(a) Stoichiometric ratio 3.0

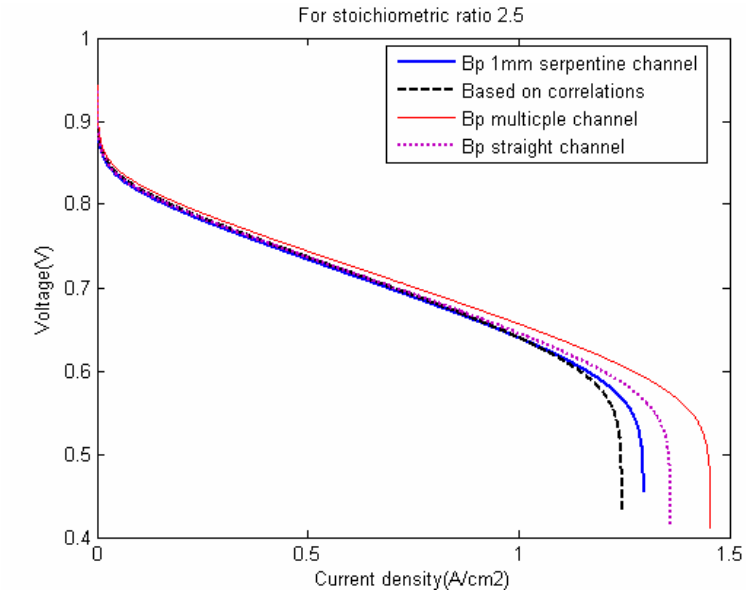

(b) Stoichiometric ratio 2.5

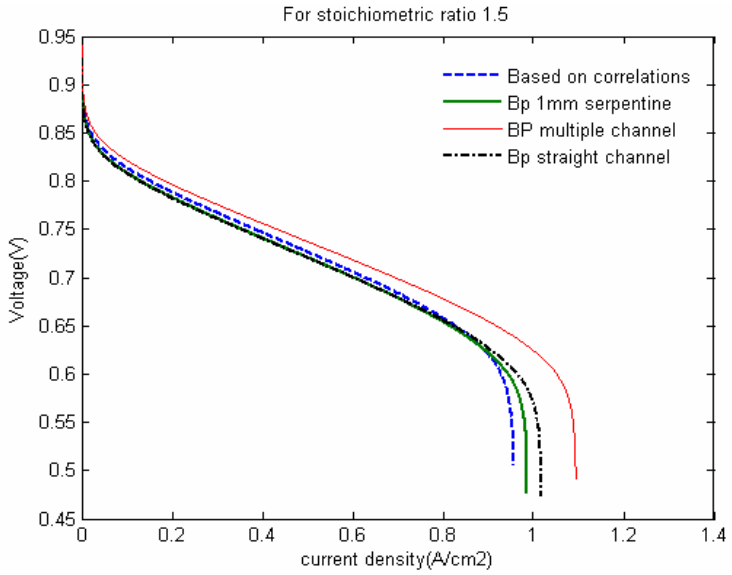

(c) Stoichiometric ratio 1.5

Figure 53: Polarization curve for different bi-polar plate designs for stoichiometric ratio.

With the bi-polar plate design with multiple channel has higher current density compared to that of other bi-polar plate designs. For the lower current densities, the effects of the bi-polar plate designs do not show any significant effect. At lower current densities, variation in activation losses do not change significant by the gas flow channel design as expected. But, at the higher current densities gas flow channel designs of different bipolar plate show significant effect on the performance in terms of limiting current density and mass transfer losses. The output voltage corresponding to the current density for different bi-polar plate designs show that the voltage is dropping sharply at higher current densities.

With the multiple parallel channel design, the limiting current density is significantly enhanced. The mass transfer looses are reduced increasingly at a higher current density compared to bas case and other channel designs. At a current density of 1.0 A/cm2, the variation in the output voltage between in base model and multiple channel bi-polar plate design is about 0.05 V. Stoichiometric ratio plays an important role in design and operation of the fuel cell. As it can be observed that by increasing the stoichiometric ratio the effect of mass transfer losses can be reduced with additional expense in terms of higher pressure drop and cost of operation.

Thermo-Mechanical Analysis of Fuel Cell with Bi-Polar Plate

A thermo-mechanical analysis is carried out to analyze the performance of a PEMFC integrated with the bipolar plate design with selected material of construction, gas flow channel size, and with or without cooling in terms of heat dissipation capacity, induced thermal stress, and weight of the bipolar plate. The analysis model is based on conjugate heat transfer with heat diffusion in solid and diffusion and convection in the gas channels. Mass flow rates and heat generation rate corresponding to the consumption rates of both reacting gases are considered to study the heat dissipation rate through the bipolar plate.

Overall thickness is also varied with the objective to reduce the weight of the bipolar plate. While bringing down the material thickness, the bipolar plate become structurally weak and develops stresses, which needs to be checked for failure as well as for manufacturing feasibility.

Thermal stress analysis is carried out to study the induced stress on the plate during the operation, and ensure structural integrity of the bipolar plate. Typical results for temperature and stress distributions across the bipolar plate are shown in Figures 54 and 55.

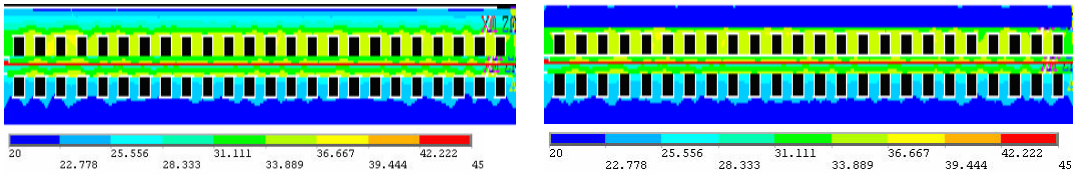

(a) Cooling at hydrogen side only (b) Cooling at both hydrogen and oxygen sides

Figure 54: Temperature distribution across the bipolar plate.

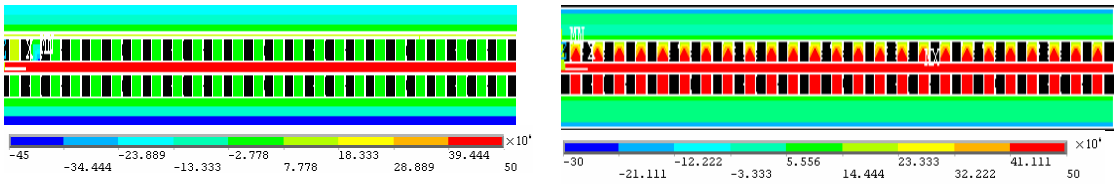

(a) Cooling along endplates (b) Adiabatic condition along endplates

Figure 55: Contour thermal stress plot in a bipolar plate with 1×1×50mm channel size with current density of 1.4Amp/cm2.

Results show that the generation of heat at the cathode-membrane interface leads to expansion of cathode and membrane interface materials. This expansion develops stress when run under steady operating conditions. When bi-polar plates are subjected to sudden cooling, the stress concentration increases rapidly due to compression of material. Stress developed during adiabatic runs of the bipolar plate is considerably less as compared to endplates run under cooling conditions.

A number of bipolar plate designs have been considered during this study with an objective to optimize the design in terms of total heat dissipation, gas flow cross-sectional area, and weight. Results showed that carbon composite is a better material in terms of heat dissipation than stainless steel and graphite. However, by reducing the thickness of the plate and reducing the channel size, the internal and channel resistance decrease, and stainless steel and graphite match thermal effectiveness of carbon composite bipolar plates.

Simulation of bipolar plate designs with and without at cooling under varying the current density showed that cooling is required at a higher current density while at lower densities convection due flowing gases is sufficient. Thermal stress analysis proved that stainless steel is a better material than carbon composite and graphite in terms of mechanical and structural integrity when exposed to cooling conditions.

Single Cell Performance Evaluation

Platinum Phosphate Blue Cathode Catalyst

The cell performance measurements of all MEAs were conducted at 60°C and 80°C using H_2/O_2 with flow rates of 0.2 L/min for both H_2 and O_2, with both gases humidified to 100% relative

humidity (RH) using a Fuel Cell Test Station 890CL (Scribner Associates Inc.). For the cathode electrochemically-active surface area measurements, a typical half-cell configuration was used by passing nitrogen at the cathode and hydrogen at the anode by coupling Corrware (Scribner Associates Inc.) and SI 1287 (Solatron Analytical) potentiostat at scan rate 30 mV/s between 0 to 0.8 V. The cell performance curves are shown in Figure 56.

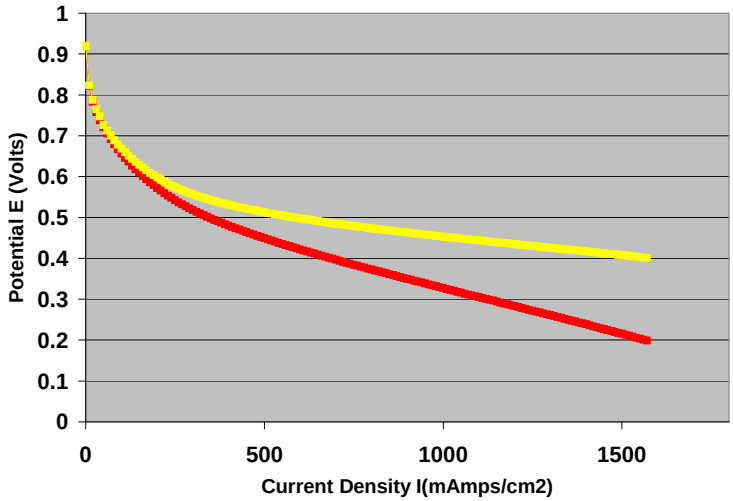

Figure 56: A graph of non-Resistance (IR) free and IR fre e performance curves of membrane electrode assembly (MEA) at 80 degrees C operated on H_2/O_2 at 80/80/80 degrees C of $T_{cell}/T_{cathode\ humidity}/T_{anode\ humidity}$ operated at 100% relative humidity (RH).

The red curve in Figure 56 represents non-IR free performance and the yellow curve represents IR free cell performance. The cathode was prepared with a platinum phosphate composite catalyst with platinum loading of 0.1 mg/cm^2. The open circuit voltage at 80 $^{\circ}$C was observed to be 0.98 V. Note that the performance was measured with five-times less platinum loading (0.1 mg_{pt}/cm^2) than commercial catalyst.

The above experiment demonstrated that the metal phosphate composite catalyst functions effectively in the proton exchange membrane fuel cell. However, no attempts were made to optimize the performance and hence the power densities reflected in Figure 56 can only be viewed as the evidence of performance, rather than a measure of total capacity of the catalyst. Optimization of power density would require further engineering including fabrication, mounting, control of humidity, and other parameters that control the power density.

Nafion® and Commercially Available Catalyst

To evaluate the curing dynamics effect on cell performance, a number of MEAs with identical catalyst and ionomer compositions were prepared under different curing conditions and their performances were evaluated [55]. Three such MEAs representing two extremes in performance will be discussed in detail. Figures 57 through 59 show typical polarization curves, taken at 60°C and 80°C, for the three MEAs. A summary of the performance data at both 60°C and 80°C is given in Table 3.

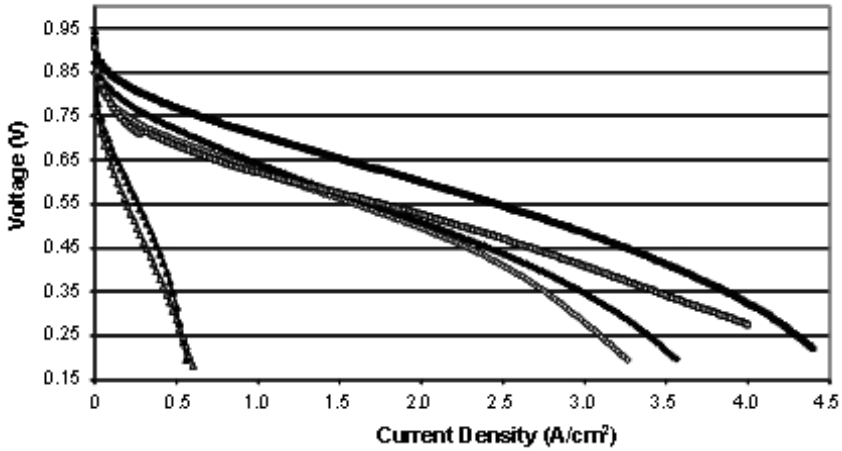

Figure 57: Non-IR free performance curves of MEA-1, MEA-2, and MEA-3 at 60°C & 80°C operated on H_2/O_2 at 60/60/60°C and 80/80/80°C of $T_{cell}/T_{cathode\ humidity}/T_{anode\ humidity}$. ●-MEA-1 at 80°C ; ■-MEA-2 at 80°C; ▲-MEA-3 at 80°C (hollow symbols represent 60°C performances)

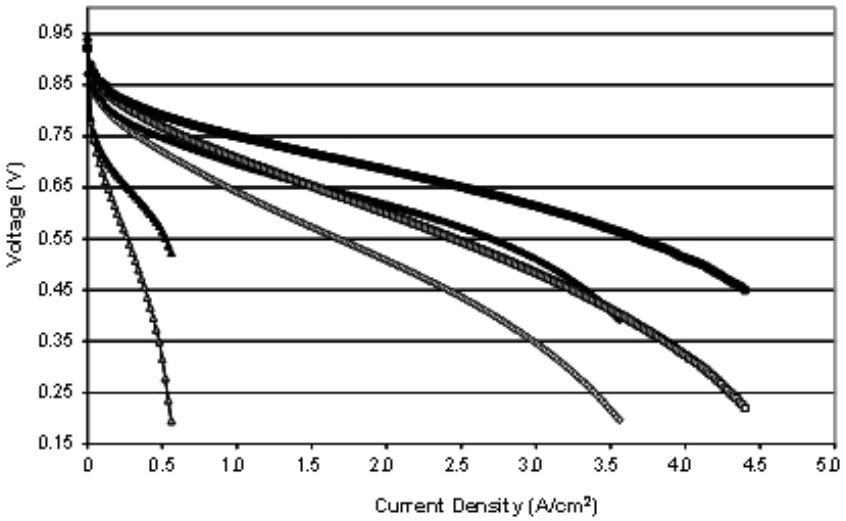

Figure 58: Polarization (IR free & non- IR free) curves of MEA-1, MEA-2 & MEA-3 operated on H_2/O_2 at 80/80/80°C of $T_{cell}/T_{cat\ humidity}/T_{anode\ humidity}$. ●-MEA-1 at 80°C; ■-MEA-2 at 80°C; ▲-MEA-3 at 80°C (hollow symbols represent non-IR free performances at 80°C).

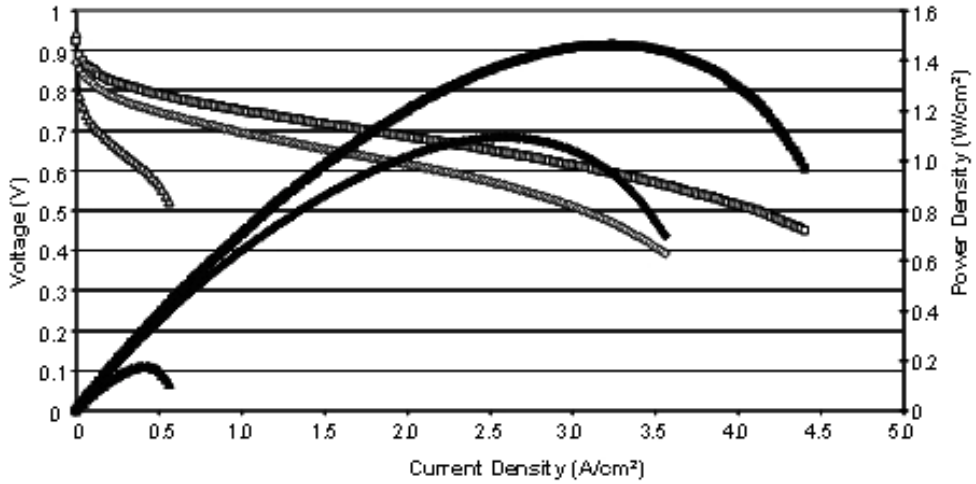

Figure 59: Performance and power density curves of MEA-1, MEA-2, and MEA-3 operated on H_2/O_2 at 80/80/80°C of $T_{cell}/T_{cat\ humidity}/T_{anode\ at\ 100\%\ RH.}$ ●-power of MEA-1 at 80°C; ■-power of MEA-2 at 80°C; ▲-power of MEA-3 at 80°C (hollow symbols represent the corresponding potentials).

Table 3: Comparison of MEA-1, MEA-2 and MEA-3 at 60ºC & 80ºC

Measurement	Temperature (°C)	MEA-1	MEA-2	MEA-3
OCP (Volts)	60	0.831	0.922	0.906
	80	0.846	0.943	0.920
ECA (m^2/g-Pt)		34.9	32.9	36.7
ECA (cm^2-Pt/cm^2-electrode)		174	165	183
Current Density @0.7V(mA/cm^2)	60	460	40	400
	80	620	80	1060
Peak Power (Watts)	60	5.47	0.761	6.13
	80	5.16	0.873	7.32
Current Density@peak power(mA/cm^2)	60	2640	440	3060
	80	2420	420	3240
Resistance (Ω-cm^2)	60	0.01877	0.032416	0.01887
	80	0.018268	0.031881	0.01779
Conductivity (S/cm)	60	0.066	0.0385	0.0665
	80	0.0684	0.0392	0.0700

As can be seen from the Figure 59 and Table 3, the peak power densities for the best performing MEA, MEA-3, at 60°C and 80°C were observed to be 1.226 W/cm^2 and 1.462 W/cm^2, respectively. Similarly, the current densities at these temperatures were 0.4 A/cm^2 and 1.06 A/cm^2, respectively, at a potential of 0.7V. The current and power densities for MEA-1 and MEA-3 approach those reported in the literature for similar test conditions [122].

The distinct difference between the three MEAs was the conditions under which they were cured. This difference in the conditions of the curing process led to a wide variation in performance. These conditions include variation in drying temperature and time between the consecutive sprays during the curing process. In MEA-1, a slow electrode drying process yielded 1.104 W/cm^2 peak power density at 2.78 A/cm^2 and 80°C. Whereas for MEA-2, fabricated using a faster electrode curing process afforded only 0.1948 W/cm^2 peak power density at 0.44 A/cm^2 and 80°C. Likewise, MEA-1 exhibits a current density of 0.46 A/cm^2 at 0.7 V compared to 80 mA/cm^2 for MEA-2 at the same potential. MEA-3, which was prepared using a slow curing process like that of MEA-1, exhibited a peak power density of 1.464 W/cm^2 at 80°C.

The higher performance of MEA-3 compared to MEA-1 is due to a thinner membrane (20 μm for MEA-3 as compared to 30 μm for MEA-1). It is known that cells containing Nafion® perform better at 80°C than at 60°C [59], which was observed for both MEA-1 and MEA-3, as shown in Table 3. However, MEA-2 did not show any improvement in cell performance by raising the temperature from 60°C to 80°C, which implies that the performance was not limited by a temperature-dependent process, such as proton conduction, but by a relatively temperature-independent process, such as reactant mass transfer. Since MEA-3 had a different membrane thickness than the other MEAs, we will focus the remainder of our analysis on the other two MEAs, MEA-1 and MEA-2, which had identical membrane thicknesses.

To fully understand the large difference in performance between MEA-1 and MEA-2, which had identical compositions, detailed electrochemical and morphological analyses were performed. To determine the source of the cell resistance among all possible sources of resistance (activation, ohmic, and mass transport) responsible for the differences in performance, the ohmic resistances of MEA-1, MEA-2, and MEA-3 were determined, Table 3, by the current interrupt technique.

This ohmic resistance was used to determine the IR-free performances of these three MEAs (Figure 58). As can be seen from Figure 58, there is contribution from mass transfer resistance only at the higher current densities, above 2 A/cm^2, for the better-performing MEA's, MEA-1 and MEA-3. However, after IR correction, MEA-2 showed significant signs of activation losses and of mass transfer losses at virtually all current densities.

Cyclic voltammograms (CVs) of the cathodes were collected in order to compare the electrochemically-active surface areas (ECSA) of the platinum electrocatalysts. The half-cell CVs were obtained in the potential range of 0 to 0.8 V at a scan rate of 30 mV/s. The calculated ECSAs, assuming a total platinum loading of 2.5 mg, in MEA-1 and MEA-2 were 34.9m^2/g-Pt and 32.9m^2/g-Pt, respectively. These calculations show that these two MEAs have comparable ECSAs and that the differences in the performances of these two MEAs cannot be attributed to differences in the amount of cathode catalyst surface area in contact with both an electronic and ionic conductor.

To understand the performance variations, SEM images and EDX elemental maps were acquired to reveal the morphology and structure of the catalyst layer, examples of which are shown in

Figures 60 through 63. There were distinct differences between MEA-1 and MEA-2. The cathode of MEA-2, shown in Figure 60, clearly has a non-uniform thickness.

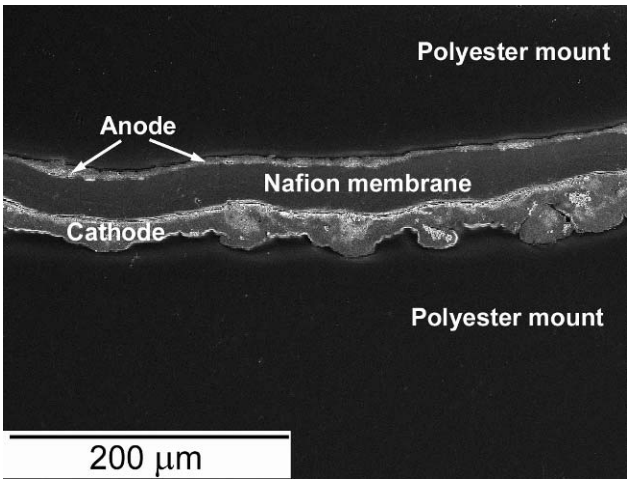

Figure 60: SEM image of MEA-2 cross-section showing large variations in the thickness of the cathode.

The outer surface of the cathode of MEA-2, which was in contact with the gas diffusion layer during the electrochemical tests, clearly has an uncommonly high surface roughness. A higher magnification image of the cathode of MEA-2 can be seen in Figure 61a. Figures 61b and 61c show EDX elemental maps of the Pt and F, respectively, for a selected area of Figure 61a. In the Pt map shown in Figure 61b, it can be seen that in MEA-2 there was regional clustering of platinum and the fluorine map in Figure 61c revealed uneven distributions of Nafion® as evidenced by the presence of several bright areas of the order of 10 μm in dimension that correspond to higher concentrations of fluorine along with several dark areas in the map that have lower fluorine concentrations.

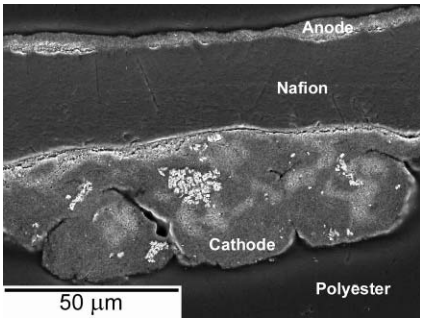

Figure 61a: SEM image of MEA-2 cathode cross-section.

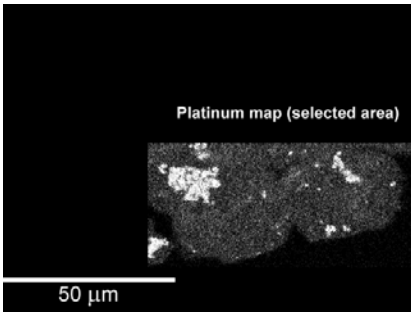

Figure 61b: EDX platinum map of MEA-2 cathode for a selected area of Figure 61a.

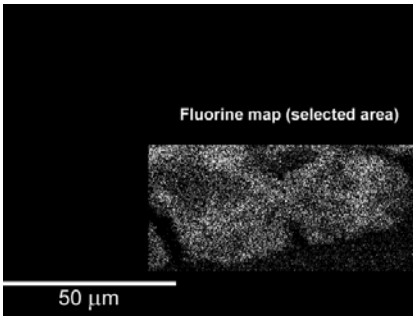

Figure 61c: EDX fluorine map of MEA-2 for a selected area of Figure 61a.

In contrast, SEM images of MEA-1 showed very few areas of Pt clustering, as seen in Figure 62. In these few clustered areas, catalyst agglomerations appeared to be much smaller. Also, the light and dark areas in the cathode of MEA-1 corresponding to fluorine are about 0.5 μm in diameter and evenly distributed through the electrode creating a more homogenous structure.

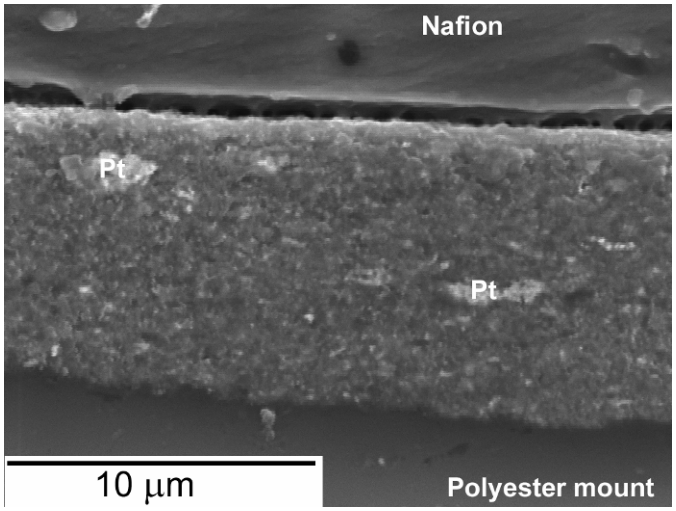

Figure 62: SEM image of MEA-1 cathode cross-section. A few small platinum agglomerates can be seen.

MEA-3, shown in Figure 63, also exhibits a catalyst morphology and homogeneous Nafion® distribution very much identical to that of MEA-1. Taking the images shown in Figures 60 through 63 collectively, it is quite clear that the distribution of Nafion® ionomer within the cathode of MEA-2 is extremely inhomogeneous in nature, compared to MEA-1 and MEA-3.

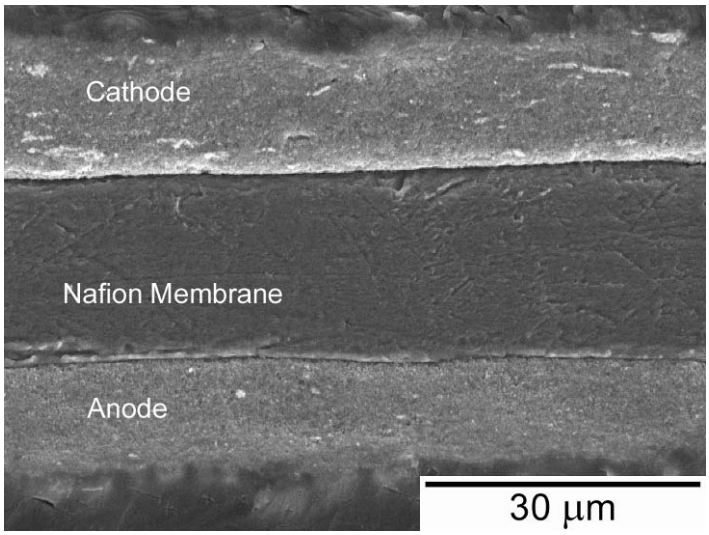

Figure 63: SEM image of MEA-3 cross-section.

The SEM images discussed above provide a clear correlation between performance and electrode structures for MEA-1 and MEA-2, which had identical electrode compositions and membrane thicknesses. The poor of performance of MEA-2 compared to MEA-1 is likely a result of the undesired localization of the ionomer. While MEA-1 and MEA-2 have nearly identical ECSAs, indicating that the catalyst utilization is identical for the two, despite the apparent clustering of the Pt in MEA-2, the distribution of the Nafion® ionomer is not the same, as shown in Figure 61c.

An ideal electrode microstructure would have the ionomer well dispersed in order to create the maximum number of triple phase boundaries between the Pt/C, ionomer, and gas pores [123]. In

the case of MEA-2 there are areas that are ionomer poorly distributed, thus we expect that there are fewer triple phase boundaries in those regions, which results in poor performance. Additionally, the areas that have high concentrations of ionomer may have blocked gas flow paths which could lower the performance of the MEA as well.

To enhance the performance of MEA at higher temperatures, we have added some reinforcing reagents to stabilize Nafion. Preliminary data collected at Ohio University (not shown) show MEAs with these composite Nafion materials can perform effectively up to 110 ^{o}C.

Multi- Cell Durability and Degradation Mechanisms

In our durability and degradation mechanism study of 100 W PEMFC stack in vehicle application a relatively brief cycling performed on the stack at Argonne National Laboratory included 74 cycles through the profile shown in Figure 19 and 354 cycles of a revised profile. In the revised profile, air was used in place of oxygen, the stack was brought to open circuit between load changes, and two of the low current peaks were removed to increase the amount of time in which the stack was running at high current. Three of the cells (1, 4, and 10) were also subjected to an accelerated degradation protocol. This accelerated degradation protocol involved cycling the potential on the cathode between 0.08 V and 1.2 V for 1500 cycles at 50 mV/sec. During the testing at Argonne, no irreversible degradation in stack performance was observed and the overall performance of the stack actually improved. The stack was then transferred to Northern Illinois University, where more extensive durability studies, described below, were performed.

Initial Performance

The initial performance of the stack using constant flow rates of hydrogen and oxygen of 1-1.24 SLPM and 1-1.18 SLPM, measured both at Argonne and at Northern Illinois University, was comparable to the performance curve supplied by the vendor with identical conditions (Figure 64). All further polarization curves shown in this report were taken with constant hydrogen and oxygen stoichiometry of 1.05 and 2.0.

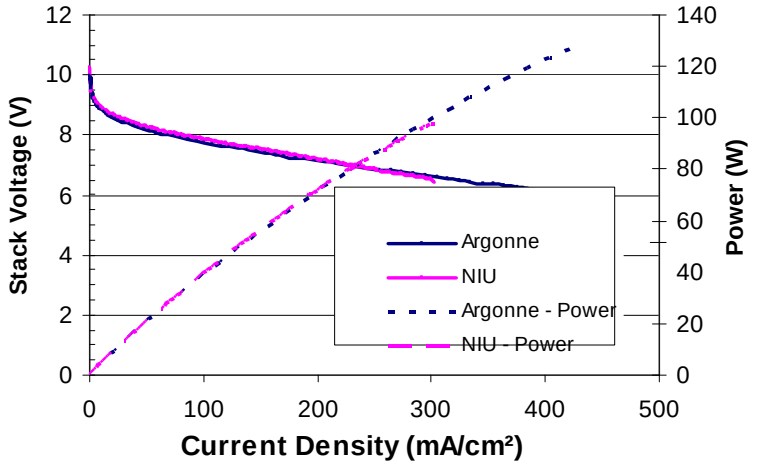

Figure 64: Initial polarization curve of the 10-cell stack. Conditions: Hydrogen/Oxygen, 0.75 bar/0.9 bar, T_{cell}=65°C, T_{H2hum} = 50°C T_{O2hum}= 55°C. Flow rates = 1-1.24 slpm H_2 and 1-1.18 slpm O_2.

A brief description of the factors affecting the dependence of fuel cell voltage on current (i.e., the polarization curve) is in order to provide a basis for the following discussion of the diagnosis of stack voltage losses. The voltage loss as a function of fuel cell current can be described by the following well-known equation (57) [124]:

$$V(i) = E_{rev} - (\eta act,O_2 + \eta act,H_2 + \eta conc,O_2 + \eta conc,H_2 + Ri) \quad (57)$$

Where E_{rev} is the thermodynamic potential for the O_2/H_2 reaction defined by the free energy of the fuel cell reaction and by the reactant concentrations and i is the cell current. The η's are the overpotentials. They are losses due to the kinetics of the cathode reaction (act and O_2 subscripts), with the kinetics of the anode reaction (act and H_2 subscripts) and the changes in concentrations of reactants due to mass transfer limitations (conc subscripts). Ri is the loss due to resistance to proton transport in the membrane, resistance to electronic transport in the electrode layer, resistance to electron transport in the gas diffusion layer and bipolar plate, and resistance at the interfaces between these components. The kinetics of the cathode reaction are orders of magnitude lower than those of the anode reaction and therefore this loss dominates the cell kinetic losses. The activation overpotential for the cathode kinetics are described in equation (58) [124]:

$$\eta_{act,O2} = (2.303\ RT/\alpha_c F) \log i_o - (2.303\ RT/\alpha_c F) \log i \quad (58)$$

Where $2.303\ RT/\alpha_c F$ is the Tafel slope and is approximately 70 mV/decade at 65°C [125] and i_o is the exchange current density for the oxygen reduction reaction and is 2-5 x 10^{-8} A/cm² Pt active area [126]. This equation shows that the measured potential at open circuit will deviate from the reversible or thermodynamic potential by $(2.303\ RT/\alpha_c F) \log i_o$. The Nafion® membrane is also permeable to hydrogen and the open circuit potential will be decreased by this hydrogen crossover from the anode to the cathode [124].

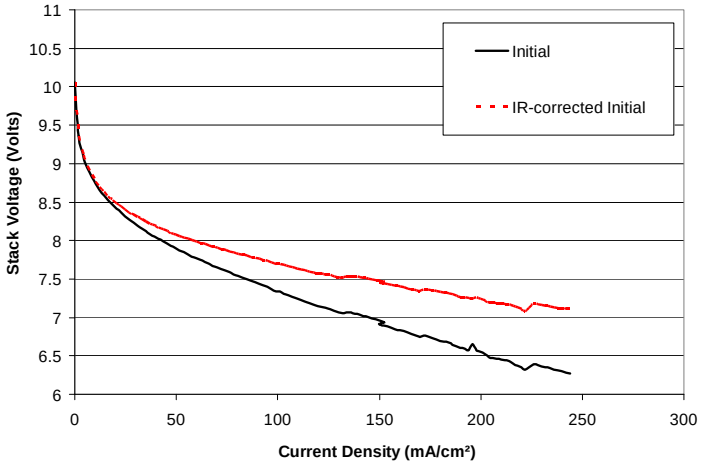

Figure 65: Initial polarization curve of the 10-cell stack under constant stoichiometric hydrogen and oxygen flows. Conditions: Hydrogen/Oxygen, 0.75 bar/0.9 bar, T_{cell}=65°C, T_{H2hum} = 50°C T_{O2hum}= 55°C. Constant stoichiometric ratio flow rates of 1.05 hydrogen and 2.0 oxygen.

Useful ways to diagnose cell and stack voltage losses are to correct the cell and stack polarization curves for iR losses and to plot this "iR-corrected" polarization curve versus the log

of the current density. This representation allows determination of the losses due to the concentration, or mass transfer, terms shown in equation (57).

The initial polarization curve taken under constant stoichiometry conditions is shown in Fig. 64, as well as the polarization curve corrected for "iR losses". As Figure 65 shows, 23% of the 3.24 V loss at 200 mA/cm² can be attributed to purely resistive losses (i.e., iR losses).

The initial individual cell polarization curves are shown in Fig. 66. Six cells (2, 3, 4, 5, 6, and 7) fell within a cell-to-cell voltage variation of 100 mV. Cells 1 and 10 had significantly worse performance, most likely due to poor transport of reactants or over-compression of these two end cells. Cells 8 and 9 showed intermediate performance. Diagnostics, as described in the appendix, were used to determine the sources of the cell voltage losses. The individual cell high frequency impedances (i.e., purely resistive impedance), as determined by the current interrupt technique, are shown in Table 4.

Table 4: High frequency resistance (mΩ-cm²)

Cell Number	Initial	After 240 h	After 480 h
1	392	409	381
2	228	215	235
3	207	213	219
4	643	507	452
5	213	218	219
6	197	190	197
7	379	275	265
8	538	415	318
9	395	362	304
10	450	442	364
Total	**3642**	**3248**	**2954**

The high frequency impedance reported by the stack manufacturer is 200 mΩ-cm². Within the uncertainty of the measurements, only four cells (2, 3, 5, and 6) show high frequency impedances consistent with that quoted by the manufacturer. The bulk of the high frequency impedance is due to the resistance to transport of protons through the membranes [127].

Table 5: Electrochemically-active surface area (m^2/g)

Cell	Initial	After 240 h	After 480 h	% Loss After 480 h
1	17.1	nd	nd	nd
2	21.8	23.3	13.9	36
3	25.0	30.9	13.8	45
4	21.5	14.7	9.4	56
5	19.2	17.7	12.6	34
6	20.8	23.2	15.7	25
7	21.3	nd	16.4	23
8	25.0	8.6	5.3	79
9	13.1	10.5	15.3	n/a
10	23.3	9.9	14.7	37

The higher than expected high frequency impedances for MEAs 1, 4, 7, 8, 9, and 10 are indicative of inadequate humidification of the membranes in these MEAs which increases the resistance to proton transport or high contact resistance between the cell components.

Table 6: Hydrogen crossover (mA/cm^2)

Cell	Initial	After 240h	After 480h
1	0.27	nd	nd
2	0.30	0.22	0.27
3	0.35	0.23	0.28
4	0.32	0.21	0.25
5	0.29	0.22	0.26
6	0.32	0.24	0.24
7	0.32	nd	0.23
8	0.20	0.33	nd
9	nd	0.21	0.23
10	0.22	0.25	0.28

Table 7: Pt concentration in the cathode effluent as a function of dynamic stress testing cycling

Hours of Cycling	Number of Cycles	Pt concentration in cathode effluent (ppb)
143	1407	14.8
186	1830	34.2
235	2311	18.0
240	2400	6.54
288	2833	4.20
327	3216	4.77
352	3462	2.55
403	3964	2.87
444	4367	5.95
471	4633	10.7
480	4721	28.5

The "IR-corrected" individual cell polarization curves are also shown in Figure 66 (bottom). These curves illustrate that a significant fraction of the voltage losses can be attributed to membrane resistance for all cells except 1, 9, and 10. With the exception of these three cells, after iR-correction the voltages of all cells fall within a 60 mV spread.

A plot of the iR-corrected cell voltages vs. the log of the current density should be linear with a slope of 70 mV/dec if the voltage losses are controlled by the kinetics of the oxygen reduction reaction [125]. Any deviation from this slope indicates that other factors, such as mass transfer in the electrodes, are influencing the voltage losses [128]. Comparison of the slopes of the experimentally-determined voltage-log current curves with the theoretically-expected slope shows that cells 1, 6, 8, and 9 deviate from the theoretical line at the lowest current densities,

which indicates that the performance of these cells is effected to a large extent by reactant concentration or limitations in mass transfer of reactants to the catalytic sites.

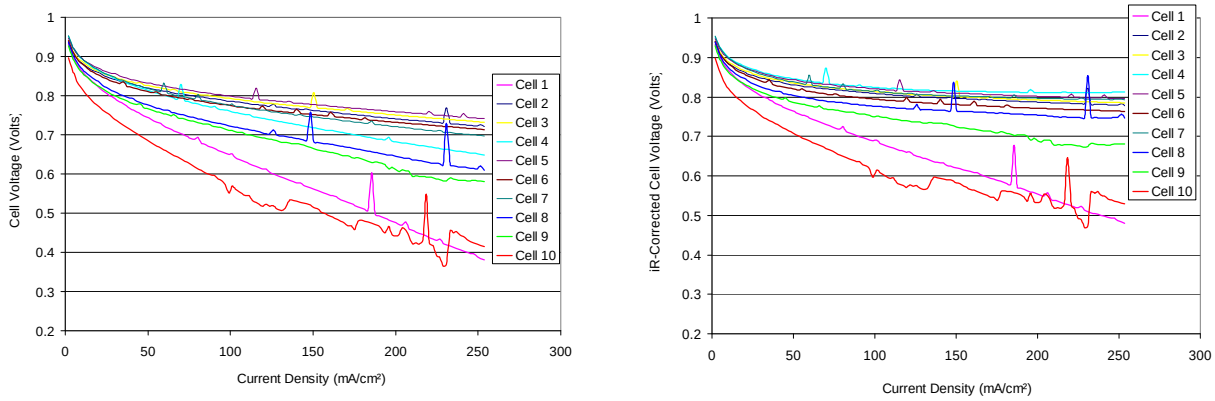

Figure 66: Initial individual cell voltages (top) and iR-corrected individual cell voltages as a function of stack current density. Conditions are the same as those for Figure65.

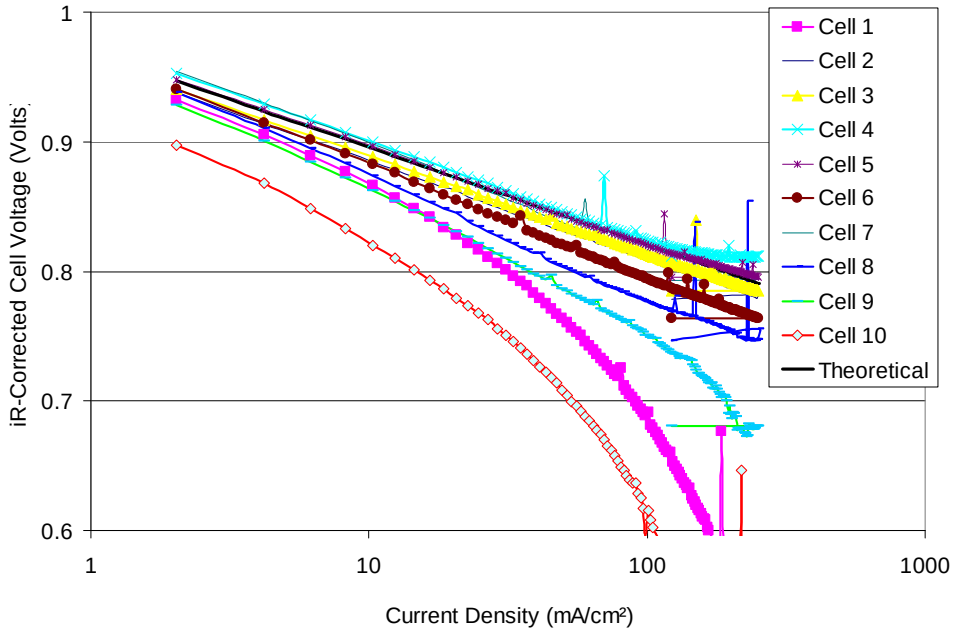

Figure 67: iR-corrected individual cell voltages as a function of the logarithm of stack current density. The black line shows the theoretical slope expected for a purely kinetically-controlled reaction. Conditions are the same as those for Fig. 65.

Figures 66 and 67 were used to determine the contribution of kinetics, mass transfer, and resistive sources (iR) to the overall cell and stack voltage loss at 100 mA/cm². The results of these analyses are summarized in Table 8. The "kinetic loss" shown in Table 8 is the difference between the voltage at 2 mA/cm² and the iR-corrected voltage expected at 100 mA/cm² using a linear fit to the voltage-log current density plot. These data illustrate the large contribution of

kinetic losses in all cells, of mass transport losses in the end cells, 1 and 10, and of the iR loss in cell 4 to the overall stack voltage loss.

Table 8: Cell losses and contribution to overall stack loss of 2.039 V at 100 mA/cm² (%)

Cell	Kinetic Loss (V)	iR Loss (V)	Mass Transport Loss (V)	Kinetic Loss (%)	iR Loss (%)	Mass Transport Loss (%)	Contribution To Stack Losses (%)
1	0.169	0.040	**0.072**	8.3	1.9	**3.5**	**13.8**
2	0.128	0.023	0.002	6.3	1.1	0.1	7.5
3	0.124	0.021	0.003	6.1	1.0	0.2	7.3
4	0.125	**0.065**	0.003	6.1	**3.2**	0.1	9.5
5	0.121	0.022	0.006	5.9	1.1	0.3	7.3
6	0.138	0.020	0.008	6.8	1.0	0.4	8.1
7	0.135	0.038	0.002	6.6	1.9	0.1	8.6
8	0.157	0.055	0.006	7.7	2.7	0.3	10.7
9	0.159	0.041	0.019	7.8	2.0	1.0	10.7
10	0.187	0.046	**0.103**	9.2	2.3	**5.1**	**16.5**

The stack was subjected to 240 hours (864,000 seconds) of the DOE-established dynamic stress test current profile shown in Figure 19. Representative voltage responses of the stack to cycles of this load profile are shown in Figure 68.

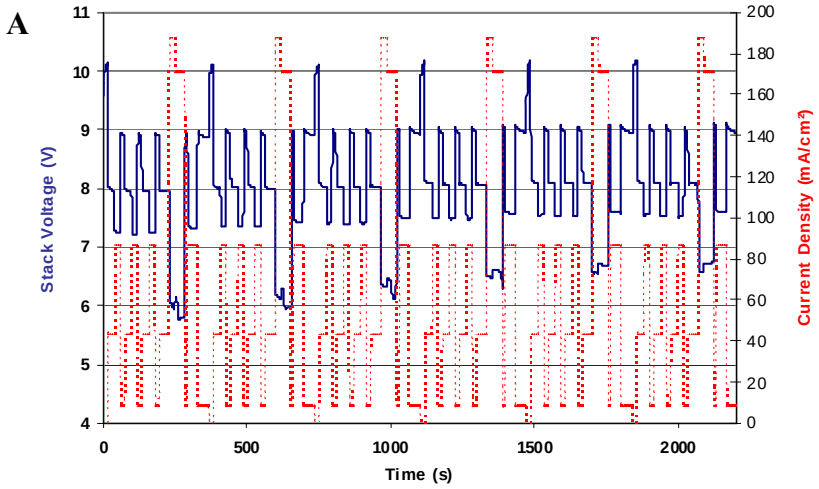

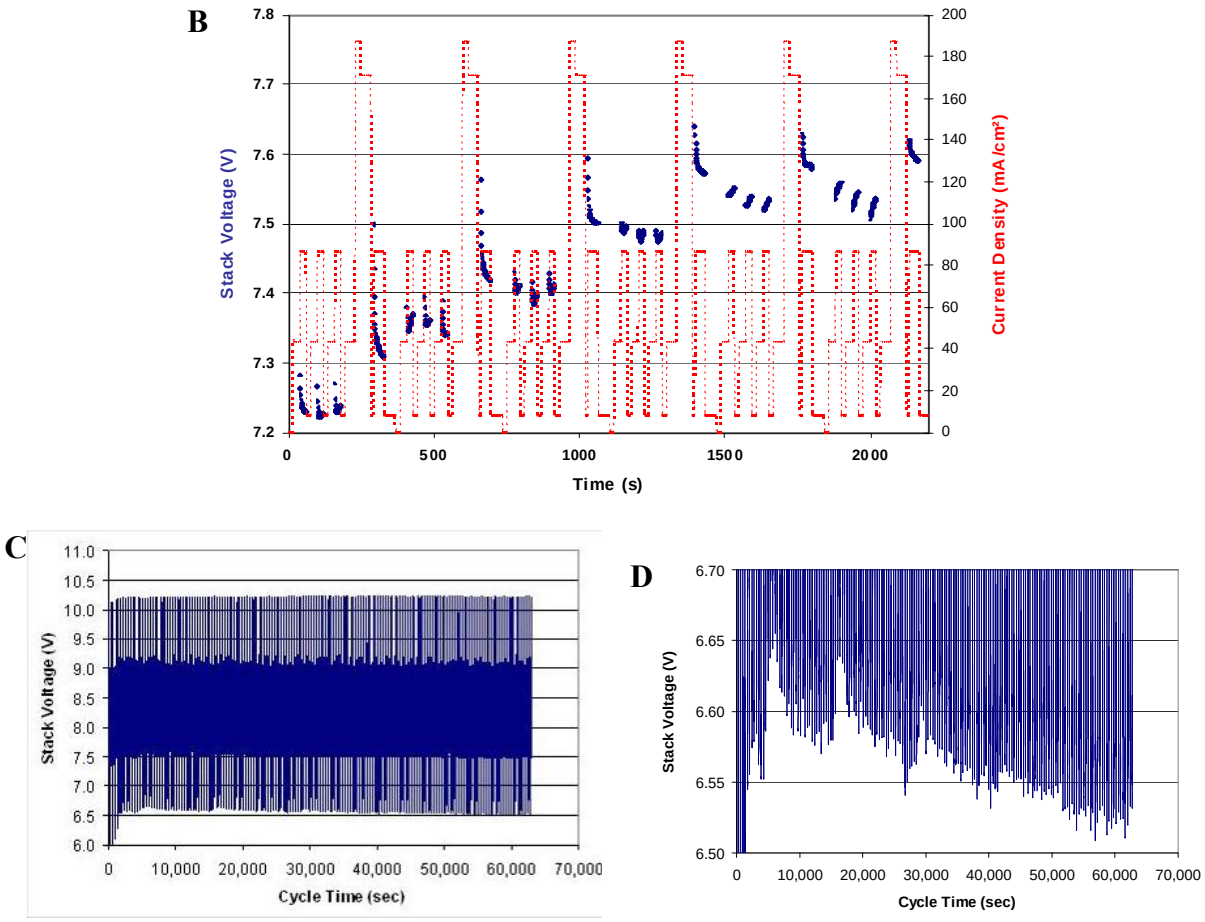

Figure 68: (A) Voltage response of the stack to five dynamic stress test cycles. (B) Magnification of the intermediate current steps in the dynamic stress test cycles illustrating performance increase with cycling. (C) Voltage response of stack to 70,000 seconds of dynamic stress testing. (D) Magnification of the high current region of the testing showing voltage degradation at >8,000 seconds.

These profiles show that the voltage response of the stack improved with cycling up to a cycle time of approximately 8,000 seconds, but degraded with further cycling (Figure 68 D). The response of the individual cells to the first 4,000 seconds of cycling is shown in Figure 69.

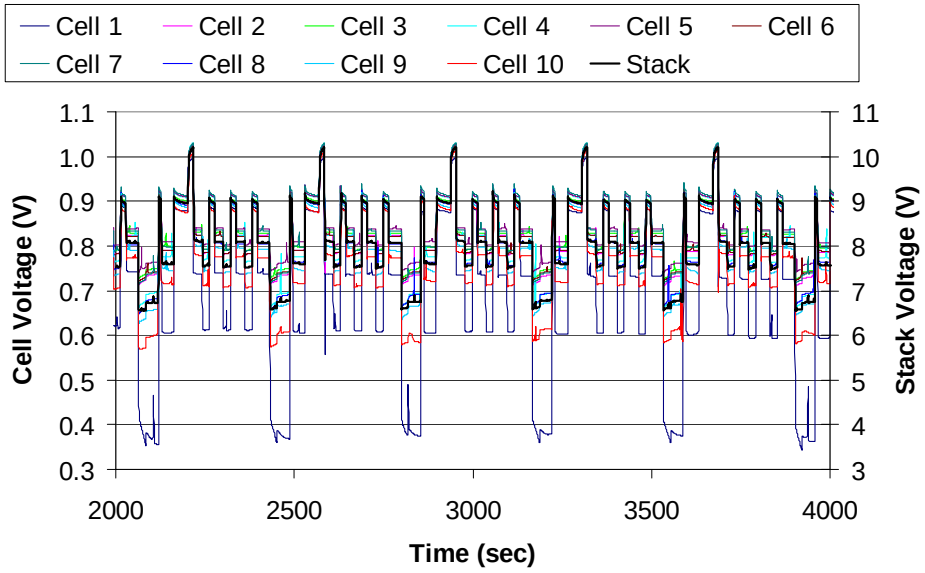

Figure 69: Response of the stack and individual cells and stack to the first 4,000 seconds of dynamic stress test cycling shown in Figure 19.

Following each 240 hours of load cycling, stack polarization curves were taken using the same conditions as those used for the initial polarization curve. As shown in Figure 70, the performance of the stack improved after the first 240 hours, indicating the stack had not reached its maximum performance during the prior stack conditioning treatment. The high frequency resistance of the stack, measured using the current interrupt technique, increased from a cell average of 264 mΩ-cm² to 295 mΩ-cm² after 240 hours. Therefore, the improvement in performance cannot be attributed to lowering of the high frequency resistance and lowering of the stack iR losses.

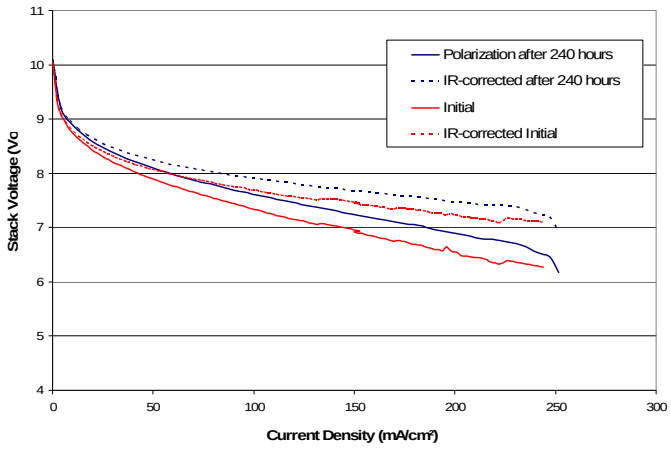

Figure 70: Polarization curves for the stack: Initial performance and performance after 240 hours of dynamic stress testing.

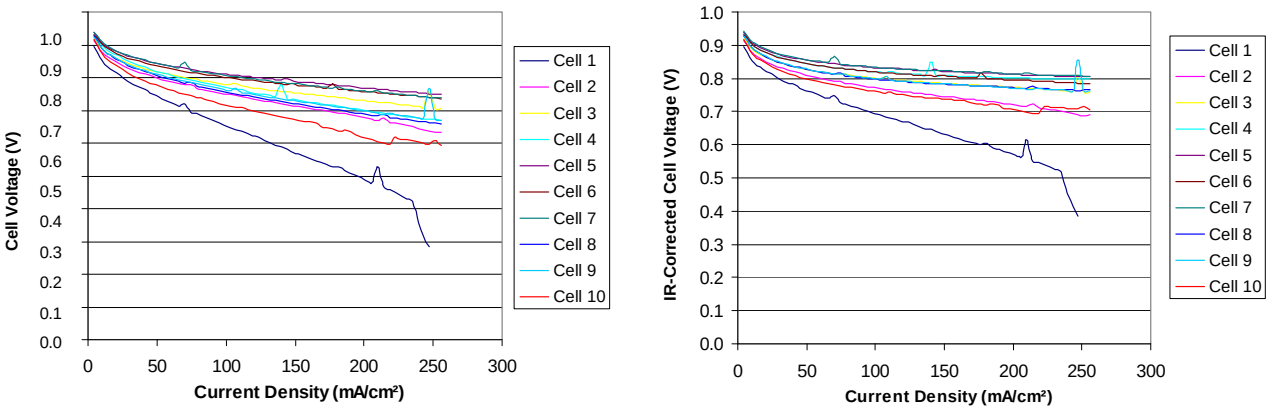

Figure 71: Individual cell voltages (left) and iR-corrected individual cell voltages as a function of stack current density after 240 hours of dynamic stress testing. Conditions are the same as those for Figure 65.

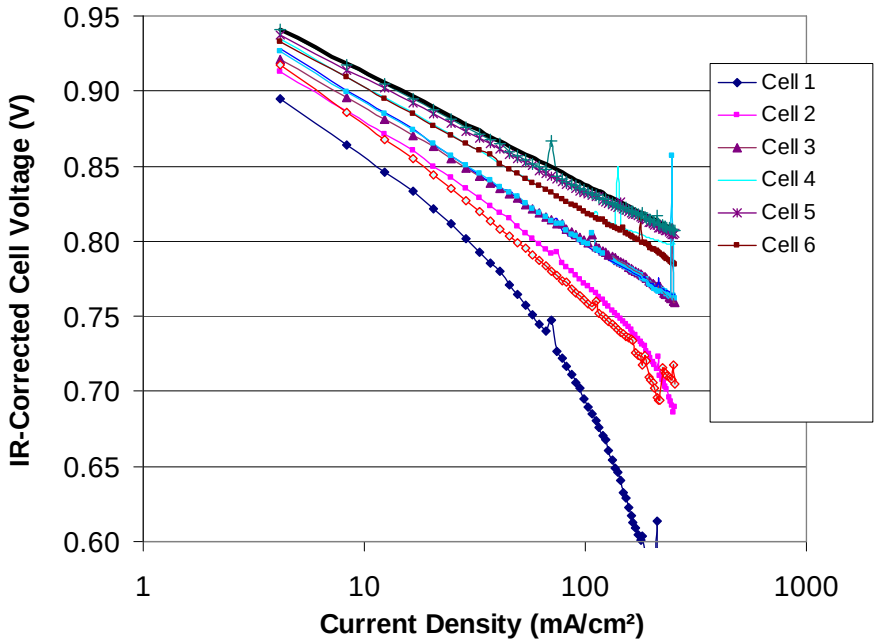

Figure 72: iR-corrected individual cell voltages as a function of the logarithm of stack current density after 240 hours of dynamic stress testing. The lack line shows the theoretical slope expected for a purely kinetically-controlled reaction. Conditions are the same as those for Figure 65.

Table 9 summarizes the losses due to kinetics, mass transfer, and iR obtained through analysis of Figures 71 and 72 and from cell diagnostic measurements. This table shows that by far the greatest improvement between the initial polarization curve and the polarization curve after 240 hours of dynamic stress testing is in cell kinetic losses, accounting for 73% of the 392 mV increase in stack voltage at 100 mA/cm². This is despite the general trend of loss in cathode electrocatalyst electrochemically-active surface area observed after 240 hours of cycling (see Table 5). This implies that the remaining surface area is more active on a surface area-

normalized basis than the initial catalyst. Such an effect may be explained by cycling causing Pt particle growth and by the well-established increase in area specific oxygen reduction reaction activity and lower mass normalized electrochemically-active surface with increasing Pt particle size [128].

Table 9: Cell losses at 100 mA/cm² (V) and contribution to overall stack loss of 1.655 V at 100 mA/cm² (%) after 240 hours of dynamic stress testing

Cell	Kinetic Loss (V)	iR Loss (V)	Mass Transport Loss (V)	Kinetic Loss (%)	iR Loss (%)	Mass Transport Loss (%)	Cell Contribution To Stack Losses (%)
1	0.143	0.042	0.060	8.6	2.5	3.7	**14.8**
2	0.125	0.022	0.017	7.6	1.3	1.1	9.9
3	0.118	0.022	0.003	7.1	1.3	0.2	8.6
4	0.110	0.052	0.003	6.7	3.2	0.2	10.0
5	0.105	0.022	0.000	6.4	1.4	0.0	7.7
6	0.097	0.020	0.017	5.9	1.2	1.0	8.1
7	0.103	0.028	0.004	6.2	1.7	0.3	8.2
8	0.124	0.043	0.006	7.5	2.6	0.4	10.5
9	0.121	0.037	0.007	7.3	2.3	0.4	10.0
10	0.145	0.046	0.012	8.7	2.8	0.7	**12.2**

As shown in Figure 73, degradation in stack performance was evident between 240 and 480 hrs of dynamic stress testing. Diagnostics were performed on each cell in the stack, as described in the appendix, to determine the sources of the changes in stack performance resulting from the test protocol. These diagnostics were determination of the electrochemically-active surface area of the cathode electrocatalyst, hydrogen crossover rates through the membrane, and resistive losses (high frequency resistance).

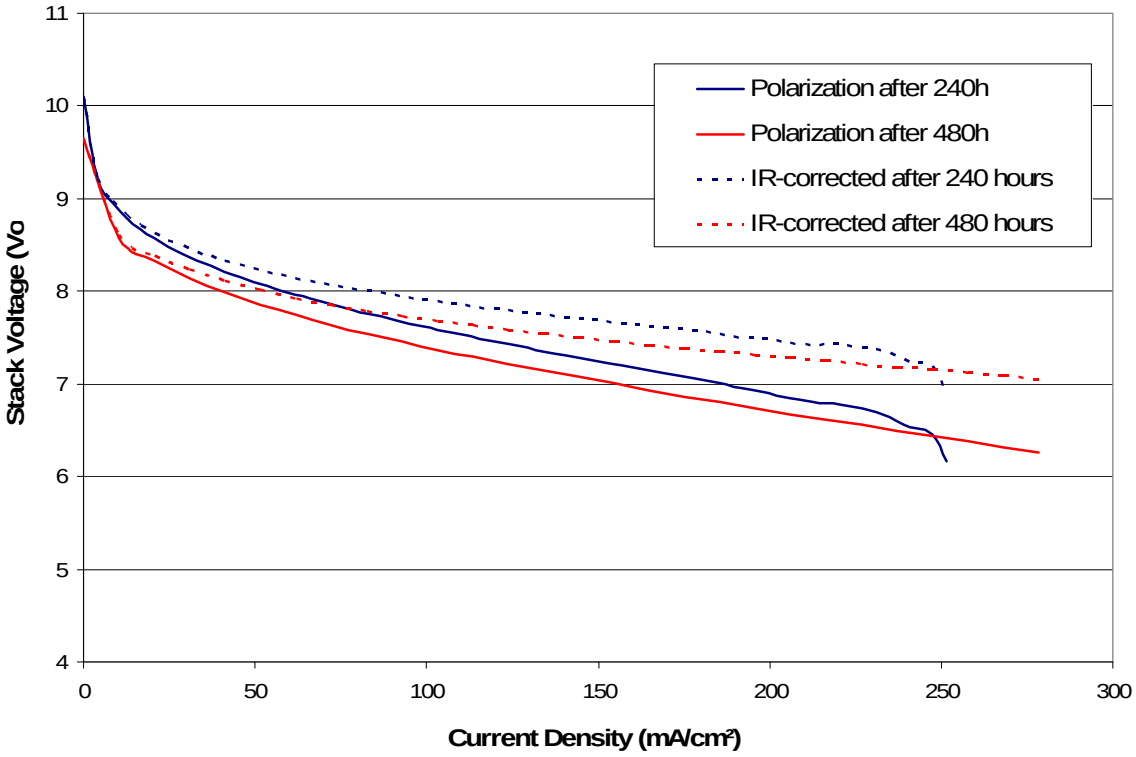

Figure 73: Polarization curves for the stack: Performance after 240 and 480 hours of dynamic stress testing.

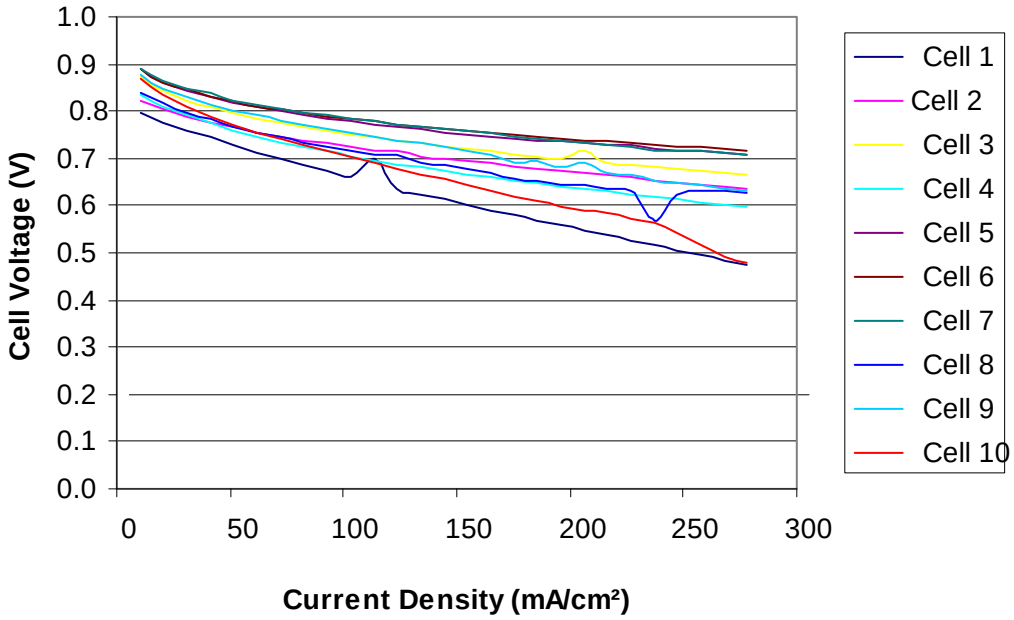

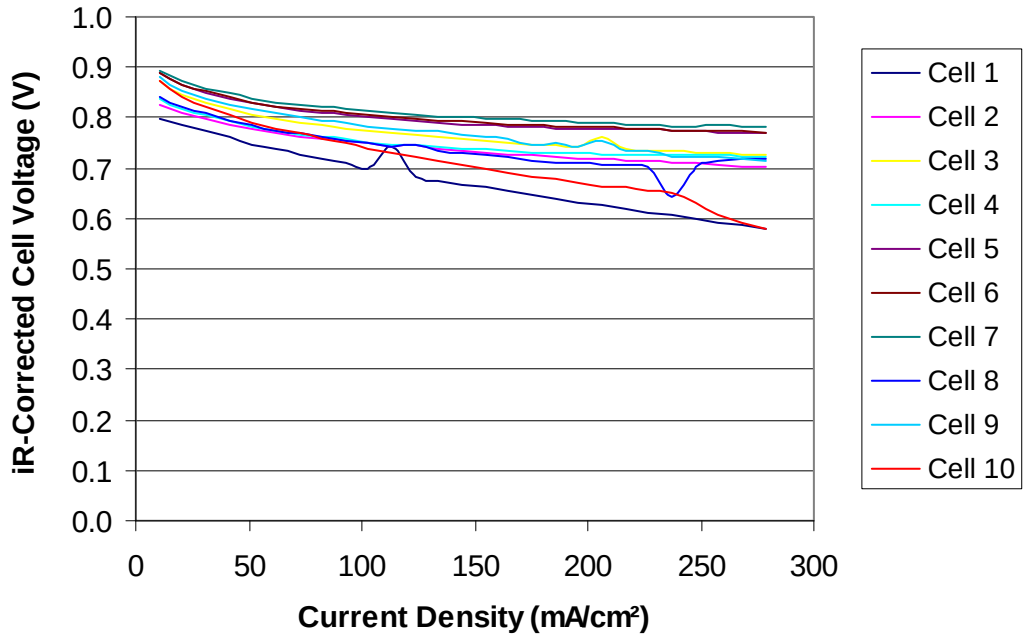

Figure 74. Individual cell voltages (top) and iR-corrected individual cell voltages as a function of stack current density after 480 hours of dynamic stress testing. Conditions are the same as those for Figure 65.

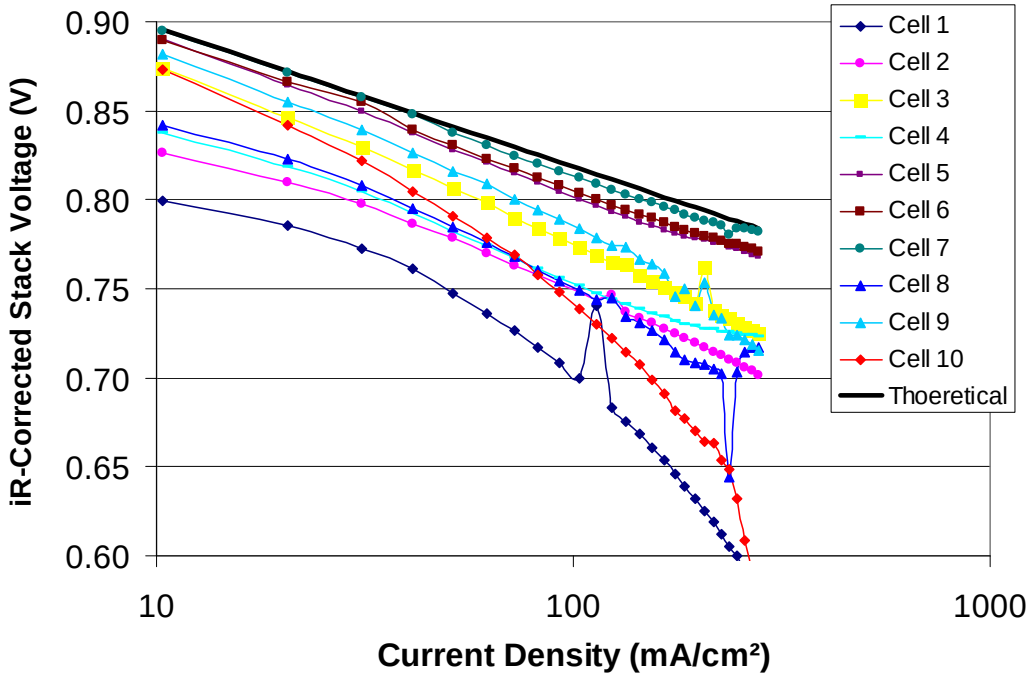

Figure 75: iR-corrected individual cell voltages as a function of the logarithm of stack current density after 480 hours of dynamic stress testing. The black line shows the theoretical slope expected for a purely kinetically-controlled reaction. Conditions are the same as those for Figure 65.

These results of the diagnostic tests after 480 hours of cycling are summarized in Tables 4–7. Table 10 summarizes the losses due to kinetics, mass transfer, and iR obtained through analysis of Figures 74 and 75, and from the cell diagnostic measurements. As illustrated in this table, the high frequency resistance of the stack decreases between 240 hours and 480 hours of dynamic stress testing and thus the iR loss decreases from 335 mV to 300 mV. The losses due to mass transfer also decrease from 252 mV to 134 mV. The over-potential or kinetic losses between open circuit and 100 mA/cm² decrease. However, the cumulative 387 mV improvement in performance is offset by a 700 mV loss in open circuit potential, for a net loss in stack performance of 313 mV. Comparison of the hydrogen crossover rates of Table A3 show that the decrease in open circuit voltage cannot be attributed to increases in hydrogen crossover rates. Therefore, the open circuit losses are most likely associated with loss of the electrochemically-active surface area of the cathode electro-catalyst, an average of 42% loss (Table 5). The loss in electrochemically-active surface area results in a 70 mV loss for every order of magnitude decrease in surface area attributable to the cathode reaction and also a loss due greater polarization due to decreased surface area to oxidize crossover hydrogen [124].

Table 10: Cell losses at 100 mA/cm² (V) and contribution to overall stack loss of 1.291 V at 100 mA/cm² (%) after 480 hours of dynamic stress testing

Cell	Kinetic Loss (V)	iR Loss (V)	Mass Transport Loss (V)	Kinetic Loss (%)	iR Loss (%)	Mass Transport Loss (%)	Cell Contribution to Stack Losses (%)
1	0.052	0.039	0.044	4.2	3.2	3.6	11.1
2	0.064	0.024	0.012	5.2	2.0	1.0	8.2
3	0.094	0.023	0.004	7.7	1.9	0.3	9.9
4	0.063	0.047	0.018	5.2	3.8	1.4	10.4
5	0.085	0.023	0.003	6.9	1.9	0.3	9.1
6	0.072	0.020	0.012	5.9	1.7	1.0	8.5
7	0.074	0.027	0.005	6.1	2.2	0.4	8.8
8	0.065	0.033	0.024	5.4	2.7	1.9	10.0
9	0.088	0.031	0.008	7.2	2.6	0.6	10.4
10	0.101	0.037	0.030	8.3	3.1	2.4	13.7

Immediately following 480 hours of dynamic stress testing, one cell in the stack lost all voltage. The tests were terminated at this time and the stack disassembled for the post-mortem diagnostics.

Post-mortem diagnostic results

Post-mortem visual and optical microscopic examination of all the MEAs in the stack revealed that significant degradation of the anode and cathode gaskets occurred on all MEAs. Representative photographs of MEA 5 are shown in Figure 76. As this photograph clearly shows, gasket degradation was particularly severe near the gas outlets even to the point of failure of the gaskets to prevent hydrogen from entering the cathode chamber and/or the anode chamber.

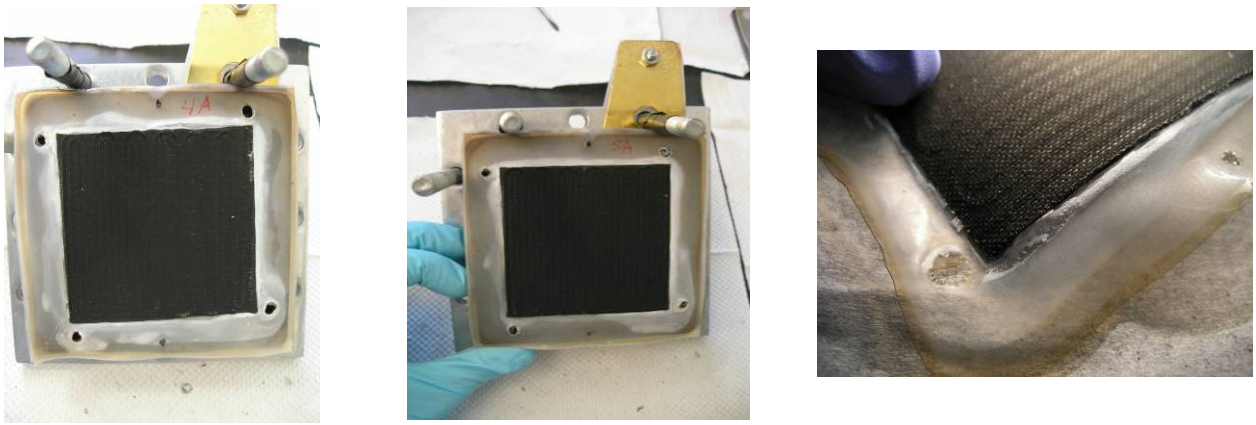

Figure 76: Post-mortem photographs of MEA 4 (left) and MEA 5 (middle and right) showing seal degradation.

Scanning electron microscopic evaluation with energy dispersive X-ray analysis was performed on three MEAs (1, 5, and 7). These cells represent cells at the stack inlet (1), the cell that failed (5), and a well-performing cell (7). The micrographs are shown in Figures 77 and 78. This analysis showed that there were no major differences between the three cells. The following observations were made upon analysis of the micrographs. The Nafion membrane is approximately 150 micrometers thick and the anode and cathode layers were not of uniform thickness within one cell. The thicknesses of the electrode layers ranged from 10 to 45 micrometers and were thinner where they made contact with the gas diffusion layer. Individual particles of platinum could not be resolved, but Pt clusters were observed in the cathode of MEA #1. The ionomer in the electrode layers is well mixed with the Pt/C and the Pt/C is uniformly dispersed throughout the thickness of the electrodes. Systematic thinning of the cathode compared to the anode was not observed, which argues against cell degradation due to carbon support oxidation on the cathode caused by high potentials encountered on this electrode. The bonding between the electrodes and membrane was weak and separation between these layers was observed.

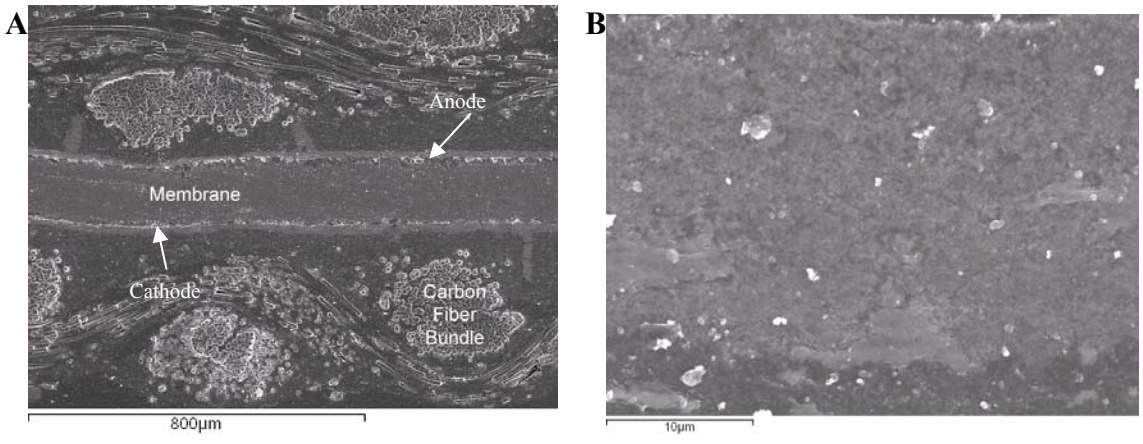

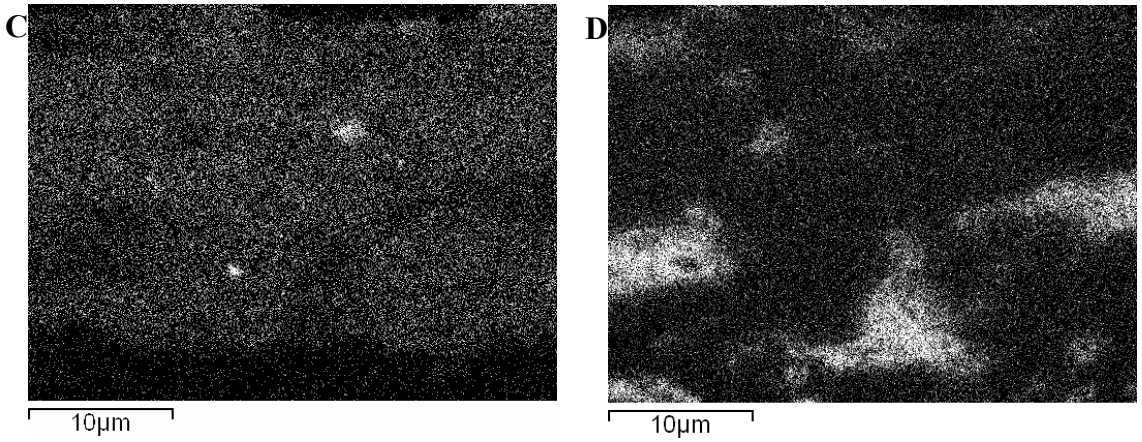

Figure 77: MEA #1: (A) SEM image of a cross-section, (B) SEM image of a section of the cathode layer (a small swath of the GDL is at the bottom of the image), (C) EDX map of F in the cathode layer of the SEM image in (B) showing where the Nafion is located. (D) EDS map of Pt in the cathode layer in (B).

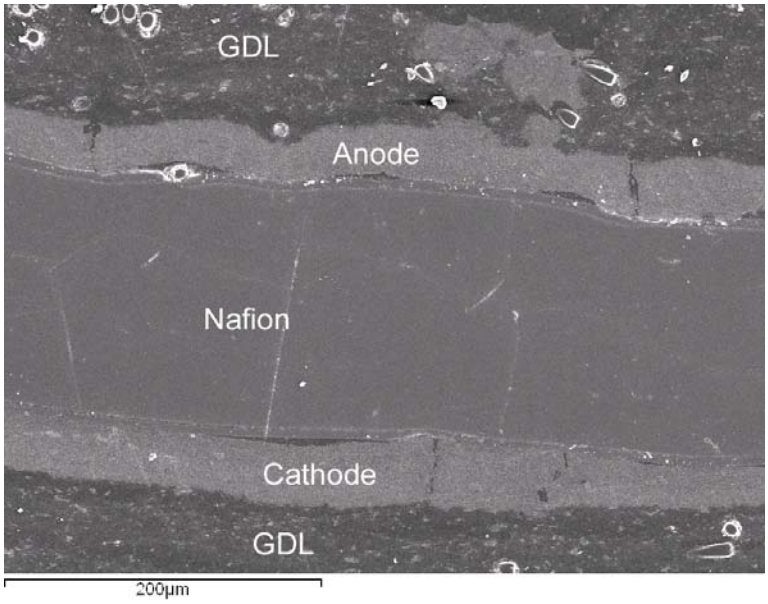

(A)

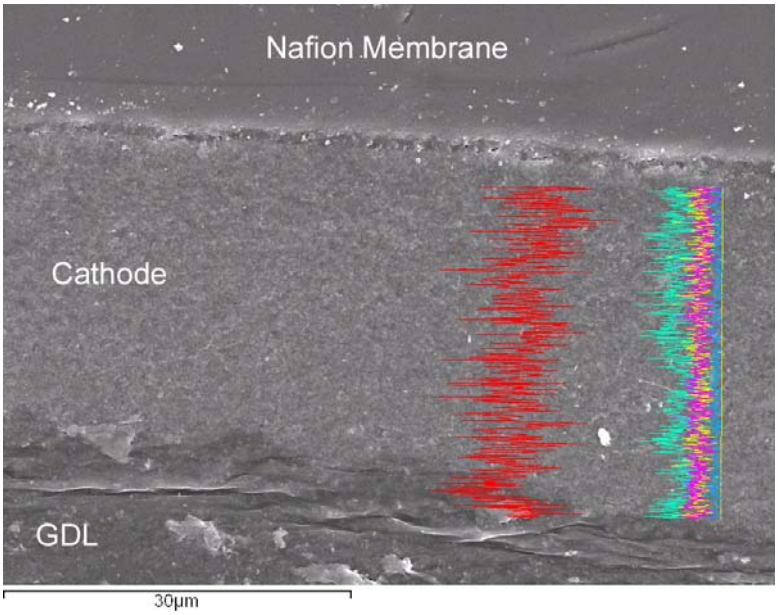

(B)_

Figure 78: (A) SEM image of a cross-section of MEA #5 and (B) SEM image of the cathode of MEA #7 with an EDX line scan superimposed. The line scan was made by scanning the electron beam from the top of the straight yellow line to the bottom of it. (Red line = carbon, green line = fluorine, pink line = platinum).

Post-mortem X-ray diffraction analysis of the cathode and anode catalyst layers of MEA #4 showed that the Pt particles on the cathode have an average size of 6.2 nm and on the anode, 5.3 nm. With a 5.3 nm particle, the theoretical electrochemically-active surface are of the platinum nano-particles is 52.9 m^2/g, whereas the average measured value is 20.8 m^2/g. Therefore, the average catalyst utilization is only 39%. With 6.2 nm particles, the theoretical electrochemically-active surface area is 45.2 m^2/g, whereas MEA #4 only had a measured value of 9.4 m^2/g. Therefore, utilization had dropped to 21% for this MEA.

Chapter 3 Results and Discussion Continued…

Chapter 3 Results and Discussion Continued… 95
Fuel Cell Vehicle Transient Power 95
Energy Storage Requirements 95
Driving cycle study 97
Power Flow Determination: 99
Motor Control Method 99
Cathode Catalyst Development for Solid Oxide Fuel Cell 100
Thermodynamic and Kinetic Stability of $La_{1-x}Sr_xMnO_{3-d}$ Perovskites 100
Determination of LSM Chemical Compatibility with the Y-ZrO_2 Electrolyte 102
Determination of LSM Mechanical Compatibility with the Y-ZrO_2 Electrolyte 103
Measurements of Conductivity and Area Specific Resistance 104

Fuel Cell Vehicle Transient Power

Energy Storage Requirements

The size of energy storage units for various vehicles with different driving profiles was calculated. Calculations were done using the acceleration method and the two driving cycle methods.

Acceleration method: In this method a comparison was made between the constant force and constant acceleration profiles. The comparison was done on a midsized sports utility vehicle (SUV) with parameters as shown in Table 11.

Table 11: Mid-Size SUV Characteristics

Mass of vehicle	2350 kg
Coefficient of air drag	0.44
Acceleration due to gravity	9.8 m/ second square
Frontal area of the vehicle	2.66 square meters
Air density	1.24 kg/cubic meter
Coefficient of rolling resistance	0.012
Final velocity at end of time period	60 miles per hour
Time to accelerate to final velocity	10 seconds
Grade of the road	0

In the comparison the fuel cell was considered to be set at the value needed to maintain a constant cruising speed. The energy storage requirements for the battery and supercapacitor were calculated to supplement the fuel cell during acceleration. For both the constant power and

constant force cases, the values for power and energy required to be delivered by the energy storage elements are calculated.

For the constant force case, the peak power is obtained from the product of force and peak velocity at the end of the interval. The energy is the integral of this power over the time period.

In the constant power case, as the name suggests, the power is constant and the energy is the product of the power and total time. The fuel cell is assumed to provide increasing power from 0 to 70 kilowatts in a linear fashion for the first two seconds. This is to approximate the two-second time delay associated with the fuel cell. After the rated power of 70kW is reached, the fuel cell power is kept constant.

For both cases the power and energy requirements from ESUs are obtained by subtracting the power and energy values of the fuel cell from the total requirements. The energy and power requirements from the energy storage elements were found to be 144.45 watt hours and 115 kilowatts, respectively, for the constant power case and 137.5 watt hours and 155 kilowatts for the constant force case.

The calculate power and energy requirements are then divided between the battery and supercapacitor. The battery and supercapacitor energy storage and power requirements were found in terms of their masses. This is based on the specific power and specific energy of each component. These values can vary of a considerable range making it necessary to look at a wide range of possible values. The range of values for these quantities used in this study is shown in Table 12 [129].

Table 12: Battery vs. Ultracapacitor Performance

Performance	Battery	Ultracapacitor
Specific Energy (storage)	10-100 —W-h/kg	5-10 W-h/kg
Specific power (delivery)	< 1000W/kg	<10,000 W/kg
Charge/discharge efficiency	50-85%	85-98%
Life expectancy	3 years	10 years

To investigate the affect of the change in variables the specific energy and specific power of the battery and the ultracapacitor were each changed independently. This developed four different ranges of battery and capacitor masses for the each of the constant power and force cases. When one of the variables was varied the others were kept constant at their average value. The average values assumed are 600 watts/kg for specific power of the battery, 3500 watts/kg for specific power of the ultracapacitor, 100 watt hr/kg for specific energy of the battery, and 4 watt hr/kg for specific energy of the capacitor.

The different values are tabulated separately for the two cases of constant force and constant torque in Tables 13 and 14. The corresponding calculations can be found in [130].

Table 13: Trends of Battery and Capacitor Masses for Constant Force Case

Variable	Range	Battery Weight (kg)	Ultracapacitor Weight (kg)

Specific power of battery (wt/kg)	50 - 1300	0	44.3 – 44.45
Specific power of ultracapacitor (watt/kg)	3000 - 4000	0	52 - 39
Specific energy of battery (watt hr/kg)	25 - 200	0 – 0.8	44.55 – 44.32
Specific energy of ultracapacitor (watt hr/kg)	3 - 4	0.08 – 0	44.28 – 44.36

Table 14: Trends of Battery and Capacitor Masses for Constant Power Case

Variable	Range	Battery Weight (kg)	Ultracapacitor Weight (kg)
Specific power of battery (wt/kg)	50 – 1300	0.131 – 0.133	32.85 – 32.81
Specific power of ultracapacitor (watt/kg)	3000 - 4000	0 – 0.3	39 - 29
Specific energy of battery (watt hr/kg)	25 – 200	0.55 – 0.05	32.76 – 32.84
Specific energy of ultracapacitor (watt hr/kg)	3 – 4	0.48 – 0.18	32.775 – 32.825

It can be seen from the above tables that the ultracapacitor takes up the major part of the energy storage system. The values obtained do not differ much from each other. It was observed only that the battery weight is a little higher for the constant power case and ultracapacitor weights higher for the constant force case.

Driving cycle study

For this study a midsize vehicle for each of the two studies discussed. This vehicle required a minimum of 114.05 kWh total energy, 120.86 kW peak power, and 23.2 KW average powers.

As discussed above, two methods were used to determine the desired results. Method 1 minimized an objective function consisting of a weighted combination of component mass, volume, and cost. This method constrained the system by requiring minimum total energy storage, peak power, and cruising power. Method 2 maximized an objective function consisting of a weighted combination of energy storage, peak power, and cruising power. For this method, the system was constrained to a maximum volume, mass, and cost. In both of these methods solutions are obtained using the linear programming Simplex algorithm. Also in both of the methods the variables being manipulated are the masses of the battery, capacitor, hydrogen, and fuel cell.

The parameters used in the optimization for Method 1 discussed are as follows:

NIMH Battery:

specific energy: 55Wh/kg.
specific power: 1000W/kg
cost/kg: 40$/kg.
volume/kg: 0.5L/kg.

Supercapacitor:

specific power: 3500W/kg
cost/kg (including packaging): 134.5$/kg
volume/kg: 0.78L/kg

Fuel Cell:

power: $P_{fc} = (0.333M_{fc} - 24.333) * 1000W$
cost/kg: 17.55 $/kg

volume/kg: 1 L/kg

Hydrogen:

specific energy: 1500Wh/kg
cost/kg: 9$/kg
volume/kg: 1.25 L/kg

The fuel cell mass was determined based on meeting the average power requirement. The values determined by this Method 1 are shown in Table 15.

Table 15: Example design results using Method 1

System Mass	
NIMH Battery (kg)	24.1
Supercapacitor (kg)	24
Hydrogen (kg)	90
Fuel cell (kg)	217
Vehicle Duty Cycle	
Energy (KW.h)	136.3
Peak Power (KW)	156
Average Power (KW)	72.1
Energy System:	
Mass (kg)	355.1
Cost ($)	8810
Volume (L)	355.8

Using the same components for Method 2 it was found that no results were obtainable because of the high cost of nickel-metal hydride batteries. Using lead-acid batteries, however, it was possible to obtain a solution.

The parameters used for the lead acid battery are as follows:

Specific energy, energy/mass: 35Wh/kg.
Specific power, power/mass: 550W/kg
Specific cost, cost/mass: 5.5$/kg
Specific volume, volume/mass: 0.38L/kg

Again the fuel cell mass was determined to meet the average power command. With this value set the resultant values from Method 2 are shown in Table 16.

Table 16: Example design results using Method 2

System Mass	
Lead-Acid Battery (kg)	341
Supercapacitor (kg)	87.6
Hydrogen (kg)	376.4
Fuel cell (kg)	145
Vehicle Duty Cycle	
Energy (KW.h)	580
Peak Power (KW)	540
Average Power (KW)	230

Power Flow Determination:

Simulations were done to determine the effectiveness of the power flow optimization methods discussion. This method determined power command for the various ESUs used in the vehicle.

Simulation for various driving cycles was run to show that the battery was able to maintain a proper charge throughout the driving period. The battery state of charge for an example run during a US06 highway driving cycle is shown in Figure 79. The top graph is the required output power at the battery side. The second graph shows the real power supplied by the battery. The difference between the two graphs is due to losses in the battery. The last graph shows the variation of battery SOC. As this example considered a plug-in hybrid, the battery started fully charged. Throughout the driving cycle the battery was able to maintain the battery charge within the acceptable range, between 40% and 80%. Details of other driving cycles can be found in [131].

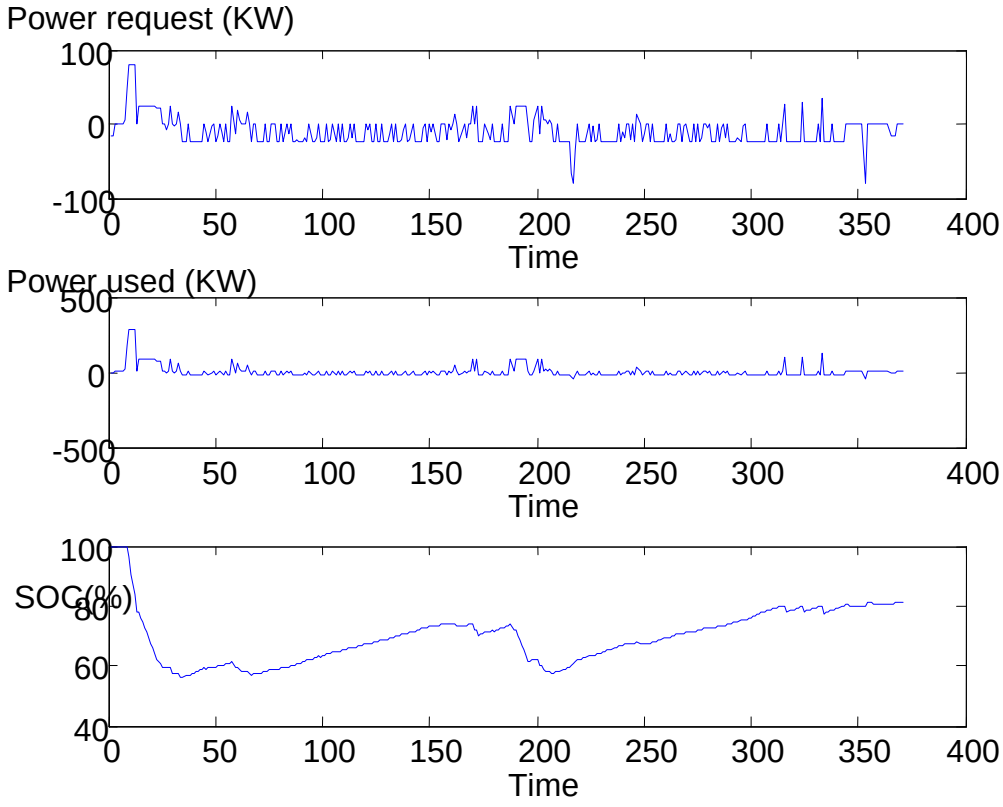

Figure79: Battery performance during US06 highway driving cycle.

Motor Control Method

The proposed motor control method using slip control was tested using a small scale system. A ¼ Hp motor connected to a standard variable voltage variable frequency converter was used in this study. A standard 8 bit microcontroller was used as the control command.

Testing the slip control dynamic performance consisted of sending a step slip commands to the inverter and measuring the resulting speed. The step in slip command should approximately give a step in torque resulting in a ramp of speed. The experimental results are displayed in Figure

80. The bottom trace represents the slip command while the top trace represents the speed. It is apparent that the speed ramps up and down with the slip command as expected demonstrating the principle of operation.

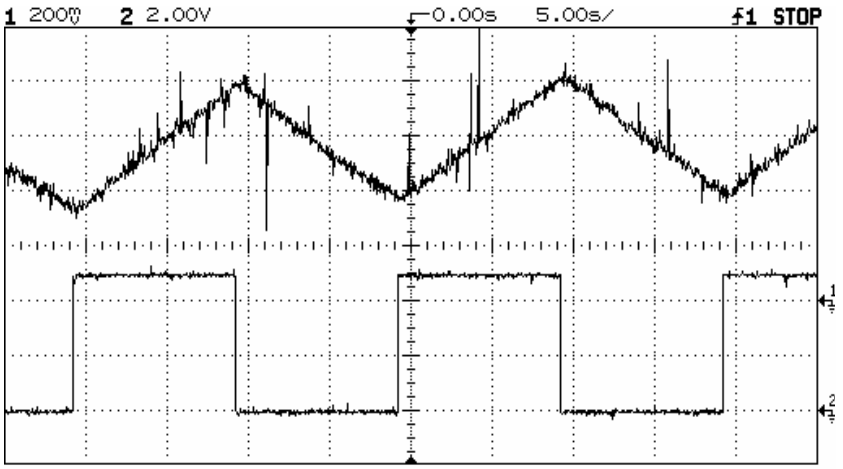

Figure 80: Experimental waveforms from slip control test. Top trace represents speed. Bottom trace represents slip command.

Cathode Catalyst Development for Solid Oxide Fuel Cell

Assessment of capabilities and development of $La_{1-x}Sr_xMnO_3$ (LSM, $x > 0.5$) cathodes for fuel cells based on yttrium stabilized ZrO_2 electrolyte**:**

Thermodynamic and Kinetic Stability of $La_{1-x}Sr_xMnO_{3-d}$ Perovskites

It was established by using thermogravimetry that compositions $x = 0.5 - 1$ are stable in O_2, argon, 0.3% H_2/Ar, and CO/CO_2 to 750 ^oC, i.e. within the planned temperature range for applications (Figure 81). In addition, it was found that compositions $x < 0.9$ are stable in O_2 and argon to 1400^oC.

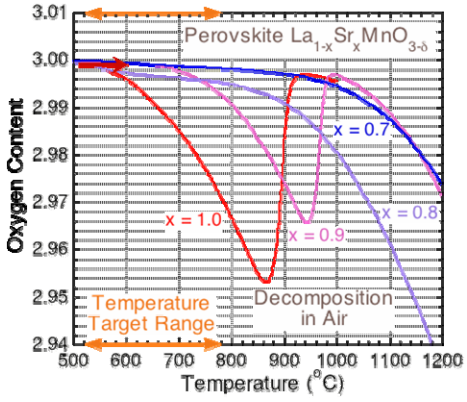

Figure 81: Thermogravimetric study of La1-xSrxMnO3 stability in air.

Complex phase equilibria have been revealed for $La_{1-x}Sr_xMnO_3$ cathodes by "in situ" neutron powder diffraction measurements as a function of oxygen pressure, temperature, and time

(Figure 82). Preliminary phase diagrams of the system have been derived as a function of temperature and oxygen content (Figures 83 and 84). A new homologous series of oxygen-vacancy-ordered perovskites with the formula $Sr_{4+n}Mn^{3+}{}_4Mn^{4+}{}_nO_{10+3n}$ has been discovered (Figure 25). These compounds correspond to n=0 ($SrMn^{3+}O_{2.5}$), n=1 ($Sr_5Mn^{3+}{}_4Mn^{4+}O_{13}$) and n=3 ($Sr_7Mn^{3+}{}_4Mn^{4+}{}_3O_{19}$) members of the series. A linear set of four $Mn^{3+}O5$ pyramids defines the n=0 building block for the series. The n-th members can be constructed from blocks containing four pyramids and n $Mn^{4+}O6$ octahedra with 2/m symmetry.

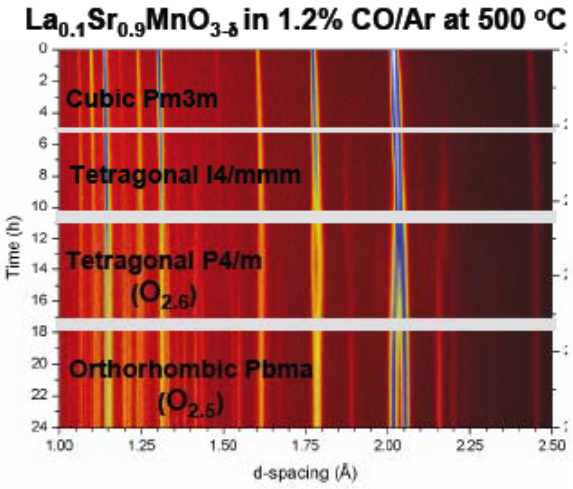

Figure 82: An example of the "in situ" NPD diffraction patterns.

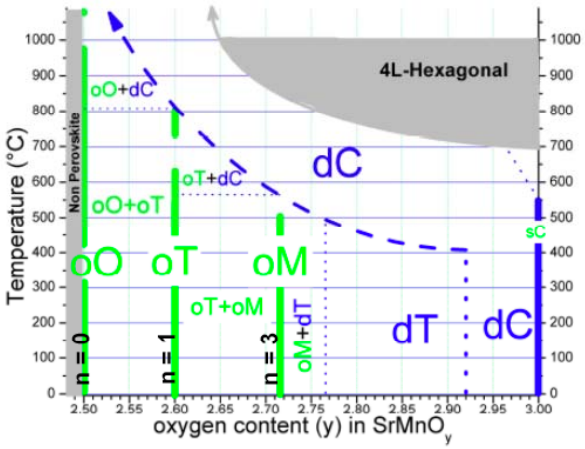

Figure 83: Stability of oxygen ordered phases as a function of oxygen content and temperature for $SrMnO_{3-y}$.

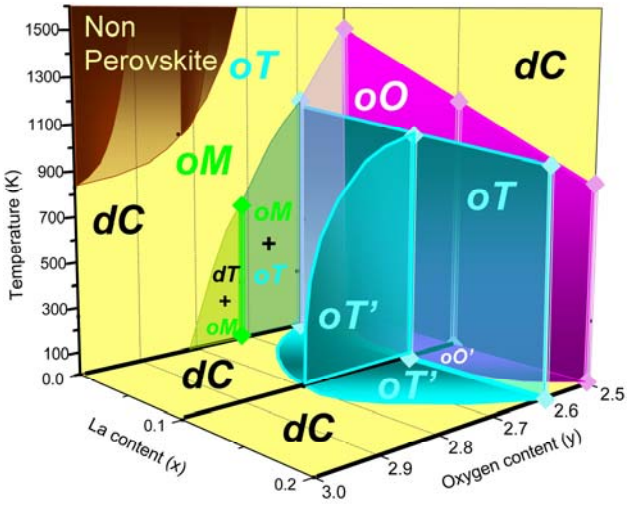

Figure 84: Stability of oxygen ordered phases as a function of oxygen content and temperature for La1-xSrxMnO3.

The compositional ranges of stability of various oxygen vacancy ordered phases that are detrimental for MIEC are shown on Figure 85. It is observed that a wide range of oxygen vacancy phases, which are not ordered (i.e., are beneficial for MIEC) exists on the diagram for x = 0.6 – 0.9 and d = 0 – 0.3.

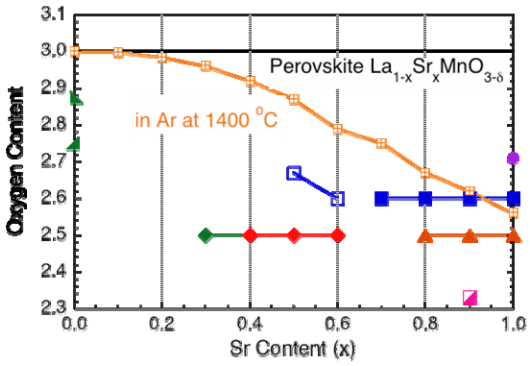

Figure 85: Stability ranges of various oxygen ordered phases as a function of chemical composition and oxygen content for La1-xSrxMnO3-d.

Determination of LSM Chemical Compatibility with the Y-ZrO_2 Electrolyte

Temporal stability of the cathode-electrolyte interface has been studied by heating 1:1 (weight) mixtures of $La_{1-x}Sr_xMnO_3$ and YSZ (3% and 8% Y) for x = 0.2, 0.5, 0.7, and 0.9 in the form of pressed pellets at 1000 °C in air. Stability has been confirmed for x = 0.2 and observed for first time for 0.5 up to 84 h. Phase transformation of the electrolyte YSZ was observed for x = 0.7 after 24 h. Experiments showed that structural transformations of the YSZ (3% Y) electrolyte were the main effects of heating in air at 1000 °C. In addition, small amounts of decomposition of the LSM material were observed for x=0.7 after firing for 180 hours. This was visible as a low-intensity diffraction peak of the deleterious $SrZrO_3$ phase in the diffraction patterns (Figure 86). Long-term stability has been confirmed for the LSM with x=0.2 and 0.5 by the absence of $SrZrO_3$ phase and the constancy of the weight ratio of 1:1 for the LSM and ZrO_2 phases by using the Rietveld refinement method.

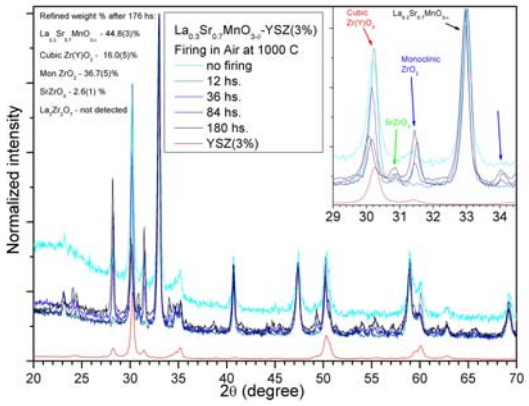

Figure 86: Study of chemical stability of La1-xSrxMnO3 and YSZ (3% Y) up to 1000°C.

Determination of LSM Mechanical Compatibility with the Y-ZrO_2 Electrolyte

Materials expansion measurements were performed as a function of temperature and oxygen content. Figure 87 shows exemplary measurement in Ar and oxygen for $SrMnO_{2.6}$. Large thermal end chemical expansion coefficients (although smaller than measured for the best $(La,Sr)(Fe,Co)O_{3-d}$ cathodes) were found for highly Sr substituted materials that are not compatible with any of the currently known electrolytes (Figure 88).

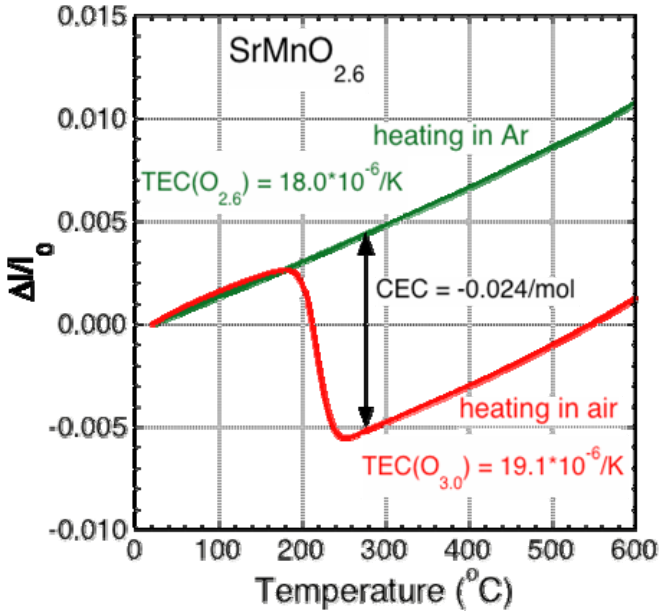

Figure 87: Thermal end chemical expansion for $SrMnO_{2.6}$

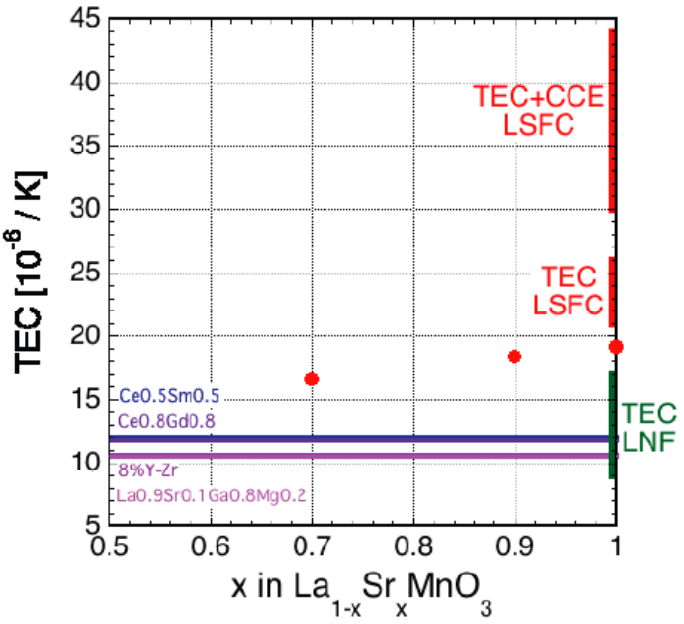

Figure 88: Comparison of thermal expansion coefficients (TEC) of $La_{1-x}Sr_xMnO_3$, $(La,Sr)(Fe,Co)O_{3-d}$ and $La(Ni,Fe)O_3$ with currently used electrolytes.

Measurements of Conductivity and Area Specific Resistance

All LSM compositions except $SrMnO_3$ showed metallic conductivity above 200°C (Figure 89). Compositions $x \geq 0.5$ revealed 2 – 3 times lower area specific resistance in air at 600 - 900 °C when compared with currently used compositions (x = 0.2) (Figure 89). This was definitely proven by repeated measurements of the electrochemical performance of the LSM electrodes on $Y(3\%)\text{-}ZrO_2$ electrolyte prepared at 1100 °C using electrochemical impedance spectroscopy and dc polarization curves for set of identically prepared samples. Several $La_{1-x}Sr_xMnO_3$ - $Y\text{-}ZrO_2$ half-cells (x = 0.2, 0.5, 0.7, and 0.8) have been prepared also in air at 1000 C. Their area specific resistance has been measured indicating good stability and reproducibility.

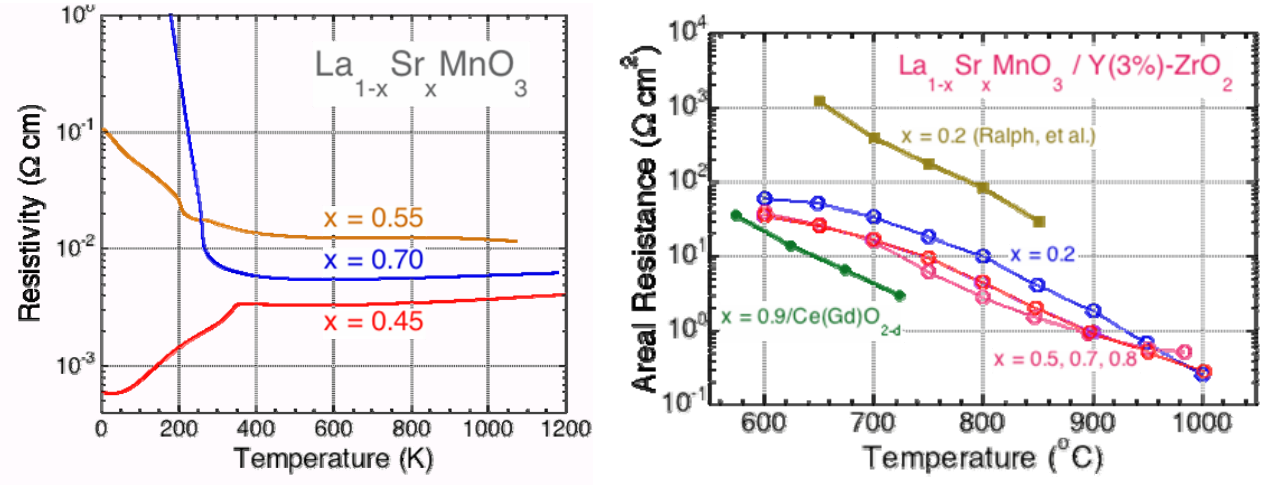

Figure 89: Resistivity and area specific resistance of selected $La_{1-x}Sr_xMnO_3$ cathodes.

Considering overall properties of the LSM compounds the best properties were found for the x = 0.7-0.8 compositions. In LSM Cathodes Summary, synthesis of new $La_{1-x}Sr_xMnO_3$ ($x > 0.5$) perovskites was optimized and new compositions are stable and metallic for $200 < T < 700$ °C. These materials show increased oxygen vacancy content. However, long-term stability with Y-ZrO_2 was shown below ~800°C. More information on some of the results described in this section can be found papers published (with a proper acknowledgment) in per review journals [132-142].

Design and synthesis of novel mixed conducting cathodes and measurements of ionic and electronic conductivity

Optimization of the substituted LSM for catalytic and oxygen conducting properties

A wide range of substituted LSM compounds have been prepared and investigated by x-ray and neutron powder diffraction and thermogravimetric measurements. A fast sample inspection method was developed for general catalytic and oxygen diffusion properties by use of thermogravimetric apparatus. After reduction of oxygen content well below 3.0 in Ar or hydrogen the samples are placed on TGA apparatus and slowly heated in oxygen (see Figure 24). The low temperature of oxygen uptake and fast mass increase indicate good catalytic properties and fast oxygen diffusion. Figure 90 shows examples of TGA oxygenations for several systems. The summary of these studies for $Sr(Fe,Mn,Co)O_{3-d}$ system is shown on Figure 91. In that system a very promising compound have been found $SrMn_{0.3}Fe_{0.7}O_{3-d}$, exhibiting reversible oxidation-reduction at temperatures lower (~ 100°C) then the best-known cathode material $SrFe_{0.2}Co_{0.8}O_{3-d}$. Low temperature of oxygen uptake and fast mass increase were also observed for the $(La,Sr)CoO_{3-d}$ system.

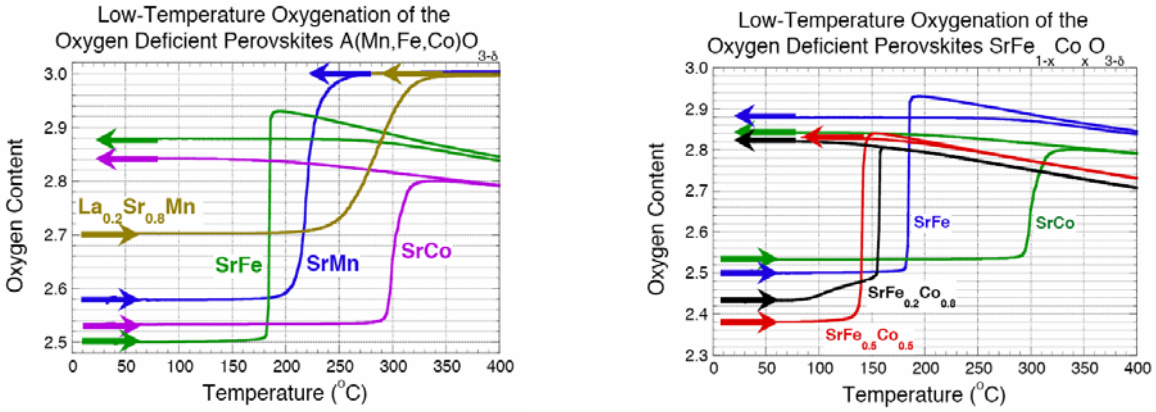

Figure 90: Low-temperature oxygenation of $Sr(Fe,Mn,Co)O_{3-d}$.

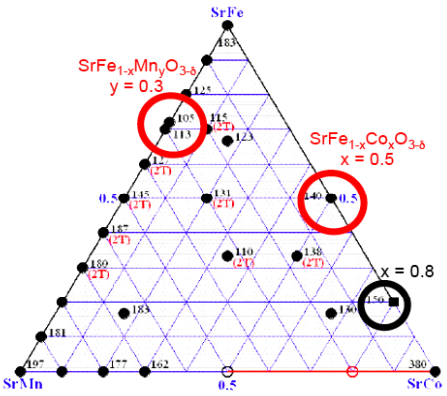

Figure 91: Oxygenation temperatures for $Sr(Fe,Mn,Co)O_{3-d}$ system.

Since $SrMn_{0.3}Fe_{0.7}O_{3-d}$ exhibits in addition suitable stability in hydrogen, samples were provided for testing as cathode materials for the PEM electrolytes. The most spectacular results were found for the pseudo-ternary system $La_{1-x}Sr_xFe_{1-y}Co_yO_{3-d}$. Figure 92 shows oxygen absorption and diffusion in these compounds at room temperature. We have identified optimal compositions, which show dramatically improved oxygen diffusion properties when compared with the currently known best cathode materials. Resistivity measurements at 500–800°C have shown very good electronic conductivities of the order of 1000 Simens. Among transition metal substituted $Sr(Mn,TM)O_{3-d}$ the lowest resistivity was observed for TM=Mo (Figure 93). In addition, enhanced stability against decomposition to hexagonal phase was observed for the high valence B = V^{5+}, Mo^{6+}, and Re^{7+}. This was confirmed by TGA measurements, which showed shift of the decomposition temperature to above 1000 C. Resistivities are increased for B = Ga^{3+}, Co^{3+}, and Fe^{3+} ions with valences smaller than that of Mn^{4+}. The high-valence substituted compounds show oxygen stoichiometric content and thermally activated behavior while the low-valence substituted compounds show increased amount of oxygen vacancies and the resistivity that is dominated by charge compensation. The same observations were made for the remaining $Sr(Fe,Mn,Co)O_{3-d}$ and $La(Fe,Ni)O_{3-d}$ compounds.

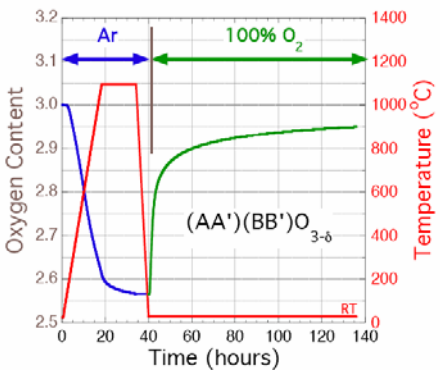

Figure 92: Low-temperature oxygenation of $La_{1-x}Sr_xFe_{1-y}Co_yO_{3-d}$.

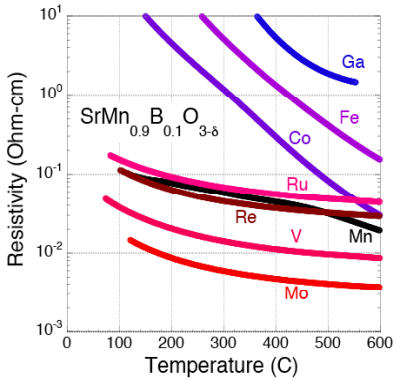

Figure 93: Resistivity of TM substituted $SrMnO_{3-d}$ cathode materials.

Chemical and Mechanical Compatibility with the Y-ZrO_2 Electrolyte

$Sr(Fe,Mn,Co)O_{3-d}$ and $(La,Sr)(Fe,Co)O_{3-d}$ compounds show reduced chemical stability against reaction with Y-ZrO_2 Electrolyte. Figure 94 shows the diffraction patterns for the ball milled $SrMn_{0.3}Fe_{0.7}O_3$-YSZ(8% Y) mixture fired for 36 h in Ar at 1000 ^oC and in air at 650 ^oC. The cathode material is stable at 650 ^oC but some decomposition occurs at 1000 ^oC. Similar results were also observed for the $SrMnO_3$ and $Sr_{0.7}Ca_{0.3}MnO_3$ samples and indicated that grinding and putting sub-micron size grains of the cathode and electrolyte in a direct contact at 1000 ^oC causes reaction of the Sr-rich LSM compositions with YSZ. However, similar study of temporal stability of the cathode and $Ce(Gd)O_2$ electrolyte interface indicated no reaction, suggesting that the use of buffer layer should limit reaction of cathode materials with the YSZ electrolyte.

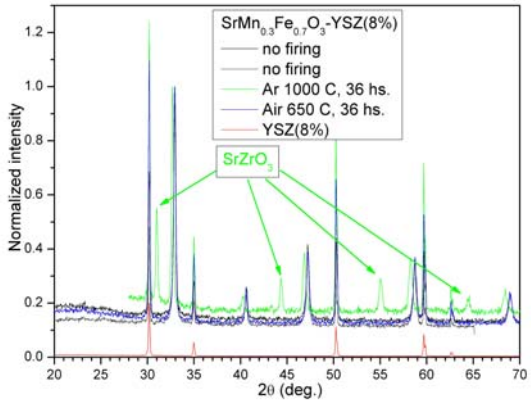

Figure 94: Study of chemical stability of $SrMn_{0.3}Fe_{0.7}O_3$ and YSZ (8% Y).

$Sr(Fe,Mn,Co)O_{3-d}$ and $(La,Sr)(Fe,Co)O_{3-d}$ compounds were found to exhibit large thermal end chemical expansion coefficients that are not compatible with any of the currently known electrolytes (see Figure 88). On the other hand the $La(Fe,Ni)O_{3-d}$ compounds showed average thermal expansion coefficient of $14.7*10^{-6}$ K^{-1} which makes this material compatible with frequently used electrolytes. At high temperatures the sample shows relatively low resistivity and behaves as a small-polaron electronic conductor with two regions of slightly different activation energies of 0.07 and 0.05 eV above and below 553 K, respectively (Figure 95).

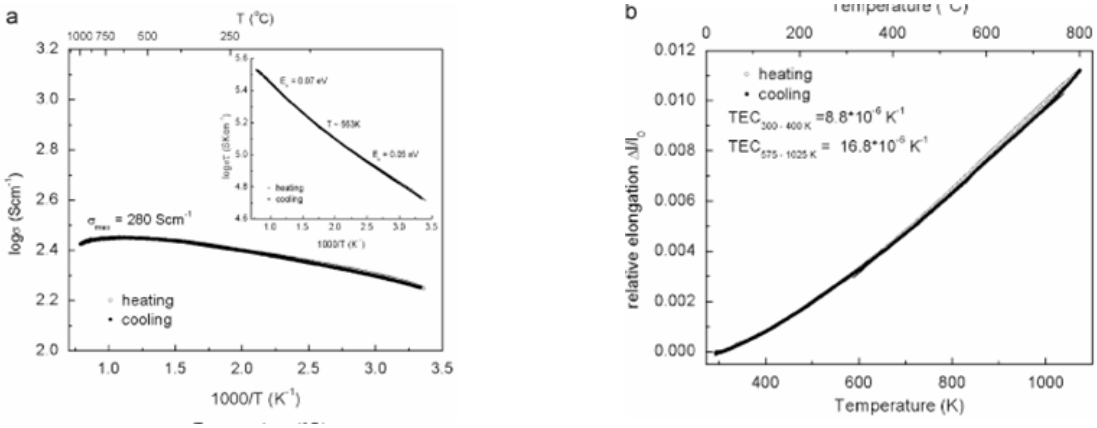

Figure 95: Conductivity and thermal expansion of $LaFe_{0.5}Ni_{0.5}O_{3-d}$.

Measurements of Area Specific Resistance

Area specific resistance measurements have been performed repeatedly for $SrMn_{0.3}Fe_{0.7}O_{3-d}$/Y-$ZrO_2$ half-cell prepared in air at 1000 °C. Its resistance was found lower than for the LSM materials (Figure 96). Figure shows impedance measurements for the first and second half-cells

at 700 °C during heating cycle. The data show complete reproducibility during holding experiments, however, the half-cells exhibit irreversible behavior during heating/cooling cycles that would require careful investigation.

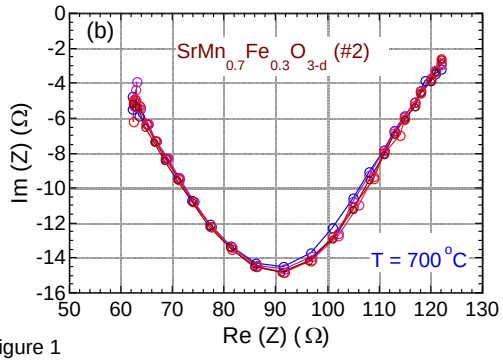

Figure 1

Figure 96: Impedance spectroscopy measurements for $SrMn_{0.3}Fe_{0.7}O_{3-d}$ half-cells at 700 °C.

Several new LSM compounds discussed here exhibit superior MIEC properties. In summary, synthesis conditions of new $Sr(Fe,Mn,Co)O_{3-d}$, $(La,Sr)(Fe,Co)O_{3-d}$, and $La(Fe,Ni)O_{3-d}$ perovskites indicate that highly Sr substituted $(La,Sr)CoO_{3-d}$ are stable in air and Ar, and are metallic to high temperatures. These materials show increased oxygen vacancy content and remarkable oxygen diffusion at low temperatures. Long-term stability with $Y\text{-}ZrO_2$ is low; stability with $Ce(Gd)O_2$ is satisfactory. ASR of $SrMn_{0.3}Fe_{0.7}O_{3-d}$ is lower than for LSM cathodes. More information on some of the results described in this section can be found papers published (with a proper acknowledgment) in per review journals [132-142].

Chapter 4 – Summary and Recommendations

Chapter 4 – Summary and Recommendations 110
Ultralow Platinum Catalysis 110
Membrane Electrode Assembly (MEA) Performance 110
Multi-Cell Analysis and Validation 111
Bipolar Plates 111
Hybrid Power 111
New Cathode Materials 112
References 112
Appendix A - List of Intellectual Property Developed from the Grant 121
Appendix B - List of Articles Published 122
Appendix C - List of Papers Presented in Meetings/Conferences 123
Appendix D - List of Thesis/Dissertations 125

Ultralow Platinum Catalysis

The composite platinum-phosphate catalyst has five advantages over conventional catalysts and can increase the power density of fuel cells. First, the entire platinum surface, not just a portion of it, is engaged in oxygen reduction with several active catalysts act as in tandem to reduce oxygen and have a larger active surfaces to reduce oxygen. Second, incorporation of bound phosphate to platinum (II) and platinum (III) oxidation states minimizes inactive hydroxide and oxide layers of platinum. Third, the loss of catalytic activity is minimized by preventing oxidation of platinum that takes place at more positive potentials. Fourth, mixed-valence surface minimizes hydrogen adsorption/desorption properties to minimize hydrogen cross-over. Finally, with or without additional catalysts life time is enhanced by minimizing carbon monoxide reduction.

Since the electrocatalyst effectively oxidizes methanol it is effectively used as an anode-catalyst for methanol oxidation. The catalyst cost is reduced with sub-milligrams of platinum. In fact, an increase of platinum content in the platinum phosphate composite over 0.1 mg/cm^2 does not increase the power density proportionally. Finally, the steady-state current-voltage responses indicate a lack of oxygen depletion when the oxygen supply is limited. This indicates a process of generating additional oxygen (presumably from water). Hence, the electrocatalyst helps alleviate mass transfer problems and manages water-flooding challenges in a membrane electrode assembly.

Membrane Electrode Assembly (MEA) Performance

The results presented in relationship to MEA performance clearly showed that the performance can be enhanced controlling the curing dynamics. A lower curing temperature allowed for slow solvent evaporation in the electrode layer, eliminated solvent trapping, and resulted in uniform

dispersion of ionomer and catalyst. The performance of MEAs fabricated using the slow curing process was relatively high. A faster curing process, achieved by increasing the curing temperature, resulted in catalyst coagulations, ionomer clustering, and uneven distributions of the catalyst and ionomer leading to poor MEA performance. Furthermore, we have enhanced the performance of the MEA up to 110 ^{o}C by adding specific reinforcing reagents.

It is recommended to pursue further work the enforcing reagents so that PEMFC can be operated at higher temperature.

Multi-Cell Analysis and Validation

Irreversible degradation was observed for a 10-cell 100 Watt polymer electrolyte fuel cell upon load cycling simulating the automotive application. The stack lasted for 480 hours under the DOE-recommended durability test protocol, after which one cell within the stack lost all voltage. Subsequent visual inspection of the cells indicated that the cause of this failure was loss of gas sealing of both the anode and cathode silicone gaskets. Gradual performance loss i observed between 240 and 480 hours of cycling.

Diagnostic tests showed that the main source of performance degradation was increase in the losses due to kinetics of the cathode reaction caused by loss of electrochemically active surface area of the platinum nanoparticle cathode electrocatalyst. This loss is caused by three processes: (1) dissolution of platinum into the cathode exhaust, (2) growth in Pt particle size from 5.3 nm to 6.2 nm, and (3) loss of utilization of the remaining Pt surface area. A drop in utilization may be caused by loss contact of the Pt particles with either the carbon support or ionomer (Nafion) in the electrode layer.

It is recommended that gaskets and electrocatalysts with higher durability be developed to meet the demanding requirements of the automotive application. Since the end cells account for a major portion of the initial performance losses in a stack, improved stack designs are needed to facilitate reactant transport to these end cells.

Bipolar Plates

High Performance bipolar plates are analyzed and designed using computer simulation model and through fabrication and testing. Results show significant improvement in bipolar plate design as demonstrated by reduce mass transfer losses and improved cell performance at high current densities. The developed computer simulation model can be used for performance evaluation of PEM fuel cell with different membrane electrode assembly and bipolar plates. The experimental test facility will be useful for evaluating newer bipolar plate design.

It is recommended that future work concentrate on the development of prototype design based on result obtained from simulation. Key issues include selection of material of construction relative to cost and manufacturability.

Hybrid Power

The transient power in a fuel cell vehicle were explored to determine the energy storage requirements in a fuel cell vehicle. This includes the distribution of power between the various power sources, and determining the power flow in the vehicle. The amount of energy storage requirements needed to aid in vehicle acceleration is one example. It was assumed the fuel cell supplied the average power while a battery and supercapactor supplied the transient power. For

the conditions of this study, very little battery power is needed for both constant force and constant power acceleration.

The power needs based on a complete driving cycle was also explored. Different constraints and objective gave widely different results. Thus the designer would have to determine which constraints best fit the design needs is critical. An optimal controller was designed to determine how the power could be divided between the various power sources. A controller can reduce the energy needs in several driving cycles. A simple motor control scheme was developed for the traction drive and a simple slip control could perform acceptably.

New Cathode Materials

New cathode materials were characterized with respect to structural properties, oxygen content and kinetics of oxygen diffusion, electrical conductivity, thermal and chemical expansion coefficients, thermal and chemical stability, and area specific resistance. Modest improvement of new LSM compositions over currently used LSM cathodes, could lower operating temperatures by 50oC. However, increased thermal and chemical expansion coefficients make these materials dissimilar with the known solid electrolytes. Significant improvement over the kinetics of oxygen diffusion and electrical conductivity was discovered for new compositions of the $Sr(Fe,Mn,Co)O_{3-d}$ and $(La,Sr)(Fe,Co)O_{3-d}$ systems. However, with these systems increased thermal and chemical expansion coefficients were observed. The need for highly conducting, mixed valent systems exhibiting large oxygen vacancy content and small chemical expansion coefficients is contradictory. Nevertheless, a new system satisfying all these above requirements was identified.

It is recommended that future work validate the utility of these new materials with measurement of critical properties. Ther is a continuing need for collaborative measurements of conductivity and thermoelectric power Q as new compounds show outstanding thermoelectric characteristics.

References

1. Steele, B.C.H., Heinzel, A., *Materials for Fuel-cell technologies*. **Nature**, 2001, 414, 345-352.

2. Ticinelli, E.A., Derouin, C. R., Redondo, A., Srinivasan, *Methods To Advance Technology Of Proton Exchange Membrane fuel Cells*, **Electrochem. Soc**., 1988, 135, 2009.

3. Srinivasa, E.A., Ticinelli, E.A., Derouin, C. R., Redondo, A., *Advances in Solid Polymer Electrolyte Fuel Cell Technology with Low Platinum Loading Electrodes*. **J. Power Sources**, 1988, 22, 359.

4. Taylor, E.B., Anderson, E.B. and Vilambi, N.R.K., *Preperation Of High-Platinum-Utilization Gas Diffusion Electrodes For Proton-Exchange-Membrane Fuel Cells*, **J. Electrochem. Soc.**, 1992, 139, L45.

5. M. W. Verbrugge, J**. Electrochem. Soc.**, 1994, 141, 46-53.

6. Coutanceau, C., Croissant, M.J., Nappron, T., Lamy, C., *Electrocatalytic Reduction Of Dioxygen At Platinum Particles Dispersed In A Polyaniline Film Electrochim*. **Acta**, 2000, 46, 579.

7. Giacomini, M.T., Ticianelli, E.A., McBreen, J., and Balasubram anian, *Oxygen Reduction On Supported Platinum/Polythiopene Electrocatalyst*s, J**. Electrochem**. Soc., 2001, 148, A323.

8. C. Zawodzinski, W ilson, M.S., and Gottesfield, S., *Proton Conducting Membrane Fuel Cell* I, Gottesfield, S., Halpert, G., Langrebe, A. Eds., **The Electrochemical Society Proceeding**, 1995, 145.

9. Wilson, M.s., Valerio, J.A., Gottesfield, S *., Low Platinum Loading Electrodes For Polymer Electrolyte Fuel Cells Fabricated Using Thermoplastic Ionomers*, **Electrochim. Acta**, 1995, 40, 355.

10. Srinivasan, S., Dillon, R., Kris hnan, L., Arico, A.S., Antonucci, V., B ocarsly, A.B., Lee, W.j., Hsueh, K.L., Lai, C.C., and Peng, A., *Techni-Economic Challenges For PEMFCS & DMFCS Enter in Energy Sectors*, in **Fuel Cell Science, Engineering and Technology**, Shah, R.K. Ed., ASME, New York, 2003.

11. Hirano, S., Ki m, J., Srinivasan, S., *High Performance Proton Exchange Fuel Cells With Sputter Deposited Pt Layer Electrodes*, **Electrochim. Acta**, 1997, 42, 1587.

12. O'Hayre, R., Lee, S.J., Cha, C. W ., Prinz, F.B., *A Sharp Peak In The Performance Of Sputtered Platinum Fuel Cells T Ultra-Low Platinum Loading*, **J. Power Sources**, 2002, 109, 483.

13. H. A. Gasteiger, S.S. Kocha, B. Som palli, F .T. W agner, *Activity Benchmarks And Requirements For Pt, Pt-Alloy And Non-Pt Oxygen Reduction Catalysts For PEMFCs*, **Applied Catalyst B: Environmental**, 2005, 56, 9-35.

14. V. Stam enkovic, B. Fowler, B.M. Mun, G. Wang, P.N. Ross, C.A. Lucas, and N.M. Markovic, *Improved Oxygen Reduction Activity On Pt3Ni(111) Via Increased Surface Site Availability*, **Science**, 2007, 315, 493-496.

15. Gulla, A.F., Saha, M.S., Allen, R.J., Mukerjee, S., *Dual Ion-Beam Assisted Deposition As A Method To Obtain Low Loading-High Performance Electrodes For PEMFCs*, **Electrochem. Solid-State Lett**., 2005, 8, A504-508.

16. Rajesh, B., Thambi, K.R., Bonard, J.M., Mathieu, H.J., Xanthopoulos, N., Viswanathan, B. **Chem. Comm**., 2003, 16, 2022-2023.

17. Li, W. Z.' Liang, C.H., Qiu, J.S., Z hou, W.J., Han, H.M., Wei, Z.B., Sun, G. Q., Xin, Q., **Carbon**, 2002, 40, 791.

18. Serp, P. Corrias, M., Kalack, P., **Appl. Catal**., 2003, 253, 337.

19. Bassel, C., Laubernds, K., Rodr iguez, N.M, Baker, R.T., **J. Phys. Chem. B**, 2001, 105, 1115-1118.

20. Hacker, V., Wallnofer, E., Baum gartner, W., Schaffer, T., Besenhard, J.O., Schrottner, H., Schmied, M., **Electrochem Comm**., 2005, 7, 377-382.

21. Girishkumar, G., Vinodgopal, K., Kamat, P, **J. Phys. Chem. B**, 2004, 108, 19960-19966.

22. Liu, Z., Lin, W ., Lee, J. Y., Zhang, W ., Han, M., and Gan, L.M., Langm uir, 2002, 18, 4054-4060.

23. Swider, K. E., Rolinson, D. R., **Electrochem Solid-State Lett**., 2000, 3, 4; Swider, K.E., and Rolinson, D.R., Langmuir, 1999, 15, 3302.

24. Liu, W. –J., Wu, B. L., Cha, C.S., **J. Electroanal. Chem**., 1999, 576, 101.

25. Hills, C.W., Masher, M.S., Frenkel, A.I., Shapley, J.R., Nuzzo, R.G., Langmuir, 1999, 15, 690.

26. Lin, S.D.; Hsiao, T. –C., Chang, J. –R., Lin, A.S., **J. Phys. Chem. B**, 1999, 103, 97.

27. Barnakov, C.N., Seit-Ablaeva, S.K., Kozlov, A.P., Rokosov, Yu.V., Fenelonov, V.B., Parmon, V.N., 2003, **Russian Patent** No. 2,206,394.

28. Ismagilov, Z.R., Kerzhentsev, Shikina, N.V ., Lisitsyn, A.S., Okhlopkova, L.B., Bar nakov, Ch.N., Sakashita, M., Iijima, T., Tadokoro, K., **Catalyst Today**, 2005, 102-103, 58-66.

29. Bregoli, L.J., Electrochim. Acta, 1978, 23, 489; Kinoshita, K., **J. Electrochem. Soc**., 1990, 137, 845-848.

30. Mukerjee, S., McBreen J., **J. Electrochem**., 1998, 448, 163-171.

31. Depa, D.B., Vojnovic, M. V., Vracar, L.M., Damjavovic, **Electrochim. Acta**, 1987, 32, 129.

32. Mukerjee S., Srinivasan, M., Soraiga, McBean, J., **J. Phys. Chem**., 1995, 99, 4577.

33. Min, J., Cho, J., Cho, K. Kim, H., **Electro. Chim. Acta**, 2000, 45, 4211.

34. Toda, T., Igarashi, H., Uchida, H., Watanabe, M., **J. Electrochem. Soc**., 1999, 146, 3750.

35. Teliska, M., Murthi, V.S., Mukerjee, S., Ramaker, D.E., **J. Electrochem. Soc**., 2005, 152, A2159-A2169.

36. Jalan, V., Taylor, E.J., **J. Electrochem. Soc**., 1983, 130, 2299-2301

37. Wang, J. X., Markovic, N.M., Adzic, R.R., **J. Phys. Chem. B**, 2004, 108, 4127

38. Uribe, F.A., Zawodzinski, T. A., **Electrochim. Acta**, 2002, 47, 3799.

39. Rajesh, B., Thambi, K.R., Bonard, J.M., Mathieu, H.J., Xanthopoulos, N., Viswanathan, *Carbon Nanotubes As Support For Cathode Catalyst Of A Direct Methanol Fuel Cell*, **B. Chem. Comm.**, 2003, 16, 2022-2023.

40. Li, W. Z.' Liang, C.H., Qiu, J.S., Zhou, W.J., Han, H.M., Wei, Z.B., Sun, G. Q., Xin, Q., *Carbon Nanotubes And Nanofibers In Catalysis*, **Carbon**, 2002, 40, 791.

41. Serp, P. Corrias, M., Kalack, P., *Carbon Nanotubes and Nanofibers in Catalysis*, **Appl. Catal.**, 2003, 253, 337.

42. Bassel, C., Laubernds, K., Rodriguez, N.M, Baker, R.T., *Carbon Nanofiber-Based Active Layers For Fuel Cell Cathodes – Preparation And Characterization* , **J. Phys. Chem. B**, 2001, 105, 1115-1118.

43. Hacker, V., Wallnofer, E., Baumgartner, W., Schaffer, T., Besenhard, J.O., Schrottner, H., Schmied, M., *Carbon Nanostructures in Portable Fuel Cells: Single-Walled Carbon Nanotube Electrodes for Methanol Oxidation and Oxygen Reduction*, **Electrochem Comm**., 2005, 7, 377-382.

44. Girishkumar, G., Vinodgopal, K., Ka mat, P, *Preparation and Characterization of Platinum-Based Electrocatalysts on Multiwalled Carbon Nanotubes for Proton Exchange Membrane Fuel Cells*, **J. Phys. Chem. B**, 2004, 108, 19960-19966.

45. Liu, Z., Lin, W ., Lee, J. Y., Zh ang, W ., Ha n, M., and Gan, L.M., *Preparation and Characterization of Platinum-Based Electrocatalysts on Multiwalled Carbon Nanotubes for Proton Exchange Membrane Fuel Cells*, **Langmuir**, 2002, 18, 4054-4060.

46. Swider, K. E., Rolinson, D. R., *Reduced Poisoning of Platinum Fuel-Cell Electrocatalysts Supported on Desulfurized Carbon*, **Electrochem Solid-State Lett**., 2000, 3, 4

47. Swider, K.E., and Rolinson, D.R., *Catalytic Desulfurization of Carbon Black on a Platinum Oxide Electrode*, **Langmuir**, 1999, 15, 3302.

48. Liu, W . J., Wu, B. L., Cha, C.S., *Surface Diffusion And The Spillover of H Atoms And Oxygen-Containing Surface Species On The Surface Of Carbon Black And Pt/C Porous Electrodes*, **J. Electroanal. Chem**., 1999, 576, 101.

49. Hills, C.W ., Masher, M .S., Frenkel, A.I., Shapley, J.R., Nuzzo, R.G., *Carbon Support Effects on Bimetallic Pt - Ru Nanoparticles Formed from Molecular Precursors*, **Langmuir**, 1999, 15, 690.

50. Lin, S.D.; Hsiao, T. C., Chang, J. R., Lin, A.S., *Morphology of Carbon Supported Pt -- Ru Electrocatalyst and the CO Tolerance of Anodes for PEM Fuel Cells*, **J. Phys. Chem. B**, 1999, 103, 97.

51. Kumar, A and Ra mana G. Reddy (2003) *Effect Of Channel Dimensions And Shape In The Flow-Field Distributor On The Performance Of Polymer Electrolyte Membrane Fuel Cells*, **Journal of Power Source**, vol.113, pp. 11-18.

52. Kumar, A and Ram ana G. Reddy (2004) *Recent Developments In Materials, Design And Concepts For Bipolar/End Plates In PEM Fuel Cells*, **Advanced Materials for Energy Conversion II**, TMS., pp. 317-324.

53. Curtis, M., and L. Xianguo, L., *Performance Modeling Of A Proton Exchange Membrane Fuel Cell*, **Proceedings of the 1998 ASME Energy Source Technology Conference**, 1998.

54. Berning, T and D. M. Lu and N. Djilali, (2002), *Three-Dimensional Computational Analysis Of Transport Phenomena In A PEM Fuel Cell*, **Journal of Power Sources**, 106, pp. 284-294, 2002.

55. Nguyen, P. T., T. Berning and N. Djilali, *Computational Model Of A PEM Fuel Cell With Serpentine Gas Flow Channels*, **Journal of Power Sources**, 130, pp. 149-157, 2004.

56. Boddu, R and P. Majumdar., *Computational Flow Analysis of Bipolar Plate for Fuel Cells*, **ASME Transactions – Journal of Fuel Cell Science and Technology**, Vol. 5, 2008.

57. H.A. Gasteiger, S.S. K ocha, B. S ompalli, an d F.T. W agner, **Applied Catalysis B-Environmental**, 56 [1-2] (2005) 9-35.

58. H. Xu, Y. Song, H.R. Kunz, and J.M. Fenton, **Journal of the Electrochemical Society**, 152 [9] (2005) A1828-A1836.

59. Anima B. Bose, Ruhulla Shaik, and Jennifer Mawdsley, **J. Power Sources**, 2008, 182, 61-65.

60. X.L. Cheng, B.L. Yi, M. Han, J.X. Zhang, Y.G. Qiao, and J.R. Yu, **Journal of Power Sources**, 79 [1] (1999) 75-81.

61. H. Mizuhata, S. Nakao, and T. Yamaguchi, **Journal of Power Sources**, 138 [1-2] (2004) 25-30.

62. K. Wikander, H. Ekstroem, A.E.C. Palmqvist, and G. Lindbergh, **Electrochimica Acta**, 52 [24] (2007) 6848-6855.

63. M.V. Williams, H.R. Kunz, and J.M. Fenton, **Journal of Power Sources**, 135 [1-2] (2004) 122-134.

64. S. Koh, J. Leisch, M.F. Toney, and P. Strasser, **Journal of Physical Chemistry C**, 111 [9] (2007) 3744-3752.

65. B.N. Popov and H.R. Colon-Mercado, **Journal of Power Sources**, 155 [2] (2006) 253-263.

66. M.S. Wilson and S. Gottesfeld, **Journal of the Electrochemical Society**, 139 [2] (1992) L28-L30.

67. P. Gode, F. Jaouen, G. Lindber gh, A. Lundblad, and G. Sundholm , **Electrochimica Acta**, 48 [28] (2003) 4175-4187.

68. E. Passalacqua, F. Lufrano, G. Squadrito, A. Patti, and L. Giorgi, **Electrochimica Acta**, 46 [6] (2001) 799-805.

69. E.A. Ticianelli, C.R. Derouin, and S. Srinivas an, **Journal of Electroanalytical Chemistry**, 251 [2] (1988) 275-295.

70. G.C. Li and P.G. Pickup, **Journal of the Electrochemical Society**, 150 [11] (2003) C745-C752.

71. M.S. Wilson and S. Gottesfeld, **Journal of Applied Electrochemistry**, 22 [1] (1992) 1-7.

72. M.S. W ilson, J.A. Valerio, and S. Gottesfeld, **Electrochimica Acta**, 40 [3] (1995) 355-363.

73. O.J. Murphy, G.D. Hitchens, and D.J. Manko, **Journal of Power Sources**, 47 [3] (1994) 353-368.

74. D. Liu and S. Case, **Journal of Power Sources**, 162 [1] (2006) 521-531.

75. D.S. Chan and C.C. Wan, **Journal of Power Sources**, 50 [3] (1994) 261-281.

76. N. Giordano, E. Passalacqua, V. Alderucci, P. Staiti, L. Pino, H. Mirzaian, E.J. Taylor, and G. Wilemski, **Electrochimica Acta**, 36 [5-6] (1991) 1049-1055.

77. N. Giordano, E. Passalacqua, V. Recupero, M. Vivaldi, E.J. Taylor, and G. Wilem ski, **Electrochimica Acta**, 1990, 35 [9], 1411-1421.

78. M. W atanabe, K. Makita, H. Usam i, and S. Motoo, **Journal of Electroanalytical Chemistry**, 1986, 197 [1-2], 195-208.

79. M. Watanabe, M. Tomikawa, and S. Motoo, **Journal of Electroanalytical Chemistry**, 1985, 195 [1], 81-93.

80. Z. Poltarzewski, P. Staiti, V. Alderucci, W. Wieczorek, and N. Giordano, **Journal of the Electrochemical Society**, 1992, 139 [3], 761-765.

81. M. F. Mathias, R. Makharia, H. A. Gasteiger, J. J. Conley, T. J. Fuller, C. J. Gittleman, S. S. Kocha, D. P. Miller, C. K. Mittelsteadt, T. Xie, S. G. Yan, P. T. Yu: "*Two Fuel Cell Cars In Every Garage?*", **Interface 2005**, 14, 24-35.

82. M. Mathias, H. Gasteiger, R. Makharia, S. Kocha, T. Fuller, T. Xie, J. Pisco, *Can Available Membranes and Catalysts Meet Automotive Polymer Electrolyte Fuel Cell Requirements?* in A.C. Society (Ed.), **American Chemical Society Fall National Meeting**, Philadelphia, PA, 2004.

83. N. Garland, *Plenary Session - Fuel Cells*, **2008 DOE Hydrogen Program Merit Review and Peer Evaluation Meeting**, Washington, D.C., 2008.

84. M. Debe, *Advanced Cathode Catalysts and Supports for PEM Fuel Cells* (FC1), **2008. DOE Hydrogen Program Merit Review and Peer Evaluation Meeting**, Washington, D.C., 2008.

85. **DOE-EERE, Hydrogen Multi-Year Program Plan**, Washington, D.C., 2006.

86. F. A. de Bruijn, V. A. T. Dam, G. J. M. Janssen: " *Durability And Degradation Issues Of PEM Fuel Cell Components*", **Fuel Cells**, 2008, 8, 3-22.

87. R. Borup, J. Meyers, B. Pivovar, Y. S. Kim, R. Mukundan, N. Garland, D. Myers, M. Wilson, F. Garzon, D. Wood, P. Zelenay, K. More, K. Stroh, T. Zawodzinski, J. Boncella, J. E. McGrath, M. Inaba, K. Miyatake, M. Hori, K. Ota, Z. Ogumi, S. Miyata, A. Nishikata, Z. Siroma, Y. Uchimoto, K. Yasuda, K. I. Kimijima, N. Iwashita : "*Scientific Aspects of Polymer Electrolyte Fuel Cell Durability And Degradation*", **Chemical Reviews 2007**, 107, 3904-51.

88. J. St-Pierre, D.P. Wilkinson, S.D. Knights, M. Bos, **J. New Mater. Electrochem. Syst.**, 2000, 3, 99.

89. J. St-Pierre, N. Jia, **J. New Mater**. Electrochem. Syst. 2002, 5, 263.

90. Bose, R.N., Viola, R.E., Cornelius, R.D., **J. Am. Chem. Soc**., 1984, 106, 3336-3344.

91. Bose, R. N., Cornelius R.D., Viola, R.E., **J. Am. Chem. Soc**., 1986, 108, 4403.

92. Mishur, R.; Zheng, C., Gilbert, T.M., Bose, R.N., **Inorg. Chem**., 2008, in press.

93. R. N. Bose and A. Bose, **International Application No. PCT/ US2003/041521** (Passed Examination).

94. A. B. Bose, M. Sarkar, R. N. Bose, **J. Power Sources**, 2006, 157, 188-194.

95. Kouvetakis, J.; Kaner, R. B.; Sattler, M. L. and Bartlett, N., **J. Chem. Soc. Chem. Commun**. 1986, 1758.

96. Chesneau, M.; Beguin, F.; Conard, J.; Erre, R. and Thebault, J., **Carbon**, 1992, 30, 714.

97. Wang, Q.; Ma, X.; Chen, L-Q.; Cermignani, W. and Pantano, C.G., **Carbon**, 1997, 35, 307.

98. Lowell, C. E., **J. Am. Ceram. Soc**. 1967, 50, 142.

99. Wagner, P.; Dickinson, L. M., **Carbon**, 1970, 8, 313.

100. Jones, L. E.; Thrower, P. A., **Carbon**, 1991, 29, 251.

101. Zhong, D. H.; Sano, H.; Uchiyama, Y.; Kobayashi, K., **Carbon**, 2000, 38, 1199.

102. Avila-Garcia, M. Plata-Torres, M.A. Dominguez-Crespo, C. Ramirez-Rodriguez, and E.M. Arce-Estrada, **Journal of Alloys and Compounds**, 2007, 434-435,764-767.

103. N.P. Siegel, M.W . Ellis, D.J. Nelson, and M.R. von Spakovsky, **Journal of Power Sources**, 2003, 115 [1], 81-89.

104. L.C. Sawyer and D.T. Grubb, **Polymer Microscopy**, Chapman & Hall: London, 1996, p. 91-94.

105. U.S. DOE, **Durability Test Protocol for PEM Fuel Cells**, 2005.

106. Iqbal Husain, **Electric and Hybrid Vehicles Design Fundamentals**, CRC PRESS.

107. Benjamin Lev, **Introduction to Mathematical Programming**, Elsevier north H olland 1982.

108. Frederick S. Hillier **Introduction to Mathematical Programming** Mcgraw-Hill College 1995.

109. Frank L. Lewis & Vassilis L. Syrmos, **Optimal Control**, John Wiley &Sons, Inc. 1995.

110. G. R. Sle mon and A. Straughen, **Electric Machines**. Readings, MA: Addison-Wesley, 1982.

111. F. Guarr, F. C. Anson, **J. Phys. Chem**., 1987, 91, 4037-4043.

112. P. Denisevich, K. Willman, R. W. Murray, **J. Am. Chem. Soc**., 1981, 103, 4727.

113. M. W. Verbrugge, **J. Electrochem. Soc**., 1994, 141, 46-53.

114. N. R. K. V. Reddy, E. B. Anderson, E.J. Taylor, **U.S. Patent No. 5,084,114 9**, 1992.

115. E. J. Taylor, E. B. Anderson, N.R.K V. Reddy, **J. Electrochem. Soc**., 1992, 139, L45.

116. K. H. Choi, H.S. Kim, T. H. Lee, **J. Power Sources**, 75 (1998) 230.

117. S.D. Thompson, L. R. Jordon, M. Forsyth, **Electrochimica Acta**, 46 (2002) 1657-1663.

118. F. Gloaguen, J. –M. Leger, C. Lamy, **J. Appl. Electrochem**., 27 (1997)1052.

119. M. Arnez, J. J. Schm idt, K. W andelt, P. N. Boss , N.M. Markovic, **J. Phys. Chem**. B, 197 (2003) 9813-9819.

120. A. Bose, D. Thati, work in progress.

121. P. J. Bouwman, W. Dmowski, J. Stanley, G. B. Cotton, K. E. Swider-Lyons, **J. Electroanl. Soc.**, 151 (2004) A1989-A1998.

122. Acharya, C. K. and Turner, C. H. *Stabilization of Platinum Clusters by Substitutional Boron Dopants in Carbon Supports*, **J Phys Chem B** (letter), 2006, 110, 17706.

123. Wilcox, D. L. Sr.; Berg, M. *Microsphere Fabrication and Applications: An Overview*, In: Wilcox, Sr. D. L.; Berg, M.; Bernat, T.; Kellerm an, D.; and Cochran, J. K. Jr, E ditors, **Mat. Res. Soc. Symp. Proc 1995**, 372, 3.

124. Amano, I.; Kano, H.; Takahira, H.; Ya mamoto, Y.; Itok, K.; Iwatsuki, S. et al. editors, **Artificial Kidney, Artificial Liver And Artificial Cell**, New York: Plenu m Press, 1978, pp. 89–98.

125. Yang, J.; Ling, L.-C.; Liu, L.; Kang, F.-Y.; Huang, Z.-H. and W u, H. *Preparation And Properties Of Phenolic Resin-Based Activated Carbon Spheres With Controlled Pore Size Distribution*, **Carbon**, 2002, 40, 911.

126. H.A. Gasteiger, W. Gu, R. Makharia, M.F. Mathias, and B. Som palli, **Handbook of Fuel Cells--Fundamentals, Technology, and Applications**, W. Vielstich, A. Lamm, and H.A. Gasteiger, Editors, John Wiley & Sons, Ltd.: West Sussex, England, p. 591-610, 2003.

127. R. O'Hayre, D.M. Barnett, and F.B. Prinz, **Journal of the Electrochemical Society**, 152 [2] (2005) A439-A444.

128. P. Spinelli, C. Francia, E.P. Ambrosio, and M. Lucariello, " *Semi-Empirical Evaluation Of PEMFC Electro-Catalytic Activity*", **J. Power Sources**, 178 (2008) 517–524.

129. A. Parthasarathy, S. Srinivasan, and A.J. Appleby, C.R. Martin, "*Temperature Dependence of the Electrode Kinetics of Oxygen Reduction at the Platinum/Nafion® Interface – A Microelectrode Investigation***" J. Electrochem. Soc**. 139 (1992) 2530.

130. K.C. Neyerlin, **J. Electrochem. Soc**., 153 (2006) A1955.

131. Wolf Vielstich, Arnold Lamm, Hubert A. Gasteiger, **Handbook of Fuel Cells,** Volume 3, John Wiley & Sons Ltd, 2003.

132. R. Makharia, S. Kocha, P. T. Yu, M. A. Sweikart, W. Gu, F. T. W agner, H. A. Gasteiger: "*Durable PEM Fuel Cell Electrode Materials: Requirements and Benchmarking Methodologies*", **ECS Transactions** 1 (2006) 3-18.

133. H.A. Gasteiger, S.S. K ocha, B. S ompalli, an d F.T. W agner, **Applied Catalysis B: Environmental**, 56 (2005) 9-35.

134. T. Markel, M. Zolot, K . B. W ipke, and A. A. Pesaran, **Advanced Automotive Battery Conference**, June 10-13, 2003.

135. Copparapu, R., Zinger, D.S., Bose, A., " *Energy Storage Analysis Of A Fuel Cell Hybrid Vehicle With Constant Force Acceleration Profile*",IEEE, **North American Power Symposium**, 38th,2006, 43-7.

136. A.Bose, D. Zinger, and H. Yu, " *Active Electrical Power Flow Control System for Optimization of Power Delivery in Electric Hybrid Vehicles*" **Utility Patent Application # 12/137,849**.

137. S. Kolesnik, B. Dabrowski, J. Mais, M. Ma jjiga, O. Chm aissem, A. Baszczuk, and J.D. Jorgensen, **Phys. Rev. B**, 73, 214440 (2006).

138. J. Pie tosa, A. W isniewski, R. Puzn iak, S. Kole snik, M. Majjiga, and B. Dabrowski, **Acta Physica Polonica A** 109, 527 (2006).

139. [O. Chmaissem, B. Dabrowski, S. Kolesnik, and J. Mais, **Phys. Rev. B,** 74, 144415 (2006).

140. O. Chmaissem, J. Mais, B. Dabrowski, and J.D. Jorgensen, **J. of Solid State Chem**. 180, 1698 (2007).

141. O. Chmaissem, L. Suescun, and J. Mais, **Acta Physica Polonica**, 111, 15 (2007).

142. [A. Baszczuk, S. Kolesnik, B. Dabrowski, O. Chmaissem, J. Mais**, Phys. Rev**., 76, 134407 (2007)

143. L. Suescun, B. Dabrowski, J. Mais, S. Remsen, J.W. Richardson Jr., E.R. Maxey, and J.D. Jorgensen, **Chem. Mater**., 2008, 20, 1636–1645.

144. L. Suescun and B. Dabrowski, **Acta Cryst. B**, 64, 177-186 (2008).

145. M. Gateshki, L. Suescun, S. Kolesnik, J. Mais, K. Swierczek and B. Dabrowski, **J. of Solid State Chem.** 181, 1833 (2008).

146. L. Suescun and B. Dabrowski, *Synthesis and Structural Characterization of* $La_xSr_{1-x}MnO_{2.6+d}$ *(0.1 < X < 0.4) Compounds Displaying Compressed Octahedral Coordination Of* $Mn^{(4-5x)+}$, (accepted **J. of Solid State Chem**.).

Appendix A - List of Intellectual Property Developed from the Grant

R. N. Bose and A. Bose, "**Metal Coated Carbon Surfaces for Use in Fuel Cells**," International Application No. PCT/ US2003/041521(Passed Examination).

Bose and R. N. Bose , " **Multifunctional Tunable Metal-Phosphate Composite Electro-Catalyst for Efficient Oxygen Reduction and Methanol Oxidation Applications in Fuel Cells and Electrolysis,** U.S. Patent and Trademark Office. Utility Patent Applications No. 12/074,507, March 2008.

Bose and R. Marin, " **Methods Of Preparing Metal Phosphate Composite Catalyst**" U.S. Patent and Trademark Office, Utility Patent Application No. 12/074,425, March 2008.

A.Bose, D. Zinger, and H. Yu, " **Active Electrical Power Flow Control System for Optimization of Power Delivery in Electric Hybrid Vehicles**" Utility Patent Application # 12/137,849**.**

Bose and J. Yang, " **Nano-Porous Boron-Carbon Microspheres**" Disclosure submitted at Northern Illinois University September 2008.

Appendix B - List of Articles Published

1. Anima B. Bose, Ruhulla Sh aik, and Jennifer Mawdsley, *Optimization of the Performance of Polymer Electrolyte Fuel Cell Membrane-Electrode Assemblies: Roles of Curing Parameters on Catalyst and Ionomer Structures and Morphology*, **J. Power Sources**, 2008, 182, 61-65.

2. A. B. Bose, M. Sarkar, R. N. Bose, *Electrocatalytic Reduction Of Platinum Phosphate Blue On Carbon Surfaces: A Novel Method For Preparing Fuel Cell Electrodes*, **J. Power Sources**, 2006, 157, 188-194.

3. R. Boddu and P. Majumdar, *Computational Flow Analysis of Bi-polar Plate for Fuel Cells*, **Transactions of the ASME Journal of Fuel Cell Science and Technology**, Vol.8, No.4. 2008 p. 041002-1- 041002-8.

4. S. Kolesnik , B. Dabro wski, J. Mais, M. Majjiga, O. Ch maissem, A. Baszczuk, and J.D. Jorgensen, *Tuning Of Magnetic And Electronic States By Control Of Oxygen Content In Lanthanum Strontium Cobaltites*. **Phys. Rev. B** 73, 214440 (2006)

5. *Influence of Pressure on Magnetic Properties of $La_{1-x}Sr_xCoO_{3-d}$ (x = 0.5, 0.67, and 1)*. J. Pietosa, A. W isniewski, R. Puzniak, S. Kolesnik, M. Majjiga, and B. Dabrowski, **Acta Physica Polonica A** 109, 527 (2006)

6. *Effects of Internal Structural Parameters on the Properties of Ba-Substituted $La_{0.5}Sr_{0.5}MnO_3$*. O. Chm aissem, B. Dabrowski, S. Kolesnik, and J. Mais, **Phys. Rev. B** 74, 144415 (2006)

7. *Crystal Structures, Charge and Oxygen-Vacancy Ordering In Oxygen Deficient Perovskites $SrMnO_x$ (x < 2.7)* L. Suescun, O. Chm aissem, J. Mais, B. Dabrowski, and J.D. Jorgensen, **J. of Solid State Chem.** 180, 1698 (2007)

8. *Novel Properties of Atomically Arranged Perovskites*. B. Dabrowski, S . Kolesnik, O. Chmaissem, L. Suescun, and J. Mais, **Acta Physica Polonica** 111, 15 (2007)

9. *Structural, transport and Magnetic Properties Of Cation Ordered Cobalt Perovskite $Ho_{1/3}Sr_{2/3}CoO_{3-\delta}$*. A. Baszczuk, S. Kolesnik, B. Dabrowski, O. Chm aissem, J. Mais, **Phys. Rev.** 76, 134407 (2007) *Oxygen Ordered Phases in $La_xSr_{1-x}MnO_3$ ($0 \le x \le 0.2$): An In-Situ Neutron Powder Diffraction Study*. L. Sue scun, B. Da browski, J. Mais, S. Rem sen, J.W. Richardson Jr., E.R. Maxey, and J.D. Jorgensen, **Chem. Mater**. 2008, 20, 1636–1645

11. *Sr4+nMnIII4MnIVnO10+3n: A New Homologous Series of Oxygen Vacancy-Ordered Perovskite Compounds Built from MnIII-O Pyramids and MnIV-O Octahedra*. L. Suescun and B. Dabrowski, **Acta Cryst**. B64, 177-186 (2008)

12. *Structural, Magnetic And Electronic Properties Of Lani0.5Fe0.5O3 In The temperature range 5 - 1000 K*. M. Gateshki, L. Suescun, S. Kole snik, J. Mais, K. Swierczek and B. Dabrowski**, J. of Solid State Chem**. 181, 1833 (2008)

13. *Synthesis And Structural Characterization of $La_xSr_{1-x}MnO_{2.6+d}$ ($0.1 < x < 0.4$) Compounds Displaying Compressed Octahedral Coordination of $Mn^{(4-5x)+}$*, L. Suescun and B. Dabrowski (accepted **J. of Solid State Chem**.)

Appendix C - List of Papers Presented in Meetings/Conferences

1. B. Bose, D. Thati, R. S ubramanian, *Nano-Catalytic Pt-Electrodes for Fuel Cell*, **Fuel Cell Gordon Conference**, July 2006.
2. Bose, D. Thati, and R. Subram anian, *Novel Thin-Films Platinum Electrodes With Excellent Oxygen Reduction And Methanol Oxidation Properties*, **233rd National ACS Meeting**, Chicago, March 2007, Abstract # PETR 0061.
3. Bose, R. Shaik, D. Myers, *Dependence of Fuel Cell Performance on Inomer Structure and Morphology*, **Electrochemical Society International Meeting**, Chicago, May 2007, Abstract # 882.
4. R. Boddu and P. Majumdar, *Computational Analysis Of Bi-Polar Plate For Fuel Cells*, **Proceedings of the Fourth International ASME Conference on Fuel cell Science, Engineering and Technology**, June 2006. No.4, pp. 663-671.
5. Copparapu, R., Zinger, D.S., Bose, A., *Energy Storage Analysis Of A Fuel Cell Hybrid Vehicle With Constant Force Acceleration Profile*, IEEE, **North American Power Symposium**, 38th,2006, 43-7.
6. Rajesh Boddu, Uday Kumar Marupakula, Ben Summers and Pradip Majumdar, *Development of Bi-polar Plates with Different Flow Channel Configurations for Fuel Cells*, **Proceedings of FUELCELL2007, The 5th International Conference on Fuel Cell Science, Engineering and Technology**, 25091,June 19-21, 2007.
7. *Experimental Evaluation of Bipolar Plate Designs for Fuel Cell*"**,** Benjamin Su mmers and Pradip Majum dar, **Proceedings of the European Fuel cell Technology & Application Conference**, RFC2007-39247, 2007.
8. Pradip Majumdar, *Modeling, Simulation and Development of PEM Fuel Cell With Bipolar Plates*, Invited Key Note Presentation, **International Workshop on Engineering Fundamentals and Applications of Fuel Cells**, January 9 –10, 2008 , Jadavpur University, Kolkata, India.
9. *Towards Novel Mixed-Conducting Perovskites with Improved Ionic and Electronic Transport*. Contributed talk at **European-MRS 2005 Spring Meeting**, Strasbourg (France), May 31 - June 3, 2005.
10. *Synthesis and Properties of Mixed-Conducting Perovskites* $La_{1-x}Sr_xMnO_3$ *(x > 0.5).* Contributed talk at **European-MRS 2006 Spring Meeting**, Nice (France), May 29 – June 2, 2006.
11. *Synthesis and properties of* $La_{1-x}Sr_xMnO_3$ *(x > 0.5) for cathodes of SOFC*. **Plenary talk at the 10th Fast Ion Conduction Symposium,** Augustow (Poland), September 13 - 17, 2006.
12. *Synthesis, Oxygen Vacancy Ordering, And Properties of* $La_{1-x}Sr_xMnO_{3-d}$. **Contributed talk at the First Polish Forum on Fuel Cells and Hydrogen Technologies**, Zakopane, Poland, September 5 – 7, 2007.

13. *Oxygen Vacancy Order and Properties of $La_{1-x}Sr_xMnO_{3-d}$ ($x \geq 0.5$)*. **Contributed talk at the 11th European Conference on Solid State Chemistry**, Septem ber 11-13, 2007, Caen, France.

Appendix D - List of Thesis/Dissertations

1. D. Thati, " **Development of Low Nano-Platinum Loaded Electro-catalyst for PEM Fuel Cell**, M.S. Thesis, Northern Illinois University, December 2006.
2. R.Shaik, " **Thin Film Cathode Catalysts for Polymer Electrolyte Fuel Cells and Investigation of the Role of Ionomer in the Polymer Electrolyte Fuel Cell Catalyst Layer"**, M. S. Thesis, Northern Illinois University, December 2006.
3. P. K. Poth araju, " **Analysis of a PEM Fuel Cell Using a Finite Element-Based Computational Model"**, M.S. Thesis, Northern Illinois University, May 2006.
4. R. Subra manian, "**New Bimetallic Nano-catalysts for Direct Methanol Fuel Cell"**, M.S. Thesis, Northern Illinois University, May 2007.
5. R. Balan, " **Durability of Small PEM Fuel Cell Stack**", M.S. Thesis, Northern Illino is University, May 2007.
6. Zhihong Yu, "**Static and Dynamic Optimal Controls for Fuel-Cell Hybrid Vehicle Power System**", M. S. Thesis, Northern Illinois University, Dec. 2007.
7. R. Copparapu, " **Energy Storage Analysis of a Fuel Cell Vehicle with Constant Force Acceleration Profile**", M.S. Thesis, Northern Illinois University, December 2005.
8. Timothy D ittmer, "**A Closed Loop Induction Motor Torque Controller for a Hydrogen Fuel Cell Vehicle**", M.S. Thesis, Northern Illinois University, August 2008.
9. Pradeep Babburi, " **Durability and Degradation Mechanism of Ten Unit 100W Polymer Electrolyte Membrane Fuel Cell For Vehicle Application**", December 2008.
10. Rajesh Boddu, " **Analysis of Fluid Flow Transport Phenomena in Gas Channels of Bipolar Plate for Fuel Cell**", M.S Thesis, Northern Illinois University, December 2005.
11. Uday Kum ar Marupakula, " **Simulation and Design of Bi-polar Plates Integrated PEM Fuel Cell for Automotive Systems**", M.S Thesis, Northe rn Il linois University, Summ er, 2007.
12. Gaurav Deshpande, " **Fuel Cell Bipolar Plate-Material Selection, Design and Analysis**", M.S Thesis, Northern Illinois University, Summer 2007.
13. Pavan Kum ar Konne pati, " **Three-Dimensional Simulation of Polymer Electrolyte Membrane Fuel cells with Bipolar Plates**", M.S Thesis, Northern Illin ois Universi ty, Fall, 2007.
14. Sunil Kom akula, "**Steady and Dynamic Simulation of Polymer Electrolyte Membrane Fuel Cells for Automotive Applications**", M.S Thesis, No rthern I llinois Unive rsity, May 2008.
15. Benjamin Summers, "**Fabrication, Testing and Performance Evaluation of Bipolar Plates with Integrated Heating and Cooling**", M.S Thesis, Northern Illinois University, Fall 2008.
16. Manasa Majjiga, MS, " **Study of Thermal, Structural, and Resistivity Properties of the Sr(Mn,Fe,Co)O_{3-} System**", September 2006.

17. Benjamin Keith Stillwell, MS, "**Evaluation Of Potential Cathode Materials For Reduced-Temperature Solid Oxide Fuel Cells**", May 2007.